Onshore and offshore seismotectonics of Iberia: An updated review

Antonio Olaiz[1], José A. Álvarez Gómez[2], Gerardo de Vicente[2,3], Alfonso Muñoz-Martín[2,3], Juan V. Cantavella[4], Susana Custódio[5], Dina Vales[6] and Oliver Heidbach[7,8].

[1]Repsol E&P, C/Méndez Álvaro 44, 28045, Madrid, Spain
[2]GEODESPAL, Faculta de C.C. Geológicas, Universidad Complutense de Madrid, Spain
[3]Instituto de Geociencias IGEO, CSIC-UCM, Madrid, Spain
[4]Instituto Geográfico Nacional, C/General Ibáñez Íbero, 3, 28003, Madrid, Spain
[5]Instituto Dom Luiz, Faculdade de Ciências, Universidade de Lisboa, 1749-016 Lisboa, Portugal.

[6]Instituto Português do Mar e da Atmosfera, Lisboa, Portugal
[7]Helmholtz Centre Potsdam, GFZ German Research Centre for Geosciences. Germany, 14473 Potsdam, Germany
[8]Institute for Applied Geosciences, TU Berlin, 10587 Berlin, Germany

Correspondence to: Antonio Olaiz (antoniojose.olaiz@repsol.com)

Abstract. From the analysis of 542 moment tensor focal mechanisms in Iberia, active tectonic deformations and stresses were inferred by implementing different and complementary methodologies: FMC classification of the rupture type; composed focal mechanism based on the average seismic moment tensor; rotation angle between tensors estimates; Right Dihedra composed focal mechanisms; Slip Model analysis to determine the strain conditions and classical stress inversion methodology. By using the Slip Model results and considering the tectonic constraints of the Cenozoic deformation in Iberia, the study region was subdivided into a series of zones where the different methods were individually applied. The results indicate that thrust faulting stress regimes are active in the Gorringe-Horseshoe area and the easternmost Tell Atlas. In the south, most of the zones are transpressive, as well as in the southwestern corner of Iberia, south of Lisbon. The exception is the Granada Basin, which displays an almost radial normal faulting stress regime. Normal faulting stresses are dominant in the Pyrenees and in the Mediterranean rim, north of the Betics. In the central part of the Pyrenees, we find a maximum horizontal extension perpendicular to the range, indicating that local stresses related to post-orogenic collapse or isostatic rebound dominate over regional ones. The maximum horizontal compression along the Eurasia-Africa plate limit is very homogeneously close to N154°E, except in some parts of the Betics that are probably influenced by a remanent effect of the Alboran Slab. In the Central Ranges and offshore Atlantic, the maximum horizontal compression is slightly rotated anticlockwise to N140°E.

1 Introduction and objectives

The Iberian Peninsula, and the former Iberian microplate, shows evidence of an intense and distributed Alpine deformation that occurred over geologic time scales (de Vicente and Vegas, 2009) (Fig. 1). After the Variscan orogeny, and during the Mesozoic, numerous extensional structures developed, in which thick sedimentary deposits accumulated, with one exception, on the Iberian Massif to the west. At the northern edge of the Iberian microplate, this extension even reached the stage of oceanic crust generation (Montadert et al., 1971; Nirrengarten et al., 2018; Sibuet et al., 2004), albeit during a very short time (Aptian-Albian) (Srivastava et al., 1990). According to tectonic reconstructions, the Iberian microplate moved independently relative to Africa and Eurasia until it collided with Eurasia to form the Cantabrian-Pyrenean Orogen. A pronounced change in the tectonic framework has been suggested to have occurred around 84 Ma, when an incipient collision between the Iberian microplate and Africa may have begun (Reicherter and Pletsch, 2000). In any case, from the beginning of the Eocene, the Iberian microplate underwent significant compression, not only at its northern border, where an incipient subduction zone was located (Gallastegui and Pulgar, 2002; Fernandez-Viejo et al., 2012), but also in its interior.

The result of Alpine compression in the interior of the Iberian microplate was the inversion of the Mesozoic aulacogen of the Iberian Basin (Iberian Chain, IC), and the development of a series of ranges with crustal thickening along the Iberian Microplate (i.e. the Spanish-Portuguese Central System, SPCS). This set of intra-plate ranges can also be considered as an incipient and aborted orogen (de Vicente et al., 2022). It has also been suggested that the Iberian block accommodated shortening by forming lithospheric folds (Cloetingh et al., 2002). Accompanying these large thrusts, major strike-slip faults and deformation belts were activated at the crustal scale, such as the South ("Castilian") and North ("Aragonese") Branches of the IC, and the Messejana-Plasencia fault (more than 500 km long), which nucleated on an end-Triassic basic dyke related to the Central Atlantic Magmatic Province (Cebriá et al., 2003; Villamor, 2002; de Vicente et al., 2021). The age of the main deformation event for these fault systems is Oligocene - Lower Miocene, although, in the westernmost sector, the SPCS and the left-lateral strike-slip faults of Règua and Vilariça display significant deformation during the Middle-Upper Miocene, and are still considered as active structures (Cabral, 2012).

Today, extensional structures dominate the easternmost part of the Iberian Peninsula (since the Upper Miocene), due to back-arc extension related to a subduction zone below Corsica and Sardinia, which were initially a part of the Iberian microplate (van Hinsbergen et al., 2014). A normal faulting stress regime, unrelated to plate tectonics, also affects the Pyrenees, where a post-orogenic collapse process has been suggested (Asensio et al., 2012). Thus, the active plate boundary would have migrated from the north, when Iberia was an independent microplate, to the south of the Iberian Peninsula (Terceira Ridge - Gloria Fault – Alboran - Tell Atlas), when Iberia became a part of the Eurasian Plate, where the emplacement of the Alboran Domain and the subduction of the southern edge of the Iberian Peninsula, have produced a diffuse plate boundary that encompasses the Betics, where shortenings and extensions occur almost simultaneously. In this Cenozoic and neotectonic complex deformation setting, it is not surprising that the present tectonic stresses in Iberia display large variations in both the stress regime and orientation of the principal stress axes (de Vicente et al., 2008) over relatively small areas.

The estimation of earthquake focal mechanisms in recent years, performed by Geophysical Institutes in Spain and Portugal (IGN, IAG and IPMA), has generated a large amount of information that adds to scientific publications resulting from different projects, such as TopoIberia (e.g. Matos et al., 2018; Martín et al., 2015), or significant earthquake crisis (e.g. Cesca et al., 2021; Villaseñor et al., 2020).

In this study, we will exclusively use well-fitted moment tensor focal mechanisms to study the contemporary deformation pattern in the Iberian Peninsula. We analyse the rupture characteristics of focal mechanisms populations for defined tectonic subareas and use the Slip Model described by Reches (1983) and de Vicente (1988) to assess which of the two nodal planes was the rupture plane. This information and the focal mechanism populations are then used to perform a stress inversion to determine the orientation the maximum horizontal stress (S_{Hmax}) and the tectonic stress regime. We also derive from the individual focal mechanism the S_{Hmax} orientation and integrate these results and the ones from the stress inversion into a revised dataset from the World Stress Map project based on borehole logs, overcoring measurements and geological stress indicators.

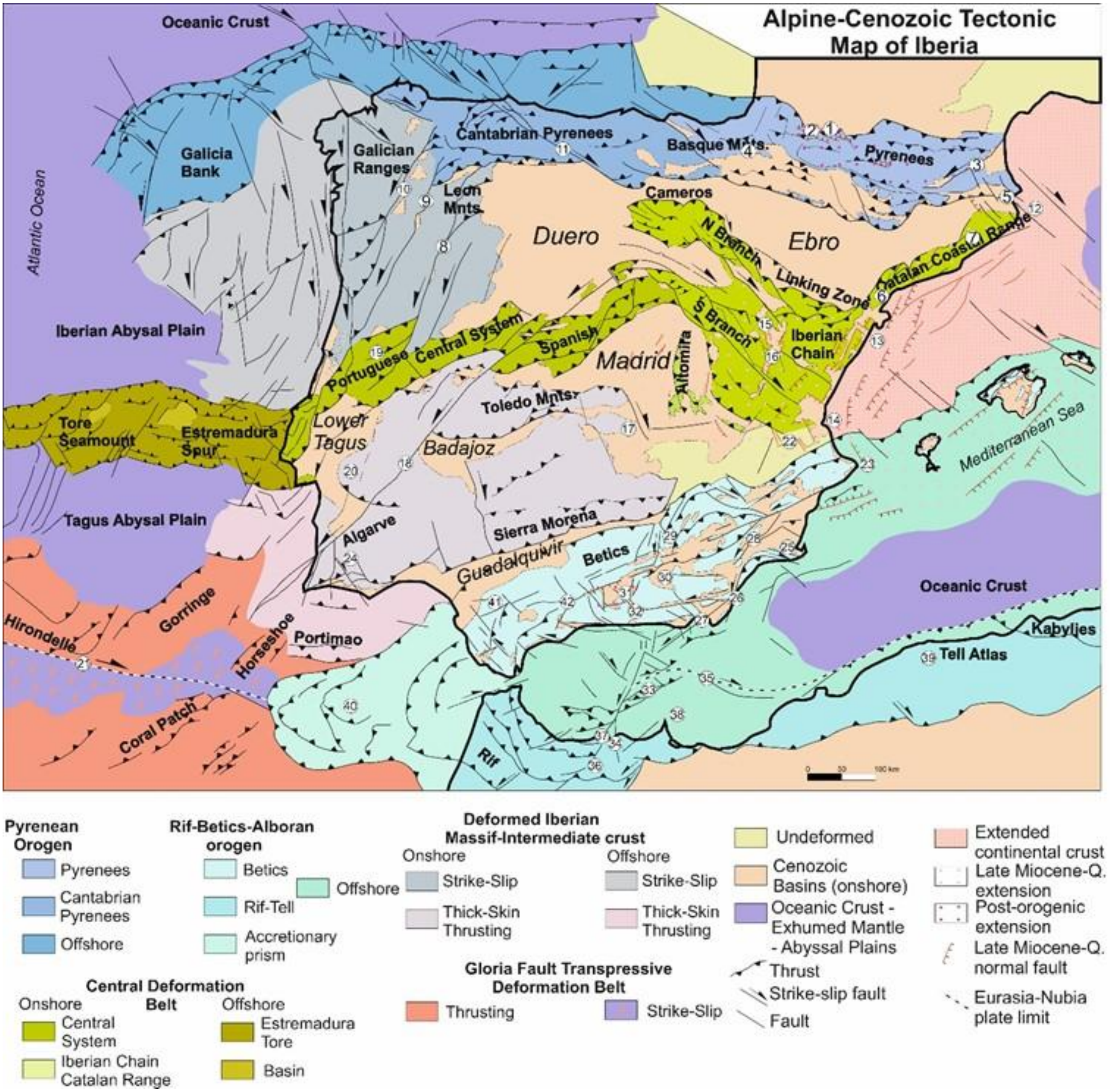

Figure 1: Alpine-Cenozoic tectonic map of Iberia, including continental and offshore domains, and showing areas that have experienced intense and distributed deformation. More recent normal faulting is shown by red lines. Q: Quaternary. Lourdes Fault (1), Bedous, Laruns, Pierrefitte and Pic de Midi du Bigorre faults (2), Têt Fault (3), Pamplona Fault (4), Amer and Empordà faults (5), El Camp Fault (6), Montseny and Pla de Barcelona faults (7), Vilariça-Bragança fault system (8), Régua-Verín fault system (9), Monforte-Orense fault system (10), Ventaniella-Ubierna faults (11), Gulf of Rosas Fault (12), Amposta Basin Fault (13), Cape Cullera Fault (14), Jiloca Graben (15), Teruel Graben (16), Campos de Calatrava volcanism (17),

Messejana-Plasencia Fault (18), Serra da Estrela Fault (19), Arraiolos and Évora seismic zones (20), Gloria Fault (21), Navarrés and Tous grabens (22), Cabo de la Nao Fault (23), São Marcos - Quarteira Fault (24), Mazarrón Fault (25), Palomares Fault (26), Serrata-Carboneras Fault (27), Alhama Fault (28), Tiscar and Guadiana Menor faults (29), Guadix Basin (30), Granada and Sierra Elvira-Dílar faults (31), Padul-Dúrcal Fault (32), Alborán Ridge (33), Idrissi Fault (34), Yusuf Fault (35), Nekor Fault (36), Al Hoceima area (37), Kert and Nador faults (38), Fault propagation associated to El Asnam earthquake (39), W verging thrusts Gulf of Cádiz (40), NE-SW thrusts (41), Torcal Shear Zone (42)

2 Data from earthquake focal mechanism

In this study we establish a new and comprehensive compilation of robust focal mechanism solutions of Greater Iberia, inferred from waveform moment tensor inversions, using the following catalogues:

- Global Centroid Moment Tensor (former Harvard Centroid Moment Tensor https://www.globalcmt.org/, Dziewonski et al., 1981; Ekström et al., 2012)
- Instituto Geográfico Nacional de España (https://www.ign.es/web/ign/portal/tensor-momento-sismico/-/tensor-momento-sismico/getExplotacion, Rueda and Mezcua, 2005)
- Instituto Andaluz de Geofísica (https://iagpds.ugr.es/investigacion/informacion-general, Stich et al., 2003, 2006, 2010).
- Istituto Nazionale di Geofisica e Vulcanologia (http://terremoti.ingv.it/en/tdmt; Scognamiglio et al., 2006; Pondrelli et al., 2002, 2004)
- Geofon (GFZ-Postdam) (https://geofon.gfz-potsdam.de/old/eqinfo/list.php?mode=mt)
- ETH- Swiss Seismological Service (https://geophysics.ethz.ch/research/groups/sed.html) (Braunmiller et al., 2002).
- IPMA Portuguese Institute for Sea and Atmosphere (https://www.ipma.pt/en/geofisica/tensor)

This dataset was then expanded with different regional publications (e.g. Carreño et al., 2008; Chevrot et al., 2011; Domingues et al., 2013; Custodio et al., 2016), datasets associated with projects such as TopoIberia (Martín et al., 2015), datasets related to earthquake clusters (Morales et al., 2015; Matos et al., 2018) and specific publications concerning seismic crises (e.g. Cesca et al., 2021; Villaseñor et al., 2020). In addition, nine unpublished moment tensor focal mechanisms were determined for events occurred between 2003 and 2019 (Table 1) and focal mechanisms for two historical events were also included in our dataset (Stich et al., 2005). The events are shallower than the Moho proposed by Diaz et al. (2016), with exception of some events located in oceanic crust (depth < 30 km), where the rheology of the upper mantle might assume as similar to the crust.

In those cases where an event is duplicated, having solutions in more than one catalogue, the double couple percentages (%DC) were compared and the solution with the highest %DC was selected.

Long (º)	Lat (º)	Depth (km)	StrikeA (º)	DipA (º)	RakeA (º)	StrikeB (º)	DipB (º)	RakeB (º)	Mw	Date (YYYY/MM/DD)
-5.98	41.5	9	7	71	25	268	66	160	3.8	20030112
-2.34	40.21	11	228	71	-157	130	69	-20	3.3	20091014
-7.62	38.96	15	288	75	180	18	90	15	3.5	20100327
-8.546	37.35	8.5	84	85	168	175	78	6	3.3	20150722
-2.29	41.61	12	179	46	-87	355	44	-93	3.6	20150805
-8.524	37.237	20	216	50	88	39	40	92	3.2	20151021
-4.62	42.86	14	134	75	-86	297	16	-106	3.6	20180519
-9.552	37.73	28	35	62	52	275	62	52	3.6	20181001
-8.013	36.37	30	175	42	-165	74	80	-49	3.8	20190716

Table 1: New focal mechanisms calculated in this study

Thus, the final database consists of 542 events. In terms of temporal coverage, the first earthquake in our database is that of Benavente (Portugal) in 1909 and the most recent one occurred on 30 September 2023 (Fig. 2).

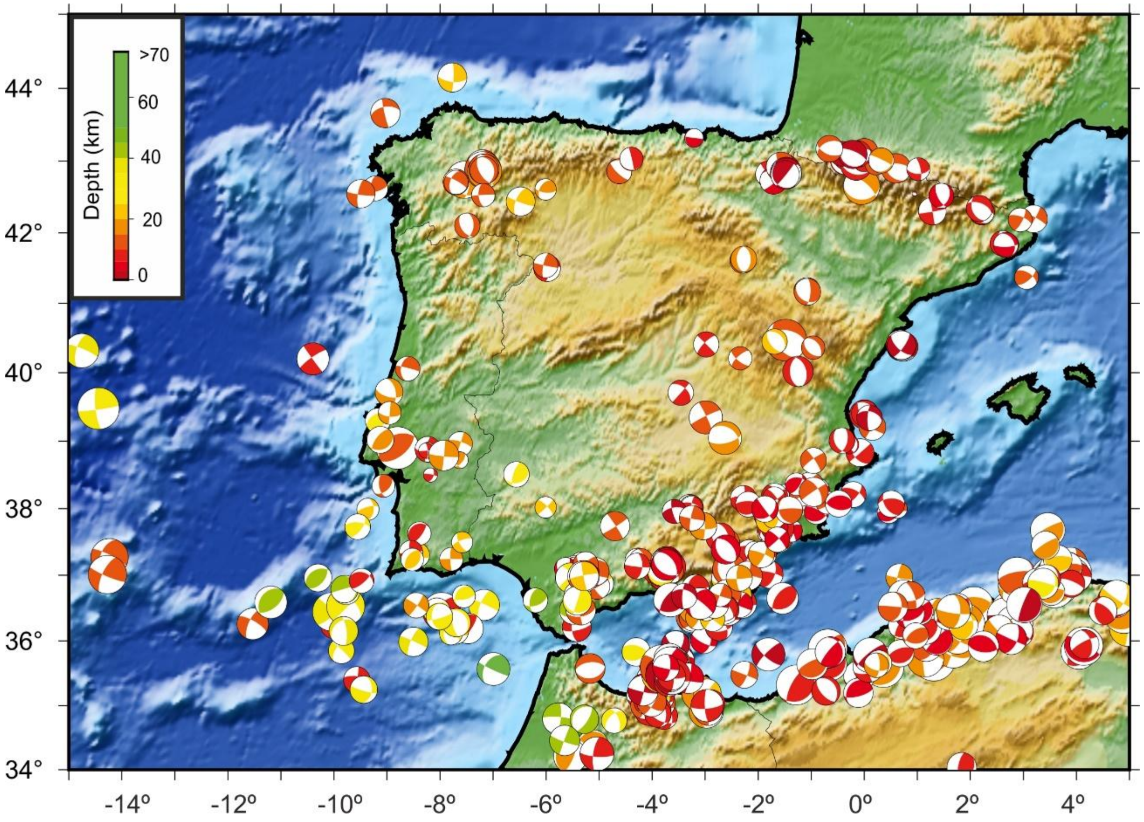

Figure 2: Distribution of the 542 focal mechanisms used in this study. The color of focal mechanisms indicates hypocentral depth.

3 Methodology

To describe the tensor characteristics of seismicity, either a stress-type or a deformation-type approach can be adopted. Both types of analysis are complementary, therefore we will use both. In the case of the deformation type analysis, we will use two approaches: A kinematic analysis that will classify the type of rupture and obtain a combine focal mechanism (Álvarez-Gómez, 2019; Kiratzi and Papazachos, 1995), using also, the right dihedral diagram (Angelier and Mechler, 1977) and the slip model (Reches, 1983). To determine the stress tensor using classical inversion procedures, we will use the methodology proposed by Reches et al., (1992). This approach enables iterative testing of various friction coefficients, validated by angular criteria established by SLIP and PAM, as detailed in the subsequent section. The methodology has been recently revised and implemented in MATLAB (Busetti et al., 2014; Wetzler et al., 2021).

Thus, we will use the appropriate terminology for each type of analysis. In the case of individual focal mechanisms, we will differentiate between reverse, strike-slip, and normal ruptures. When we refer to deformation, we use terms as shortening, shear, and extension. Conversely, when we deal with stresses, we use thrusting stress regime, strike-slip stress regime and normal faulting stress regime.

3.1 Kinematic analysis. Composite focal mechanism

To gain insight into the kinematics related to the brittle behaviour of the lithosphere, we binned the focal mechanisms according to their rupture characteristics and stress-strain orientations in tectonic sub-areas. We refer to these from here onwards to as tectonic zones. These zones were delimited considering the tectonic regimes, using a methodology that is explained in more detail in section 4 as is a fundamental step on the stress inversion analysis.

For each tectonic zone, we classified the focal mechanisms by rupture type (reverse, strike-slip, normal) using the Focal Mechanisms Classification (FMC) diagram (Álvarez-Gómez, 2019). Then, for each rupture type population, we obtained a combined focal mechanism by averaging the moment tensor components following the approximation of Kiratzi and Papazachos (1995):

$$\bar{F}_{ik} = \frac{\sum_{x=1}^{n} M_o^x F_{ik}^x}{\sum_{x=1}^{n} M_o^x} , \qquad (1)$$

where Fik is the normalized moment tensor, M0 is the seismic moment, and the sums are performed over the number of events in each rupture population. If most of the released seismic moment is controlled by one of the earthquakes, the composed focal mechanism is very close to that larger event (Kiratzi and Papazachos, 1995). To avoid this effect in areas with moderate seismicity, an adequate approximation is to use only the sum of the seismic moment tensor components, disregarding the respective seismic moments. In this case, all earthquakes will have the same weight in the sum.

$$\bar{F}_{ik}^{RT} = \sum_{x=1}^{n} \bar{F}_{ik}^{x} , \qquad (2)$$

where RT is each of the rupture types, encompassing n events, and i and k are the indices of the moment tensor components.

As a result, we obtain a combined focal mechanism for each rupture type reflecting the geometry of the corresponding moment tensors and related deformation.

Following this reasoning we can obtain also a composed focal mechanism considering all the events in a tectonic zone:

$$\bar{F}_{ik}^{zone} = \sum_{y=1}^{n} \bar{F}_{ik}^{(y)} = \bar{F}_{ik}^{Reverse} + \bar{F}_{ik}^{Strike-slip} + \bar{F}_{ik}^{Normal}, \qquad (3)$$

As can be seen in equation 3, the summation of the combined rupture types is equivalent to the sum of all tensors. This step allows us to estimate the degree of strain partitioning by means of the computation of the minimum rotation angle (Kagan, 1991) between the different rupture types as is described below.

A way to assess the character of a moment tensor is to use its compensated linear vector dipole (clvd) component, which quantifies the extent to which the deviatoric part of the seismic moment tensor differs from a pure double-couple. We used the clvd ratio (fclvd) from Frohlich and Apperson (1992):

$$fclvd = \frac{|m_B|}{max[|m_T|,|m_P|]}, \qquad (4)$$

where mT, mB and mP are the largest, intermediate, and smallest principal components of the summed moment tensor. When the double couple component is dominant, the fclvd tends to be 0 while when the value approaches 0.5 the tensor is far from a double couple. The clvd proportion of the summed moment tensor can be used also to analyse the seismotectonics of a zone (e.g. Frohlich and Apperson; 1992; Jost et al., 1998; Buforn et al., 2004; Borges et al., 2007; Bailey et al., 2012).

If we consider the composed moment tensor to be a representation of the seismic strain in a zone, we can use its orientation and characteristics to get insight into the deformation pattern of the studied tectonic zones. A first approximation is to consider the orientation of the principal strain axes. The T axis is equivalent to the extension axis, the P axis is equivalent to the shortening axis, and the B axis is the intermediate axis, which can be neutral for a plane strain deformation (a pure double couple moment tensor) or it can be an extension or a shortening axis depending on the tectonics of the zone.

It is of interest also to quantify the amount of seismic deformation taking place in each zone using the different rupture types. These different rupture processes on a zone cannot be considered to reflect temporal changes in the regional deformation field as the time interval of the catalogue is very short, but rather local strain axes permutations. To quantify these changes in the orientation of the axes between rupture types, we resort to the minimum rotation angle between tensors (or Kagan angle; Kagan, 1991). The angle for a pure axis permutation maintaining the orientation of all the axes would be 90°. In practice, if we consider the angle between the focal mechanisms of different types of rupture and given that they nucleate in faults with different orientations, this angle may depart slightly from 90º.

Finally, to analyse the shape of the seismic deformation tensor, we can adapt the Flinn diagram for 3D strain tensor shapes used in classic structural geology analysis. The Flinn diagram represents the relation between the principal strain axes, or principal extension (Flinn, 1958), where the abscissa is the relation ŝ2/ŝ3 and the ordinate the relation ŝ1/ŝ2. An alternative to these values was proposed by Ramsay (1967) who suggest the use of natural logarithm of these relations so that:

$$ln[\hat{s}_1/\hat{s}_2] = \varepsilon_1 - \varepsilon_2 , \tag{5}$$

$$ln[\hat{s}_2/\hat{s}_3] = \varepsilon_2 - \varepsilon_3, \tag{6}$$

where ε1, ε2 and ε3 are the natural strains of the largest, intermediate, and smallest principal strain axes of the deformation ellipsoid; i.e. the magnitude of the changes in the length of the axes. Similarly, the principal strain axes of the combined seismic moment tensors can be considered the amount of seismic strain change induced by the earthquakes in a volume. Consequently the logarithmic Flinn diagram can be adapted to this purpose. Additionally, the shape of the ellipsoid can also be defined by the k-value, which is defined as

$$k = \frac{\varepsilon_1 - \varepsilon_2}{\varepsilon_2 - \varepsilon_3} , \tag{7}$$

This parameter has values of 0 for oblate strain shape, 1 for plane strain and ∞ for prolate strain shapes. In the case of seismic moment tensors, a pure double couple has the form

$$\begin{bmatrix} M_0 & 0 & 0 \\ 0 & 0 & 0 \\ 0 & 0 & -M_0 \end{bmatrix}, \tag{8}$$

having the values of the principal axes the same magnitude although of opposite sign to conserve the volume. Strictly speaking, a double couple corresponds to a plane strain ellipsoid with no strain on the orthogonal plane to the maximum and minimum moment axes mT=-mP, mB=0. If the intermediate moment axis is different from 0, then the compensated linear vector dipole component appears as shown in equation 3.

To represent the combine seismic moment tensors in the Flinn diagram we defined the ordinate and abscissa as M1 – M2 (or mT – mB) and M2 – M3 (or mB – mP) respectively, where M1 ≥ M2 ≥ M3 (we used the logarithm of these values to improve the data presentation). The shape of the tensor can then be defined in an equivalent way as in equations (5 and 6):

$$k = \frac{M_1 - M_2}{M_2 - M_3} , \tag{9}$$

3.2 Kinematic analysis. Slip model

Focal mechanisms provide valuable insights into earthquake rupture kinematics, including the strike, dip and rake of the two nodal planes. However, most of the time, the selection of the true fault plane among the two possible ones is not straightforward. The strain orientation derived from thrust or normal faulting focal mechanisms may remain the same irrespective of the true fault plane, but the dip direction of the fault would not be constrained. On the other hand, for strike-slip faulting focal mechanisms, the strike of the fault plane is crucial to properly define the strain field.

The Slip Model (Reches, 1983; de Vicente et al., 1988) identifies which of the nodal planes is more prone to slip from a mechanical point of view (the neoformed plane). Additionally, it is helpful to identify areas under similar strain conditions. In this study, we apply the workflow suggested by de Vicente et al. (2008), Olaiz et al., (2009) and Arcila and Muñoz-Martín (2020). The Slip Model proposed by Capote et al. (1991), based on de Vicente (1988) and Reches (1983), defines the maximum shortening trend (Dey, E_{Hmax}) and the shape factor (k´) of the deformation ellipsoid for each individual focal mechanism. This method, based on the Navier–Coulomb fracture criterion, assumes that the brittle strain and stress axes are parallel and that one of the axes is close to vertical. According to the Slip Model, under the triaxial strain conditions of brittle strain, fractures are arranged in orthorhombic symmetry concerning the fundamental axes of the strain ellipsoid.

$$k' = e_y/e_z, \tag{10}$$

where ez is the axis of the vertical strain and ey is the axis of the maximum horizontal shortening
Accordingly, replacing ey and ez in equation (10):

$$k' = (sin^2Dcos^2B)/(1 - sin^2Dcos^2B)\ , \tag{11}$$

$$B = sin^2Dcos^2P\ , \tag{12}$$

Where D is the dip and P the pitch of the slip vector on the fault plane.
Two sequences of strain are established as a function of k´, from reverse to normal trough strike-slip faulting, and k´ is rescaled to plot values continuously (Table 2).

k´ = ∞	Plane strain	Pure strike-slip (Pitch =0)
∞ > k´> 1	Shear with extension	Strike-slip normal
k´= 1		
1 > k´> 0	Extension with shear	Normal strike-slip
k´= 0	Plane strain	
0 > k´> -0.5	Radial extension	Pure normal (Pitch = 90)
k´= -0.5	Pure radial extension	
k´= -0.5	Pure radial shortening	
-1 > k´> -0.5	Radial shortening	Pure reverse (Pitch = 90)
k´= -1	Plane strain	
-2 < k´< -1	Shortening with shear	Reverse strike-slip
k´= -2		
-∞ < k´< -2	Shear with shortening	Strike-slip reverse
k´ = -∞	Plane strain	Pure strike-slip (Pitch = 0)

Table 2 k´ values obtained from the Slip Model

Additionally, based on the relationship between dip and pitch proposed by de Vicente (1988), when the nodal plane coincides with the character of the focal plane, frictional energy is dissipated more efficiently. Therefore, the selected plane can be utilized in stress inversion methods based on striation-fault pair orientations (Angelier and Mechler, 1977). Hence, the quality of the stress inversion results is improved compared to those obtained using both planes (Michael, 1987; de Vicente, 1988; Giner-Robles et al., 2006).

3.3 Dynamic analysis, stress inversions

For the stress inversion we apply the method proposed by Reches et al. (1992). The method incorporates two constraints: first, the stresses in the slip direction satisfy the Coulomb yield criterion; and second, the slip occurs in the direction of maximum shear stress along the fault. The computations yield the complete stress tensor, normalized by the vertical stress, and evaluate the mean coefficient of friction (μ) and the mean cohesion (C) of the faults during the time of faulting (Reches, 1987). Thus, for every selected population, two angular quality criteria are obtained: the slip misfit (SLIP), which is the mean angle between the observed and calculated slip axes of all faults in the cluster, and the principal angles misfit (PAM), which is the angle between the ideal stress axes of each nodal plane and general stress axes of the entire group according to the optimal mechanical condition for faulting (Reches, et al., 1992). In addition, the stress ratio (R) is stablished as is proposed by McKenzie (1969), Etchecopar et al. (1981), Gephart and Forsyth (1984), Delvaux et al. (1997) among others (Equation 13, Table 3).

$$\mathrm{R} = (\sigma_2 - \sigma_3)/(\sigma_1 - \sigma_3)\ , \qquad (13)$$

To assess the statistical representativeness of the population of focal mechanisms within in each tectonic zone, a Monte Carlo bootstrapping approach was employed to determine the value of the friction coefficient with the least errors. This technique enables us to determine the potential variability of the principal stress axes, particularly the possible permutations between two principal stress axes when they have similar magnitudes.

R		Stress Regime	Vertical axis
R=1	$\sigma_1 = \sigma_2 > \sigma_3$	Radial Thrusting	σ_3
1 > R > 0	$\sigma_1 > \sigma_2 > \sigma_3$	Triaxial Thrusting	σ_3
R = 0	$\sigma_1 > \sigma_2 = \sigma_3$	Uniaxial Thrusting	σ_3
0.5 > R > 0	$\sigma_1 > \sigma_2 > \sigma_3$	Strike-slip Thrusting	σ_2
R = 0.5	$\sigma_1 = \sigma_2 > \sigma_3$	Pure Strike-slip	σ_2
1 > R > 0.5	$\sigma_1 > \sigma_2 > \sigma_3$	Strike-slip Normal	σ_2
R =1	$\sigma_1 = \sigma_2 > \sigma_3$	Uniaxial Normal	σ_1
1 > R > 0	$\sigma_1 > \sigma_2 > \sigma_3$	Triaxial Normal	σ_1
R =0	$\sigma_1 > \sigma_2 > \sigma_3$	Radial Normal	σ_1

Table 3: Relation between stress tensor (R shape factor ratio) and the stress regime.

4 Tectonic zonation for stress-strain analysis

To define the tectonic zones needed for the stress inversion and the strain analysis we use the Slip Model (De Vicente et al., 1988). This model provides unique values of the shape factor (k´) and the orientation of the shortening (or minimum extension) axis (Dey) for each individual focal mechanism. Interpolation of these values enables the generationof continuous maps that show the variation of both parameters (e.g. de Vicente et al., 2008; Olaiz et al., 2009; Arcila and Muñoz-Martín, 2021). In this study, we built interpolated maps of the shape factor (k´) and the value for Dey using the blockmean module of the Generic Mapping Tools (Wessel and Smith, 1991; Wessel et al., 2013). The shape factor (k´) is a scalar that varies between 0 and 300. Therefore, the values are average normalized for each node and subsequently interpolated on a continuous surface. These maps are a powerful tool to better defining different strain regions based on homogenous shape factor values and similar Dey trends. Thus, the grouping of the focal mechanisms is straightforward, allowing for the optimization of results for techniques designed for populations.

The three fundamental pieces of information that we considered for the delineation of the tectonic zones in the Iberian Peninsula are (a) the available information on the neotectonic (in this case, Alpine) structural deformational style (Fig. 1), (b) the density of the available data (Fig. 2), and (c) the dominant type of focal mechanism. The global and interpolated analysis of the data using the Slip Model allows us to consider these parameters simultaneously (Figs. 3 and 4).

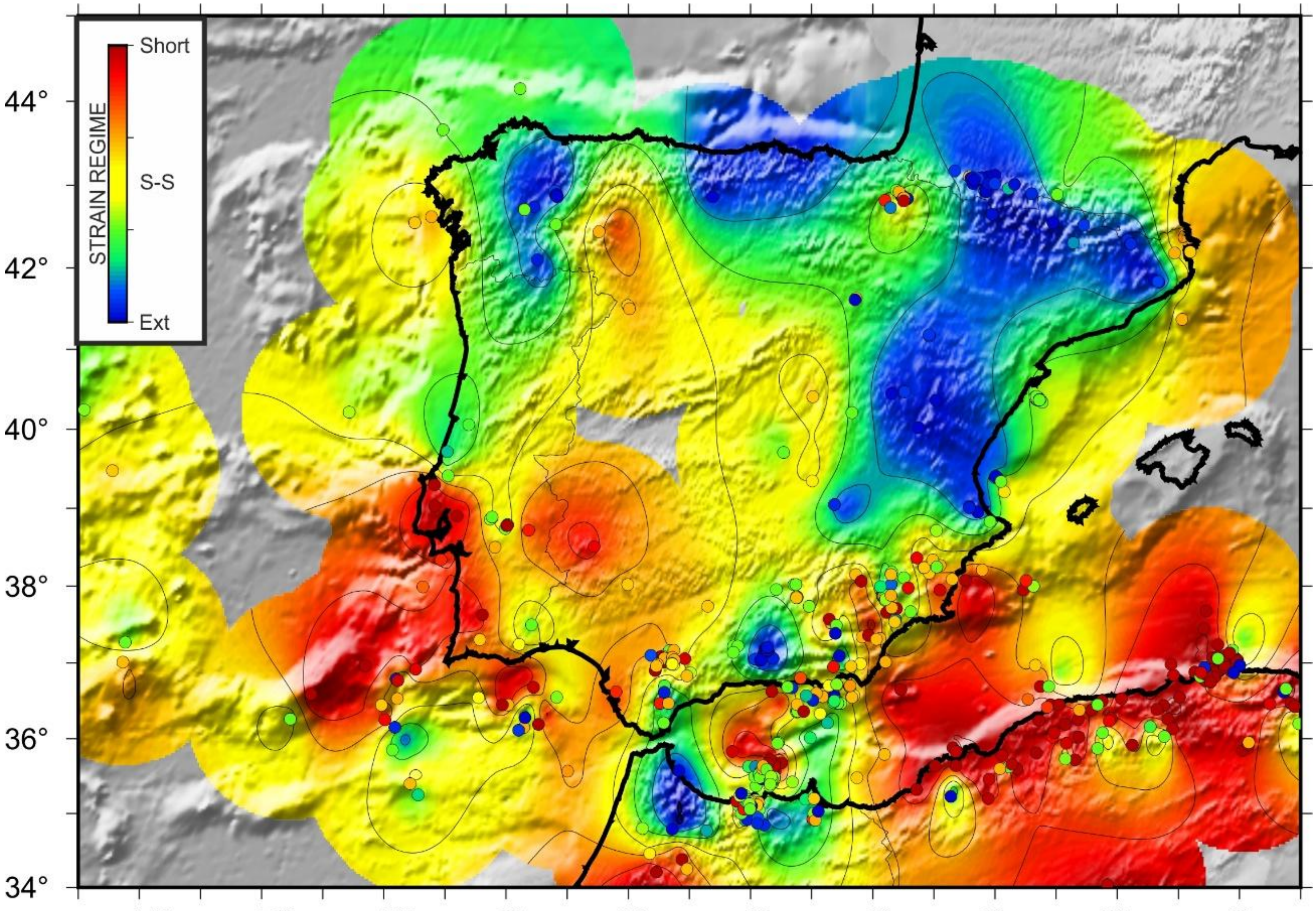

Figure 3: Style of active deformation (strain regime) for Iberia determined from focal mechanisms. The map shows the shape factor (k´) determined using the Slip Model (Reches, 1983 and de Vicente, 1988). Each dot represents a focal mechanism. Search radius of 150 km. Short.: shortening. S-S: shear strain. Ext.: extension.

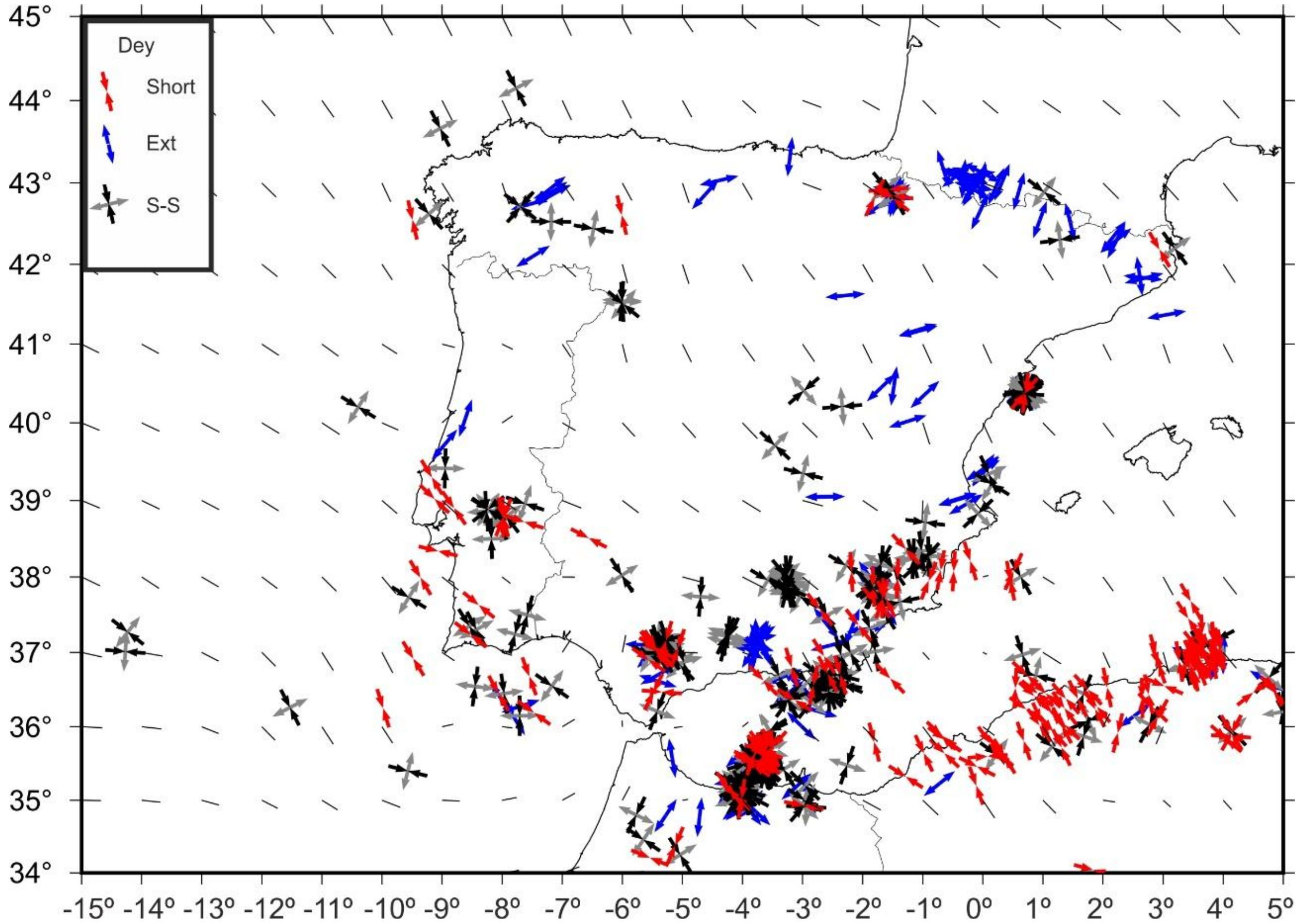

Figure 4: Solutions of the Slip Model (by assuming that one principal strain axis is vertical) for all analysed focal mechanisms. Short, and Ext denote the principal horizontal shortening and extension axes, respectively, and S-S the shear strains. Black bars are Dey trend interpolations.

Considering these criteria, we sub-divided Iberia into the following zones (Fig. 5):

In the Pyrenees, we identified three zones: the Central Pyrenees (CP), characterized by mostly normal faulting focal mechanisms, and two additional zones at the eastern and western ends, where there are more focal mechanisms: the Western Pyrenees (WP) and the Eastern Pyrenees - Northern Catalan Coastal Range (EPCE). Further west, on the north edge, we grouped together the earthquakes in North-Western Galicia (NWG), with numerous focal mechanisms in the central area, as well as offshore. In the east of the peninsula, offshore near the coast, we have differentiated two tectonic zones: the North Valencia Trough (NVT) and the South Valencia Trough (SVT). The former is from a local seismic network. Onshore, we have separated the focal mechanisms in the IC and south of the eastern SPCS (Central Basins, CB), as well as those in the tectonic zone near Lisbon, which we refer to as the Western Central System (WCS). Further south but not yet at the active plate boundary, we defined the Algarve (AL) as the tectonic zone. In the offshore Atlantic to the west, although the data are very scattered, the focal mechanisms are similar, and several correspond to earthquakes that occurred at mantle depths but are not well-constrained. Therefore, we grouped them in the tectonic zone Offshore Atlantic (OA). Further south, primarily offshore and along the plate boundary, we examined the Gorringe-Horseshoe (GH) and Gulf of Cádiz (GC) tectonic zones. The large number and variability of focal mechanisms in the Betics require smaller tectonic zones. Thus, considering the predominance of normal faulting in the Granada Basin (GB), we differentiated the Western Betics (WB) to its west, the Betics Antequera (BA) to its north, and the Eastern Betics (EB) to its east. In the Alboran Sea, we considered the North Alboran (NA), which also has onshore focal mechanisms, and the Alboran Ridge (AR), located at the probable plate boundary. Further south, on the African plate, in the Rif, we considered the tectonic zones of Al Hoceima (ALH) and Rif (RF). Finally, in the Algerian Atlas, we analysed two populations: one located further east, the Eastern Tell Atlas (ETA), and the other located further to the west, the Western Tell Atlas (WTA). Fig. 5 shows the focal mechanisms in different colours for each area. We used the Rif (RF) focal mechanisms in the Slip Model analysis (Figs. 3 and 4), but any stress inversion had a good quality solution and, therefore, we are not going to comment on RF active tectonics (Fig. 5). Cádiz

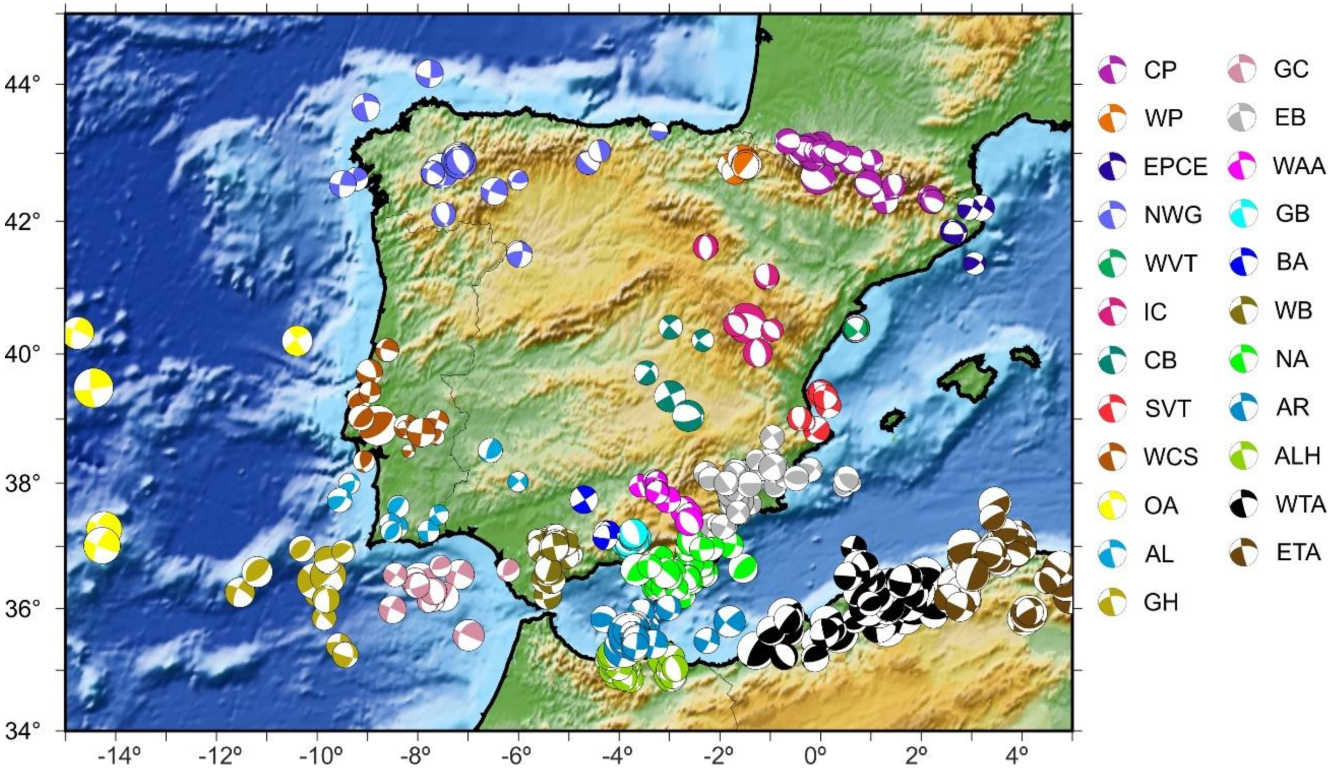

Figure 5: Color-coded focal mechanisms for every considered tectonic zone: Central Pyrenees (CP); Western Pyrenees (WP); Eastern Pyrenees-Northern Catalan Coastal Range (EPCE); North-Western Galicia (NWG); Western Valencia Trough (WVT); Iberian Chain (IC), Central Basins (CB); Western Spanish Portuguese Central System (WCS); Offshore Atlantic (OA); Gorringe-Horseshoe (GH); Southern Valencia Trough (SVT); Algarve (AL); Eastern Betics (EB); Western Alcaraz Arch (WAA); Granada Basin (GB); Northern Alboran (NA); Alboran Ridge (AR); Al Hoceima (ALH); Western Tell Atlas (WTA); Eastern Tell Atlas (ETA); Gulf of Cádiz (GC); Western Betics (WB); Betics Antequera (BA).

5 Results

The results obtained following the methodologies described above are summarized in Tables 4 and 5 for all considered tectonic zones. For additional information see Appendix A and Appendix B.

Label	Population	Combined Seismic Moment Tensor main axes						Rupture type	fclvd	k value	Minimum Rotation Angle (º)		
		P trend	P plunge	B trend	B plunge	T trend	T plunge				N-SS	SS-R	R-N
CP	Central Pyrenees	163	76	**296**	10	28	10	N	-0,10	1,39	88,6	-	-
WP	Western Pyrenees	**99**	21	287	69	190	3	SS	-0,31	3,52	82,1	74	72,7
EPCE	Eastern Pyrenees	**344**	17	129	70	251	11	SS	-0,28	2,98	76,1	-	-
NWG	NW Galicia	**328**	14	138	76	237	2	SS	-0,34	4,09	78,5	43,8	98,4
WVT	Western Valencia Trough	**2**	29	143	54	262	19	SS-N	0,06	0,84	16,3	25,6	25,5
IC	Iberian Chain	309	86	**154**	4	64	2	N	0,04	0,89	-	-	-
CB	Central Basins	**276**	6	31	77	185	12	SS	-0,26	2,58	70,3	-	-
WCS	Western SPCS	**323**	3	229	60	55	30	SS-R	0,29	0,33	44,9	71,7	99,4
OA	Offshore Atlantic	**152**	22	297	64	57	14	SS-N	0,03	0,92	-	-	-
GH	Gorringe-Horseshoe	**164**	15	44	62	260	23	SS-R	0,33	0,26	49,6	68,7	90,2
SVT	Southern Valencia Trough	18	73	**157**	13	249	11	N	-0,25	2,56	74,1	-	-
AL	Algarve	**143**	6	31	75	234	14	SS	0,41	0,13	80,3	-	-
EB	Eastern Betics	**352**	15	119	67	258	18	SS-R	0,22	0,46	46,7	83,6	71,4
WAA	W Alcaraz Arch	**143**	3	333	87	233	0	SS	-0,23	2,30	87	-	-
GB	Granada Basin	250	76	**139**	5	48	13	N	0,08	0,77	-	-	-
NA	Northern Alboran	**334**	6	217	76	66	12	SS	-0,15	1,63	88,3	49,7	100
AR	Albora Ridge	**337**	20	173	70	69	5	SS	0,19	0,52	64,8	76,4	98,4
AH	Al Hoceima	**329**	24	157	65	60	3	SS-N	-0,08	1,30	50,8	58,2	76,6
WTA	Western Tell Atlas	**324**	15	231	10	108	71	R	0,29	0,33	67,4	80,4	105,5
ETA	Eastern Tell Atlas	**336**	26	69	8	175	63	R	0,08	0,77	77,8	73,5	96,3
GC	Gulf of Cádiz	**161**	15	291	67	66	17	SS-R	0,24	0,42	91,9	66,6	94,4
WB	Western Betics	**332**	11	235	31	79	57	R-SS	0,20	0,50	35,9	58,6	59,9
	Western Betics > 20 km	**299**	18	81	67	205	13	SS-N	0,22	0,44	80,4	90,1	105,8
BA	Betics Antequera	**305**	30	101	58	209	11	SS-N	-0,05	1,16	-	-	-

Table 4: Summary of the combined seismic moment tensor results for all considered zones. Bold numbers are the trend the greatest horizontal shortening axis trend and underlined numbers are the trend of the most horizontal extensional axis.

Label	Tectonic zones	Dey	SHmax	σ1 tr	σ1 pl	σ2 tr	σ2 pl	σ3 tr	σ3 pl	R	Fric	Cohe	N/Nad	PAM	SLIP
CP	Central Pyrenees	119±12	121,5	196	83	121	1	3	4	0,35	0,6	0,0187	28/28	23,11	17,7
WP	Western Pyrenees	101±24	98,6	90	59	103	31	190	6	0,7	0,1	0,0351	12/14	33,63	30,15
EPCE	Eastern Pyrenees	166±20	165,1	349	48	158	41	253	6	0,42	0,3	0,0312	6/6	36,1	21,1
NWG	NW Galicia	155±14	147,8	290	79	150	9	59	5	0,6	0,4	0,0354	17/21	17,96	27,53
WVT	Western Valencia	0±14	170,8	359	35	125	39	245	31	0,34	0,2	0,0096	11/12	15,92	9,99
IC	Iberian Chain	166±9	141,8	54	87	148	0	238	3	0,43	0,1	0,0114	8/8	24,37	16,44
CB	Central Basins	78±12	84,3	270	55	80	34	173	4	0,61	0,4	0,0055	6/6	23,33	6,19
WCS	Western SPCS	140±19	137,2	134	13	209	50	54	37	0,38	0,1	0,0451	20/20	33,65	29,29
OA	Offshore Atlantic	140±28	133,9	151	15	166	72	44	10	0,92	0,1	0,0059	5/5	18,75	2,97
GH	Gorringe-Horseshoe	133±26	157,3	159	24	251	5	352	65	0,41	0,1	0,0204	8/13	38,82	11,3
SVT	Southern Valencia	166±21	147,8	129	80	149	9	238	3	0,5	0,1	0,0029	8/10	20,72	6,69
AL	Algarve	117±20	146,3	140	17	334	72	232	4	0,14	0,6	0,0658	11/11	38,22	14,681
EB	Eastern Betics	163±18	169,1	171	13	112	66	256	20	0,35	0,01	0,0033	47/47	31,13	29
WAA	W Alcaraz Arch	160±13	152,5	153	8	325	82	62	1	0,8	0,6	0,0614	14/14	22,43	16,13
GB	Granada Basin	136±13	119	263	84	123	6	33	5	0,11	0,5	0,0152	16/16	18,92	14,72
NA	Northern Alboran	163±20	151,2	149	14	187	72	62	10	0,73	0,01	0,0024	42/42	28,12	24,24
AR	Alboran Ridge	166±17	161,8	161	22	159	68	251	1	0,34	0,01	0,0023	62/62	26,79	19,8
AH	Al Hoceima	147±17	153,6	152	36	159	54	64	4	0,69	0,1	0,0186	41/41	21,63	19,77
WTA	West Atlas	146±15	145,3	145	12	199	71	58	15	0,14	0,2	0,0366	44/44	25,99	16,83
ETA	East Atlas	166±17	145,6	149	20	164	13	185	65	0,4	0,01	0,0032	52/52	25,52	23,09
GC	Gulf of Cádiz	148±12	147,7	150	5	251	64	58	25	0,19	0,1	0,0144	10/12	23,09	16,14
WB	Western Betics	148±22	140,7	139	16	212	45	63	40	0,18	0,1	0,031	28/28	28,68	24,54
	Western Betics > 20 km	148±14	78,7	114	17	113	72	204	0	0,26	0,01	0,0041	6/7	24,27	23,28
BA	Betics Antequera	102±11	104,8	105	3	109	87	15	0	0,91	0,7	0,0061	5/5	13,04	7,97

Table 5: Summary of the stress inversion results for all considered zones. Dey defines the maximum shortening trend. R defines the stress ratio. Tr is the trend of the axis and pl is the plunge of the axis. N denotes number of events, and Nad is number of events for the given solution (adjusted). PAM is the principal angles misfit and SLIP is the slip misfit.

5.1 CP Central Pyrenees

The focal mechanisms in this area are mostly normal, although some strike-slip faults are also observed. The seismic moment release is controlled by the normal fault events giving rise to a combined moment tensor close to double couple, with a k value of 1.39 and an fclvd of 0.1. The Kagan angle between the combined moment tensors of normal and strike-slip earthquakes has a value close to 90°, indicating an almost pure permutation between the B and P axes. The orientations of the principal strain axes (T and B) are consistent with each other and orthogonal to the strike of the mountain range, although these axes show some variability with two predominant families, one N020°E-N030°E and the other N040°E-N050°E, which could indicate the activation of normal fault families with slightly different orientations (see Appendix A).

The 28 focal mechanisms located in the central part of the Pyrenees provide a very consistent stress inversion solution (Fig. 7 CP) that indicates a nearly uniaxial normal faulting stress regime, with a direction of N005°E-N030°E , sub-perpendicular to the topographic axis of the range. The solution, as obtained by de Vicente et al. (2009) and Asensio et al. (2012). The latter authors also analysed GPS data with similar results (extension perpendicular to the range of 2.5±0.5 nanostrain yr-1), which they attributed to post-orogenic collapse. This normal faulting stress regime would account for the seismic activity of the main active normal faults present in the area, such as the Lourdes Fault (1), which has a 50 km trace and a 50 m fault scarp (Alasset and Meghraoui, 2005; Lacan and Ortuño, 2012), as well as those of Bedous, Laruns, Pierrefitte and Pic de Midi du Bigorre (Lacan 2008) (2) . The latter authors attribute the seismicity in this part of the Pyrenees to a process of isostatic rebound. In this area, we also include the focal mechanisms in the easternmost part of the area, obtained close to the Têt Fault (3), which is 120 km long and accommodated right-lateral movement from the Miocene to the Upper Pliocene (Cabrera et al., 1988), and which during the Plio-Quaternary seems to have had mainly extensional movement (Briais et al., 1990). In any case, the three nearby focal mechanisms show normal faulting, consistent with the other mechanisms used for the inversion. Recent studies, calculated with polarities and temporary seismic networks, provide very similar focal mechanisms (Ruiz et al., 2023).

5.2 WP Western Pyrenees

Seismicity in the western Pyrenees is clustered in the south of the mountain range, in the vicinity of the city of Pamplona. This seismic activity is characterised on the one hand by normal faulting, with a strike-slip component, and on the other by a series of oblique events with an important strike-slip component. This component is important in the area, with the combined moment tensor having mainly shearing characteristics, although with fclvd values of 0.31 and a k of 3.52, which indicates a prolate-type seismic deformation tensor shape. The strain axis of the combined mechanism is N011E and that of maximum horizontal shortening (B and P permuting) between N090°E-N110°E.

The stress inversion (Fig. 7 WP) results also in a normal faulting stress regime as in CP (N098E), although the stress tensor shows characteristics closer to strike-slip, with σ2 at N103°E, which allows activating WNW-ESE to E-W normal faults, such as those of Leiza, Aralar and Roncesvalles (Lacan and Ortuño, 2012), but also NE-SW strike-slip faults, such as the Pamplona Fault (4), which is 125 km long (Ruiz et al., 2006). This is a vertical fault, inherited from the Late Variscan, which also controlled Mesozoic and Tertiary sedimentation (Ruiz et al., 2006) and was reactivated as an oblique ramp during the Pyrenean shortening (Vergés, 2003).

5.3 EPCE Eastern Pyrenees-Northern Catalan Coastal Range

This tectonic zone, which contains only 6 focal mechanisms was differentiated from the Central Pyrenees population because here, as in the westernmost part, there seem to be more strike-slip faulting mechanisms (the easternmost ones). Half of the population, with epicentres close to the axis of the mountain range, present pure normal faulting mechanisms while the other half has a thrust faulting component. The Kagan angle between the combined normal and strike-slip faulting mechanisms is close to 80°, suggesting a permutation between the P and B axes. The combined moment tensor departs from a pure double couple, with an fclvd of 0.28 and a k-value of 2.98. The shape of the ellipsoid is therefore of prolate type, with the strain axis oriented at N72E and the maximum shortening almost horizontal at N163°E.

The stress inversion (Fig. 6 EPCE) indicates a more normal faulting stress regime (N165E) concerning CP, similar to that obtained by Goula et al. (1999) with normal strike-slip stresses, whichdiffers from the one provided by these authors, which was more thrusting. The onshore focal mechanisms would indicate that the structures associated with the recent NW-SE Olot volcanism, the Amer and Empordà faults (5) (Souriau and Pauchet, 1998; Lacan and Ortuño, 2012) present normal-type movements, which would have been responsible for the seismic crisis between 1427 and 1428 that caused considerable damage (Olivera et al., 2006). Active faults further south, in the Catalan Coastal Range, such as the El Camp (6) (Masana, 1996) Montseny and Pla de Barcelona (7) (Perea et al., 2020) seem to be more related to the opening of the Valencia Trough than to the Pyrenees. In any case, the stress solution is very similar to those found to the south in IC, WVT and SVT, so it seems to be less related to the local processes affecting the Pyrenees.

5.4 NWG North-Western Galicia

The Pyrenean orogen spans across northern Iberia to the Cantabrian Cordillera (Cantabrian Pyrenees), Galicia and offshore, as far as the Galicia Bank (Fig. 1). The southern part of the Bay of Biscay, the closest to Iberia, also appears to be affected by the deformation of the Pyrenees (e.g. Boillot and Malod, 1988) where the shortening took place from the Upper Eocene to the Middle Miocene (Gallastegui and Pulgar, 2002). After the Middle Miocene, much of the neotectonic activity in Galicia and Northern Portugal was concentrated in the left-lateral strike-slip NNE-SSW fault system of Vilariça-Bragança (8), Règua-

Verín (9) and Monforte-Orense (10) (Cabral, 1989; de Vicente & Vegas, 2009; Martín González et al., 2012), which, although not strictly a part of the Pyrenees, are closely related to its evolution, as well as to that of the SPCS.

The focal mechanisms in this zone can be grouped into two families, one of normal faulting type releasing most of the seismic moment, and the other of oblique strike-slip faults, some with normal components and other with reverse faulting components (see Appendix). By using the Kiratzi & Papazachos (1995) approximation, which gives equal weight to all combined events in the tensor, we avoid the dominance of events with a much higher energy release than the others. The resulting combined moment tensor shows a prolate form, with k values close to 7 and an fclvd of 0.39, dominated by ENE-WSE extension. The strain axes are very coherent in all focal mechanisms, with the combined one having an orientation of N057°E. In the horizontal shortening axes (P and B permuting with a rotation angle of 84°) there is more variability, with the P axis showing an orientation of N147°E.

The 18 focal mechanisms included in the stress inversion (Fig. 6 NWG) are of strike-slip and normal-directional types, resulting in a common normal faulting stress regime, with a strike of N147°E and a dip of N150°EIt should be noted that the most normal faulting mechanisms are concentrated in the area where small sedimentary basins developed during the Miocene, specifically in the interior of Galicia (de Vicente et al., 2011). In contrast the offshore region is dominated by strike-slip faulting.

We were only able to obtain one focal mechanism in the Cantabrian Mountains (Cantabrian Pyrenees), which shows NW-SE normal faulting. This focal mechanism could indicate that important faults in that orientation, such as the Ventaniella-Ubierna faults (11), accommodate normal faulting deformation today. A study using a local seismic network (10 stations) on the Ventaniella Fault determined focal mechanisms for earthquakes of Mw<2 without obtaining a consistent pattern (López-Fernández et al., 2018), therefore the results in this area are not conclusive. The two focal mechanisms with the highest double-couple component (above 80%) calculated by del Pie Perales (2016) are normal faulting solutions and the focal planes are compatible with the strike-slip fault system. Recently, on September 30th, 2023, a Mw=3.6 thrusting focal mechanism was reported by the IGN in Villamejil (León).

5.5 NVT Western Valencia Trough

The Valencia trough, between the Mediterranean rim of Iberia and the Balearic Islands, shows a complex succession of partially inverted Mesozoic rifting events during the Cenozoic (Etheve et al., 2018). During the last 30 Myr, the emplacement of the Calabrian-Tyrrhenian subduction zone with trench retraction and back-arc extension produced intense extension in the Levantine sector of Iberia (Faccenna et al., 2004) during the Neogene (Roca and Guimerà, 1992), forming a broad rifting zone with the development of many horsts and grabens. This extension is moderately active today (Perea et al., 2020).

The Castor CO_2 storage project generated a sequence of apparently triggered seismicity. In addition to the moment tensors calculated by the IGN, several groups published focal mechanisms (Cesca et al., 2021; Villaseñor et al., 2020). The moment tensors present mostly similar solutions in both studies, in terms of plane orientations, although the depth and epicentral location vary significantly. Due to the better epicentral relationship with the previously identified NE-SW striking faults, the results used here were those by Villaseñor et al. (2020). These mechanisms show strike-slip fault offset with a strong normal component, very similar to those obtained by Goula et al. (1999) for the 1991 and 1995 events based on P-wave polarities. The combined moment tensor shows an N082°E trending T axis and an immersion of 19°. The P axes show somewhat more scatter, still, the P axis of the combined moment tensor is oriented N002°E, with an immersion of 28°. The value of k obtained is 0.8, which indicates an oblate-type tensor shape, with N-S shortening and E-W extension.

The stress inversion of the 12 focal mechanisms (Fig. 6 WVT) yields a very consistent solution, indicating a normal faulting stress regime compatible with strike-slip and oriented N170°E. This stress regime activates moderately dipping NE-SW and NW-SE faults, such as those of the Gulf of Rosas (12), the Amposta Basin (13), Cape Cullera (14) and the Columbretes Basin (Perea et al., 2020), which affect Plio-Quaternary sedimentary units (Perea et al., 2012). Onshore, the El Camp Fault (6) (Masana, 1996) can also be activated by this type of stresses. The stress solution for this zone is very similar to that of the SVT.

5.6 IC Iberian Chain

The IC is part of the Iberian intraplate orogen, with a main Oligocene-Lower Miocene age of deformation, which involved the inversion of Permo-Mesozoic rifts (Álvaro et al., 1979). From the Upper Miocene onwards, its activity is linked to the opening of the Valencia trough (Roca and Guimerà, 1992) and therefore shows a similar evolution to the WVT. To the W, the extension deactivated the thrusts that uplifted the SPCS north of Madrid. The recent extensional process formed Neogene-Quaternary basins associated with N-S to NW-SSE normal fault activity (Simón, 1989). The associated stress field, from recent fault data, shows triaxial normal faulting, with σ3 oriented ENE-WSW (Arlegui et al., 2005). The most important active faults are those bounding the Jiloca graben (15) (Sierra Palomera, Calamocha, Daroca, Munébrega faults) and the Teruel graben (16) (Sierra del Pobo, Valdecebro and Concud) (Simón, 2020).

The 8 focal mechanisms in this tectonic zone are normal faulting events, with a few showing a strike-slip component, which combined give rise to a pure double-couple tensor with a horizontal T-axis oriented N064°E and B-axis oriented N154°E. The individual moment tensors are divided into two distinct families (see Appendix), with T- and B-axis rotations of about 30º, probably due to the activation of complementary normal fault families.

The focal mechanisms used for the stress inversion, located in the north and centre of the IC, yield a triaxial normal faulting stress regime solution (Fig. 6 IC), with σ3 oriented N058°E, similar to that of the WVT and compatible with the results obtained from recent faults analyses (Arlegui et al., 2005). Thus, the active stress field can activate the aforementioned normal faults (Simón, 2020).

5.7 CB Central Basins

In central Iberia, south of the SPCS and W of the IC, in the Cenozoic basins of Madrid and La Mancha (CB), we find 6 focal mechanisms, mainly showing strike-slip and normal faulting. Most of the strike-slip solutions correspond to small seismic moment releases. The combined moment tensor shows an fclvd of 0.25 and a value of k of 2.58, corresponding to a prolate-type tensor shape dominated by a strain axis oriented N005°E and an axis of maximum shortening nearly oriented E-W. The stress inversion of the focal mechanisms (Fig. 6 CB) indicates a normal faulting stress regime solution with a small strike-slip component, with σ3 almost perpendicular to that obtained for the CI, at N173°E, which also differs from most of the areas considered. However, geodetic velocities obtained from GPS data in this area show a clear westward displacement (considering Eurasia fixed) with rates of 2 - 3 mm/yr. (Cannavò and Palano 2016; Neres et al., 2018a), different from the NW-SE movement seen further to the south. The results published by Khazaradze et al. (2018) further support a dominant strike-slip faulting regime. On the other hand, and as a differential element, the area is characterised by volcanism, mainly sodic alkaline and ultra-alkaline rocks, with radiometric ages between 4 Ma to less than 0.7 Ma (Ancochea and Huertas, 2021) (Campos de Calatrava volcanism) (17) , which has been related to a gentle folding of the Iberian lithosphere and the presence of an anomalous low-density sub-crustal block below the volcanic zone (Granja Bruña et al., 2015). It is therefore possible that this recent volcanic activity somehow influences the calculated stress tensor. An edge effect related to large-radius extension and uplift in the CI cannot be ruled out (Casas-Sáinz and de Vicente, 2009), nor is an indentation effect related to the Betics.

5.8 WCSWestern (Spanish Portuguese) Central System

As mentioned before, the central orogenic belt extends to the west, reaching as far as Lisbon and offshore into the Estremadura Spur. In its Portuguese stretch, the SPCS is an active mountain range (Cabral, 2012), with reported damage to structures that were translated into earthquake intensities such as the Benavente earthquake in 1909 with an estimated moment magnitude Mw= 6.0 and a significant thrust faulting component (Stich et al., 2005; Fonseca & Vilanova, 2010). The thrust faults have predominantly NE-SW strikes with associated NW-SE shortening (de Vicente et al., 2018). To the east of Portugal, in the westernmost Spanish sector, and along the NE part of the Messejana-Plasencia fault (18), instrumental seismicity is scarce. However, there is evidence of end-Cenozoic and Quaternary deformation (de Vicente et al., 2022).

The focal mechanisms in this tectonic zone are predominantly reverse or strike-slip faulting events, the former showing a higher release of seismic energy. There are some normal faulting events whose T and B axes are kinematically compatible with each other. Considering the combined mechanisms of strike-slip and reverse faulting, we calculated the value of the minimum rotation angle close to 70°, thus constituting a T and B permutation. The orientation of the axis of maximum shortening of the combined moment tensor is N146°E and the axis of maximum extension is oriented N056°E. The overall combined moment tensor, considering all earthquakes in this zone, is of oblate type, with a low k value of 0.325 and an fclvd of 0.29; thus being dominated by NW-SE shortening.

The stress inversion for this tectonic zone (Fig. 6 WCS) was computed using 20 focal mechanisms and resulted in a clear thrust faulting stress regime solution with a small strike-slip component, with σ1 oriented N134°E. This stress regime activates NE-SW striking thrust faults and left lateral NNE striking and right-lateral ESE striking strike-slip faults. Examples include the Vilariça-Bragança (8) and Régua-Verín (9) faults, which exhibit left-lateral movement. Additionally, there are faults from S Galicia (NWG, with σ2 at N150E) to the Serra da Estrela (19) with a thick-skinned tectonic style without tectonic inversion, and the SPCS (Cabral, 2012) with σ1 at N134°E. The thrusts bordering the Lusitania Basin to the S and the Lower Tagus Cenozoic Basin to the north are also active with kinematics that are directly related to the inferred stress tensor. Focal mechanisms to the east show mainly strike-slip faulting in the Arraiolos and Évora seismic zones (20), within the Ossa-Morena zone of the Variscan basement, consistent with right-lateral motion on N065°E faults (Matos et al., 2018).

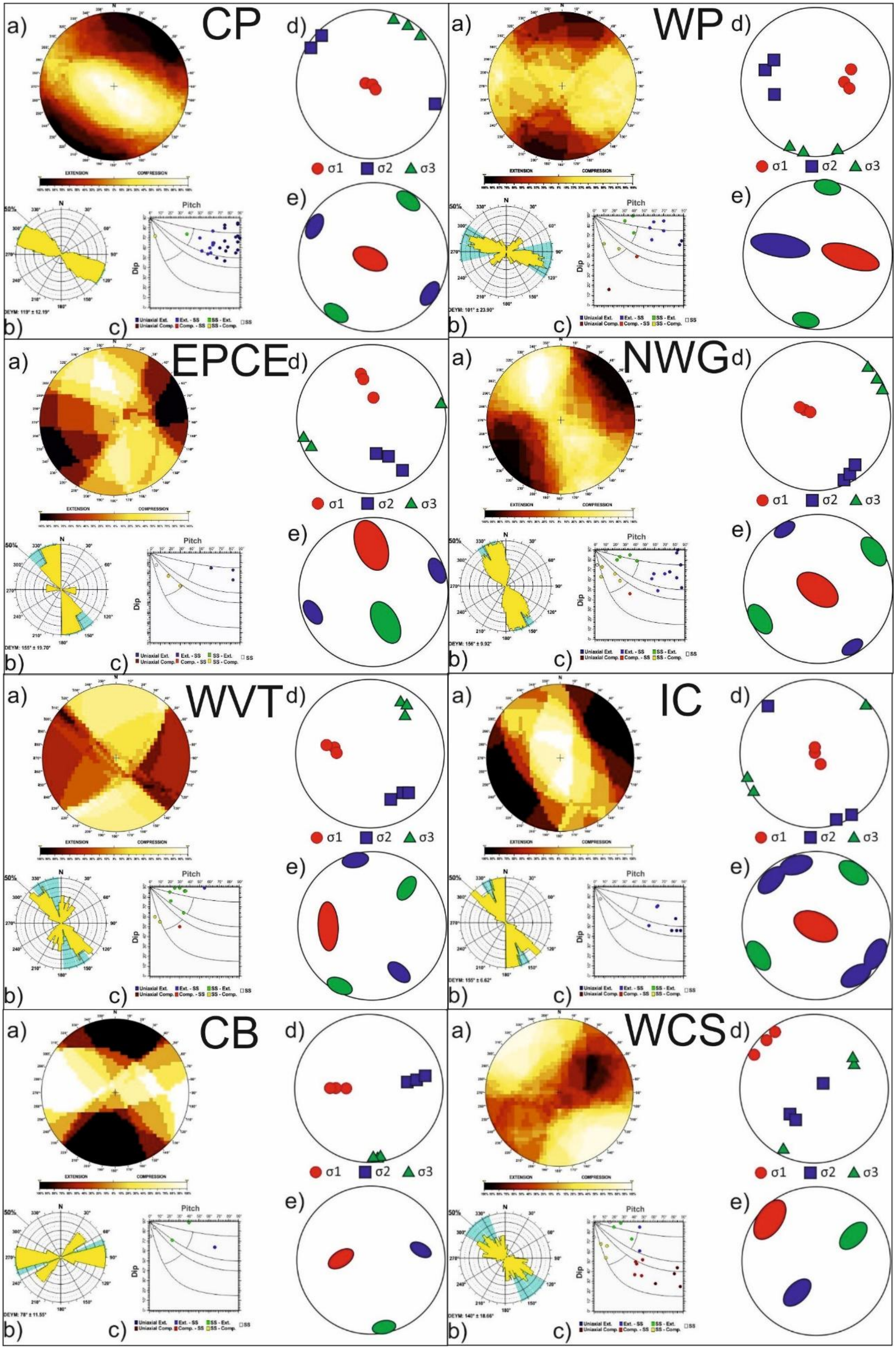
CP
WP
EPCE
NWG
WVT
IC
CB
WCS
a)
b)
c)
d)
e)
σ1
σ2
σ3
EXTENSION
COMPRESSION
Pitch
Dip
N
50%
DEYM: 119° ± 12.19°
DEYM: 101° ± 23.90°
DEYM: 155° ± 19.70°
DEYM: 156° ± 9.92°
DEYM: 155° ± 6.62°
DEYM: 78° ± 11.55°
DEYM: 140° ± 18.66°
Uniaxial Ext.
Ext. - SS
SS - Ext.
SS
Uniaxial Comp.
Comp. - SS
SS - Comp.

Figure 6 Results of the stress-strain analyses for different zones: a) Right Dihedra solution. b) Rose diagram of the Deys obtained from the Slip model. C) Pitch/Dip plot for the neo-formed nodal planes obtained from the Slip Model. d) Stress Inversion Results. e) Variability of the three principal stress axes of the stress inversion. CP Central Pyrenees; WP Western Pyrenees; EPCE Eastern Pyrenees-Northern Catalan Coastal Range; NWG North-Western Galicia; WVT Western Valencia Trough; IC Iberian Chain, CB Central Basins; WCS Western Spanish Portuguese Central System.

5.9 OA Offshore Atlantic (ES Estremadura Spur)

The focal mechanisms in the Atlantic offshore, to the north of the active plate boundary, are spatially scattered over a wide area and some appear to be deeper than the Moho (although the depth of these earthquakes is poorly constrained by the mainland seismic networks). We grouped all these events given their similar characteristics. Between the Tagus and the Iberian abyssal plains, there is a structural high, the Estremadura Spur, with E-W to NE-SW thrusts, which is the offshore extension of the SPCS, affecting the intermediate crust (Terrinha et al., 2009). Between this tectonic uplift and the Galicia Bank to the north, NNE-SSW faults seem to dominate, with kinematics similar to those onshore (Vilariça-Bragança (8) and Régua-Verín (9) fault systems). In the south, there are some focal mechanisms close to the Hirondelle structural high, to the north of the Gloria fault (21). In the Estremadura Spur, a NNW-SSW shortening regime dominated the main structuring of the range during the Palaeocene-Miocene (Pereira et al., 2021): However,the most recent and active deformation appears to be transpressional (Neves et al., 2009).

There are 6 strike-slip focal mechanisms in this zone, some of which have a small normal component. These moment tensors show some variability in their principal axes, especially in the P axis. Therefore, the combined moment tensor presents k values below 1, an fclvd greater than 0 (Fig. 7 OA), and a tendency to have an oblate shape, with the P axis having a dominant N152°E orientation. The extension T-axis is in the N057°E direction. The stress inversion indicates a strike-slip stress regime with a normal component, characterized by σ1 at N131°E and σ3 at N044°E, which activates right-lateral ESE-WNW faults, such as the significant like the major strike-slip Gloria fault (21) in the North Atlantic, which defines the present-day plate boundary between Eurasia and Africa.

5.10 GH Gorringe-Horseshoe

At the active plate boundary, and between the NE-SW structural highs (pop-ups and restraining steps with thick-skinned tectonic styles) of Gorringe and Horseshoe, there are 13 reverse and strike-slip focal mechanisms, several of which below the Moho, that indicate a thrust-faulting stress regime (Fig. 7 GH) with σ1 at N159°E. These focal mechanisms are mainly strike-slip with a vertical component and reverse faults with some horizontal component. There are also normal-type mechanisms whose T axes are kinematically compatible with the T axes of the other events. The orientations of the axes of maximum horizontal shortening and extension exhibit considerable variability, with the T axes giving rise to two well-differentiated families: one N040°E-060°E and the other N070°E-N090°E (see Appendix). The more E-W trending axes seem to be more associated with the strike-slip faults in the centre and south of the region, while the reverse fault events in the northern part have NE-SW B-axis orientations. The combined moment tensor presents an oblate shape, dominated by shortening, with a k value of 0.623 and an fclvd of 0.14, indicating a significant distribution of deformation across different structures. The orientation of the P and T axes are N155E and N65E, respectively.

Deformation along the Gloria fault (21) (zone OA) is purely strike-slip and locally transtensional, whereas between the Gorringe and Horseshoe tectonic uplifts (zone GH) it is compressional (Zitellini et al., 2009). The most prominent structure, the Gorringe Bank, is bounded by NE-SW crustal thrusts, the most significant one located on its northern edge. This structure was the source of destructive landslides during the Miocene, with renewed Plio-Quaternary activity (Gamboa et al., 2021). Several earthquakes have hypocentres at upper mantle depths (>20 km), implying that the observed surface thrusts must be linked to structure at mantle levels (Grevemeyer et al., 2017). Active deformation has reactivated and inverted former Mesozoic normal faults (García-Navarro et al., 2005) and appears partitioned between NW-SE thrusts and WNW-ESE to W-E strike-slip faults (Terrinha et al., 2009). Further south, the Coral Patch Ridge shows a similar tectonic structuring (Martínez-Loriente et al., 2013). The inferred stress tensor activates pure NE-SW thrusts and right-lateral NW-SW reverse-strike-slip and WNW-ESE strike-slip faults, which may be the tear faults of the thrusts (Ferranti et al., 2014).

5.11 SVT Southern Valencia Trough

In the easternmost onshore part of the Prebetic front, on the undeformed foreland, Betic compression ceased approximately 10 Myr ago. This area is structured in a series of horsts and grabens, about 25 km long and 5 km wide (Navarrés, Tous) (22), which triggered a diapirism of the Triassic salt (Keuper facies) when the extension associated with the opening of the Valencia Trough was imposed in the area (De Ruig, 1995). The main trend of the grabens is perpendicular to the Betic front (NW-SE), although there are also parallel grabens, indicating triaxial extension. Their position explains why they are not plug-type diapirs, but rather linear ones, which were controlled by multiple faulting episodes (Jackson and Hudec, 2017). The diapirism is still active, affecting Quaternary materials (Gutierrez et al., 2019). The coastline also changes in this sector to NW-SE, while further north, up to the Pyrenees, it has a NE-SW orientation, which is that of the main faults in the Valencia Trough, as in WVT. This orientation, which is transverse to the main trough, must likely influenced by the Betic front. The offshore Cabo de la Nao fault (23) would be one of the main faults of this transverse fault system (Maillard and Mauffret, 1999).

We have 10 focal mechanisms in this tectonic zone. Most of them indicate normal faulting, but there are also strike-slip focal mechanisms. The combined tensors present minimum rotation angles of 74°, showing a permutation between the B and P axes. The combined tensor has an fclvd value of -0.25 and a clearly prolate tensor shape with k = 2.56, showing the predominance of the N069°E oriented extension. The stress tensor obtained from the inversion (Fig. 7 SVT) indicates a normal faulting stress regime, with σ3 at N058°E, which is capable of activating the transverse fault system of the southernmost part of the Valencia Trough, located in the foreland of the Betic orogen. The stress tensor solution is very similar to those of IC, WVT and EPCE.

5.12 AL Algarve

The southwestern corner of the Iberian Massif, in the Portuguese Algarve, also comprises a band of Mesozoic and Cenozoic materials, known as the Algarve Basin, which was inverted during the Cenozoic due N-S to NW-SE shortening. The NW-SE shortening developed later, from the Miocene to the present (Terrinha, 1998; Ramos et al., 2015) and activated E-W to NE-SW striking thrust faults. Still in this zone but north of the basin there are important strike-slip faults, such as the southernmost part of the Messejana-Plasencia Fault (18) (NE-SW, left lateral) and the São Marcos - Quarteira Fault (24) (NW-SE, right lateral). According to GPS data, the southern block of this fault exhibits significant movement to the nortwest relative to the northern block (Cabral et al., 2017). It displays clear activity during the Quaternary (Cabral et al., 2019). Offshore, the most relevant tectonic structure is the Portimão Bank, bounded by E-W thrusts and co-located with a Cretaceous magmatic intrusion (Terrinha et al., 2009; Vázquez et al., 2015; Neres et al, 2018b). Throughout the Algarve basin, there is active salt tectonics (Matías et al., 2011).

We can group the focal mechanisms in this zone into pure and reverse strike-slip faulting. Although there is some scatter in the orientation of the T-axes, the P-axes are very consistent, with the combined strain tensor having an orientation of the maximum shortening axis at N143°E. The combined moment tensor, however, is far from a double couple, showing a very high fclvd of 0.4 and an oblate tensor shape, with a k value of 0.132. This k-value is the lowest value of all obtained solutions, showing the dominance of the shortening deformation tensor.

The inversion of the 11 mechanisms indicates a thrust-faulting stress regime (Fig. 7 AL) with σ1 at N140°E, which activates NE-SW striking thrust faults and left-lateral N-S and NW-SE striking right-lateral east-west striking strike-slip faults. The solution is very similar to that obtained for the WCS, showing that this type of stresses predominates throughout the SW corner of Iberia, to the west of the Betic front. This observation, together with the absence of thrust faulting stresses in the Iberian Betic foreland, indicates that one of the effects of the emplacement of the Alboran Domain to the W was the mechanical decoupling between Iberia and Africa. .

5.13 EB Eastern Betics

The easternmost part of the Betics shows a significant level of seismic activity. This area was affected by extensional tectonics during the opening of the Algero-Balearic Basin throughout the Miocene, the most significant extensional episode occurring in the Serravallian-Tortonian (Comas et al., 1999). Although it may have maintained a certain transcurrent character (Montenat and Ott d'Estevou, 1999). Since the Late Miocene, the dominant tectonics in the region have been characterized by shortening, resulting in the tectonic inversion of the Miocene basins (Sanz de Galdeano, 1990; Martínez-Díaz, 1998). The active continental indentation of the Águilas Arc to the nortwest is related to this shortening, which is linked to the collision of Africa and Eurasia, in which the arc forms part of the African crust (Ercilla et al., 2022; Tendero, 2022). The overthrusting arc is bounded to the E by the right-lateral strike-slip Mazarrón Fault (25) and to the W by the left-lateral strike-slip Palomares Fault (26). The latter extends southwestwards on the Serrata-Carboneras Fault (27) to the offshore Alborán Sea. The indentation implies a progressive tilting towards the SE of the whole arc (Ercilla et al., 2022; Tendero-Salmerón, 2022). In the frontal part of the arc, once in the Iberian crust, the deformation is accommodated in a left-lateral NE-SW transpressional corridor, the Eastern Betic Shear Zone (EBSZ), specifically the Alhama Fault (28), in continuity with the Trans-Alboran Transpressional Shear Zone (TASZ). It is in this shear zone that the most active faults of the Iberian Peninsula are found, with deformation rates between 0.5 - 1.5 mm/yr as indicated by palaeoseismological and geodetic methods (Herrero-Barbero et al., 2020; Gomez-Novell et al. 2022, Moreno et al., 2015, Echeverría et al., 2015, Martín-Banda et al., 2016). The simultaneous activity of these two macrostructures implies the presence of a deformation partitioning process (s.s) potentially with a certain degree of mechanical decoupling between the African and Iberian crusts.

The focal mechanisms in this tectonic zone are dominantly strike-slip and reverse events, with the most frequent having a certain oblique character, while some normal faulting events with a strike-slip component are also present. The minimum rotation angle between the strike-slip moment tensor and the extensional moment tensor is about 47º, indicating the predominance of a transcurrent character in the normal mechanisms (see Appendix). The combination of all the mechanisms gives rise to an oblate-shaped strain tensor, dominated by shortening, with fclvd values of 0.21 and a k value of 0.46. The P axis has an N172°E orientation, although the P axes of all mechanisms have a large scatter, which is controlled by the location of the events (see Appendix). This variability of the shortening axes may be influenced by the presence of large crustal structures that generate local block rotations (Martínez-Díaz, 2002) or by local deformation distribution patterns in the area (Alonso-Henar et al., 2019).

The inversion of the 47 focal mechanisms (Fig. 7 EB) provides a thrust-to-strike-slip faulting stress regime with σ1 at N171E, which can activate NE-SW to ENE-WSW striking thrust faults, as well as right-lateral NW-SE and left-lateral NNE-SSW striking strike-slip faults. There are also three NW-SE striking normal fault mechanisms in the area, which have a common σ3 (NE). This stress tensor solution explains the simultaneous movement of the Aguilas Arch and Alhama fault (28).

5.14 WAA Western Alcaraz Arch

This tectonic zone includes the westernmost part of the Alcaraz (or Prebetic) arch and a sector of the Guadix Basin, which has recorded intense seismic activity in recent years. The structural morphology is like that of other arcs in the Betics (Águilas) and the Alborán Sea, which are interpreted as resulting from as tectonic indentation processes, in this case , incipient (Tendero-Salmerón, 2022). The seismicity is concentrated along two NW-SE to ESE-WNW right-lateral strike-slip faults, the Tiscar and Guadiana Menor (29) faults (Tendero-Salmerón et al., 2020), which affect Quaternary materials and the Cenozoic sediments of the Guadalquivir Cenozoic Basin. The Torreperogil - Sabiote seismic series, characterized by strike-slip focal mechanisms, also appears to be related to faults possibly rooted in the basement (Pedrera et al., 2013). To the south, the intramountain Guadix Basin (30) , with a general NW-SE trend, appears to be filled with Tortonian to Pleistocene sediments (Pla-Pueyo et al. 2009) bounded by NW-SE normal faults (Alfaro, et al., 2008; Sanz de Galdeano et al., 2012).

Of the 14 focal mechanisms, two are normal faulting events (in the Guadix Basin) and the rest are strike-slip events (also one in Guadix). The orientation of the T axes in both types of mechanisms is consistent, with the minimum rotation angle between strike-slip and normal events being close to 90°. The combined strain tensor has a prolate form, dominated by the T axis, with an fclvd value of -0.23 and a k of 2.3. The orientation of the T axis is N052°E, while the P axis has an orientation of N142°E. The stress tensor obtained (Fig. 7 WAA) by inversion indicates a strike-slip stress regime with a normal component, characterized by σ1 at N153°E. This stress regime activates left lateral N-S and right lateral ESE-WNW strike-slip faults, as well as NW-SE normal faults. The inferred stress tensor is like that obtained by Tendero-Salmerón et al. (2020) from 5 mechanisms in the Tiscar and Guadiana Menor faults (shear with σ1 at N143°E).

5.15 Granada Basin

Within the tectonic context of NW-SE convergence between Africa and Eurasia (Iberia), as well as the westward emplacement of the Alboran Domain, accompanied by the rollback of the southern Iberian slab, the presence of NW-SE extensional basins within the orogen appears to be kinematically necessary. The easternmost part of the Betic Orogen is dominated by processes of thrust arc indentation with tectonic transport to the NW (Tendero-Salmerón 2022), while the westernmost arc formed by the Betic and Rif arcs surrounding the Strait of Gibraltar is located to the W. This kinematics is supported by the presence of a NW-SE extensional basin within the orogen, which is dominated by the presence of NW-SE normal faults related to radial extension (Reicherter and Peters, 2005). This kinematics is confirmed by GPS data (Cannavò and Palano 2016; Neres et al., 2018a; Neres et al., 2019). The boundary between these two zones within the Betic Orogen is marked by extensional basins aligned and bounded by NW-SE normal faults, such as the Guadix fault in WAA and by the Granada Basin. The age of the deformation of the Granada basin is Upper Miocene to present, defining a seismicity corridor approximately 300 km wide (Galindo-Zaldivar et al., 1999). The most prominent faults here are the Granada (31), Sierra Elvira-Dílar (31) and Padul-Dúrcal (32) faults (Sanz de Galdeano et al., 2012).

The focal mechanisms in the Granada Basin are extensional and cluster into two families, whose T axis orientations form an angle of 30-40° with each other. The combined moment tensor is of oblate type, dominated by vertical shortening and with fclvd values of 0.08 and k of 0.768. The T axis has an orientation N048°E, and the B axis of N139°E; which is consistent with the dominant shortenings in the surrounding zones.

The seismic sequence that occurred in 2021 enabled the determination of the stress tensor from 5 focal mechanisms of normal faulting stress regime (R=0.28), with σ3 at N049°E (Madarieta-Txurruka et al., 2022). In our stress inversion (Fig. 7 GB), we utilized 16 focal mechanisms that yield a highly consistent triaxial normal faulting stress regime with σ3 striking at N033°E. Therefore, this stress orientation is congruent with that obtained to the E (WAA and EB), facilitating the emplacement of WB to the W.

5.16 NA Northern Alboran

The offshore deformation of the N margin of the Alborán Sea has been explained as a result of the ongoing slab rollback in the Alborán Domain, in the Gibraltar Arc (Betics-Rif), and of the indentation tectonics that predominates to the east and south, giving rise to a complex faulting pattern (Galindo-Zaldivar et al., 2022). On the other hand, in the easternmost part of this zone, the most important tectonic structure is the Carboneras Fault (27), a continuation of the Palomares Fault (26) (EB). This structure has an NE-SW strike, extends offshore and has been active since the Late Miocene until the present. This fault shows a left-lateral strike-slip movement that occurs at a rate of 1.3 mm/yr (Moreno et al., 2015) and an offset of more than 15 km (Gràcia et al., 2006; Rutter et al., 2012), in which 4 palaeoseismic events have been identified (Masana et al., 2018). Among the 42 focal mechanisms analysed, we find reverse and normal solutions, but mainly strike-slip ones. Except for 3 normal faulting focal mechanisms indicating N-S extension, the others show a T (or B) axis towards NE-SW. The shortening axes in the focal mechanisms are very consistent, with orientations between N130°E - and N180°E. The minimum rotation angles between the normal faulting mechanisms and the strike-slip and thrust mechanisms are high, ranging from 90-100°; in contrast, the minimum rotation angle between the reverse and strike-slip mechanisms is approximately 50°, ndicating a strong strike-slip component in the thrust earthquakes (see Appendix). The combined moment tensor is a slightly prolate strike-slip deformation tensor, with a k value of 1.63 and an fclvd of -0.14. The extensional stress axis, which would be dominant in the deformation of the zone, has an N065°E trend, while the shortening axis has an N154°E trend. The stress inversion result is alike those of WAA and EB. The obtained solution (Fig. 7 NA) does not seem to reflect the structural complexity indicated by the field and GPS data (Galindo-Zaldivar et al., 2022). The solution exhibits a strike-slip stress regime with a normal component, characterized by σ1 in N149°E and σ3 in N064°E. Therefore, in this zone, the indentation process would predominate over the rollback process.

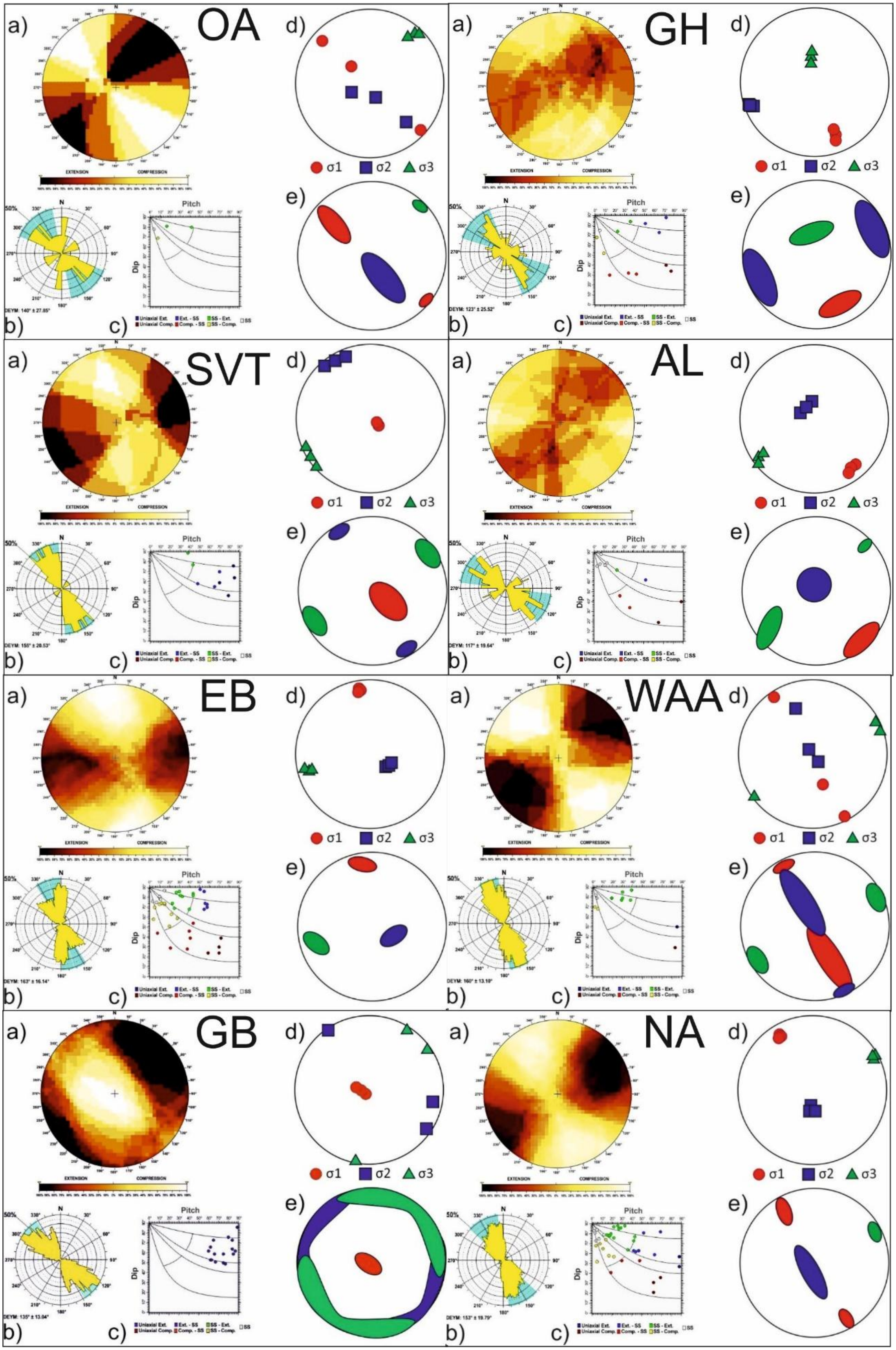
a)
OA
d)
σ1 σ2 σ3
e)
EXTENSION
COMPRESSION
50%
N
b)
DEYM: 140° ± 27.85°
c)
Pitch
Dip
Uniaxial Ext.
Ext. - SS
SS - Ext.
SS
Uniaxial Comp.
Comp. - SS
SS - Comp.
GH
DEYM: 123° ± 25.52°
SVT
DEYM: 155° ± 28.53°
AL
DEYM: 117° ± 19.64°
EB
DEYM: 163° ± 16.14°
WAA
DEYM: 160° ± 13.10°
GB
DEYM: 135° ± 13.04°
NA
DEYM: 153° ± 19.79°

Figure 7: Results of the stress-strain analyses for different zones: a) Right Dihedra solution. b) Rose diagram of the Deys obtained from the Slip model. C) Pitch/Dip plot for the neo-formed nodal planes obtained from the Slip Model. d) Stress Inversion Results. e) Variability of the three main stress axes of the stress inversion. OA Offshore Atlantic; GH Gorringe-Horseshoe; SVT Southern Valencia Trough; AL Algarve; EB Eastern Betics; WAA Western Alcaraz Arch; GB Granada Basin; NA Northern Alboran.

5.17 AR Alboran Ridge

The most prominent structures in the Alborán Sea, in the central part of the Alborán Domain, are the Alborán Ridge (33), a crustal pop-up with the main tectonic transport to the NW and outcropping Neogene volcanic materials, the left-lateral Al Idrissi Fault (34) and the right-lateral Yusuf strike-slip Fault (35). The three structures draw an indentor with similar kinematics to those of Águilas and Cazorla (in EB and WAA) (e.g., Tendero-Salmerón, 2022). Since the Late Miocene, magmatic intrusions in the Alborán Ridge seem to have acted as a backstop that favoured its uplift relative to the indentation (Tendero-Salmerón, 2022). The continental crust to the S of the aforementioned structures appears to belong to the African plate, so these faults are considered to constitute the active plate boundary between Africa and Eurasia (Iberia), with the Yusuf Fault (35) extending to the Tell Mountains orogen in Algeria (Martínez-García. 2012; Gómez de la Peña, 2017). The seismic crisis of 2016, which included an Mw 6.4 earthquake located in the southern limit of the Al Idrissi fault system (34), enabled defining its trace by connecting it with the Bokkoya and Trougout Faults, which enters the African onshore and connects with the Nekor Fault (36). It is therefore a very recent plate boundary (Gràcia et al., 2019). The seismic sequence indicates the presence of restraining steps along the strike-slip trace (Stich et al., 2020).

The focal mechanisms in this tectonic zone include pure reverse faulting, oblique faulting, with mainly normal component, and normal faulting with strike-slip component. The minimum rotation angles between the three fault types are high, showing the activation of different structures in response to a consistent strain tensor. The orientation of the T axes is very congruent in all mechanisms, with directions between N050°E and N080°E. The shortening axes show somewhat more variability. The combined moment tensor has an oblate shape, with k 0.519 and fclvd 0.19, and is dominated by shortening with an N157°E orientation. The mean T strain axis is N069°E.

The inversion of the 63 focal mechanisms (Fig. 8 AR) indicates a transpressive strike-slip faulting stress regime, with σ1 at N161°E, which activates mostly N-S to NNE-SSW left-lateral faults, NW-SW right-lateral strike-slip faults and E-W to ENE-WSW thrust faults. There are also 5 normal faulting mechanisms with nodal planes sub-parallel to the inferred σ1 orientation, indicating the presence of secondary normal faulting steps along faults in the principal direction. The stress solution is intermediate to that of the Águilas (EB) and Alcaraz (WAA) indentors.

5.18 ALH Al Hoceima

The S sector of the Alboran Domain, on the N coast of Morocco, shows significant seismic activity (2004 Mw 6.4 and 1994 Mw 5.9 earthquakes) in the Al Hoceima area (37) with ruptures up to 20 km, which allowed us to infer an associated strike-slip stress regime (R=0.5) with σ1 at N161°E and σ3 at N071°E (van der Woerd et al., 2014). However, the Trougout (N171°E) and Bokkoya (N030°E) faults, which continue offshore in AR, together with the Bousekkour-Aghbal (N020°E) fault, bound the Plio-Quaternary Nekor basin and define a transtensional area between the Nekor (36) and Al-Idrissi (34) faults (d'Acremont, 2014). Backstripping analyses of the sediments of Al Hoceima Bay during the last 280 kyr indicate a westward migration of deformation with vertical throw rates of 0.47 mm/year because of the interaction between the northwesternwards movement of the Alboran indentor and the south-westward displacement of the Rif (Tendero-Salmerón, 2021). Further to the E, the NE-SW Kert and Nador faults (38) appear to have a normal component (Ammar et al., 2007), although the considered focal mechanisms are mainly strike-slip faults like those of Al Hoceima. Therefore, we grouped them into a single population. The focal mechanisms indicate mainly strike-slip and normal faulting, with a significant population of oblique faults with both components. Reverse-type events with strike-slip components are also present. All focal mechanisms exhibit highly consistent axes of maximum shortening and horizontal extension, with minimal variability (see supplementary information). The combined moment tensor indicates a directional deformation with an extension component close to a double couple, with an fclvd value of -0.08 and a k value of 1.3. The P axis of the combined moment tensor has an orientation N143°E and the T axis N060°E.

As there are more normal fault-type focal mechanisms in this population than in AR, the stress tensor shows a strike-slip faulting solution (Fig. 8 ALH) with a normal component, with σ1 at N152°E and σ3 at N064°E. Therefore, the tectonics in this zone is transtensional.

5.19 WTA-ETA Western-Eastern Tell Atlas

The Algerian Tell Atlas is the most seismically active area in the western Mediterranean, including, among others the, 1980 El Asnam, Mw 7.3, earthquake, which occurred on a 36 km long thrust linked to a NE-SW fault propagation anticline (39). The focal mechanism of this earthquake indicated the presence of a NW-dipping thrust plane (Meghraoui et al., 1986). In general, this is in good agreement with the tectonics of the range, characterized by dipping faults related to fault adaptation-propagation anticlines. These main neotectonic structures correspond to E-W striking to NE-SW striking thrusts that cut Quaternary rocks. The main intramountain basins are the Cheliff, Mitidja, Soummam, Hodna and Constantine basins (Maouche et al., 2019 and references therein). The coast shows evidence of folding and uplift, with marine terraces uplifted during the Pleistocene and Holocene (Maouche et al., 2011).

In the WTA, the most frequent focal mechanisms are reverse, coexisting with strike-slip and some normal faulting, all of them kinematically compatible with NW-SE horizontal shortening axes. The combined moment tensor is oblate inverse, with k = 0.328 and fclvd 0.28, showing the predominance of horizontal shortening. The P axis has an orientation N143°E and the B axis N050°E. Further east, the population of focal mechanisms is similar, mainly with thrusting events. The combined moment tensor is therefore of a shortening type and oblate, although it is closer to the double couple, with k = 0.767 and fclvd = 0.08. The P axis is oriented N155°E and the B axis N069°E; therefore, the shortening is more northerly in this area than it is further to the west.

Because the inferred moment tensor vectors and shortening directions are not coaxial, it has recently been suggested that, from the Alboran domain to the E, transpressional tectonics predominates, activating E-W striking right-lateral strike-slip faults and NE-SW striking thrusts (Meghraoui and Pondrelli, 2012). Stress inversions based on earthquake focal mechanisms indicate that the deformation is accommodated by E-W striking reverse-strike-slip faults in the Eastern Tell. In contrast, the Western Tell is dominated by strike-slip faults (Soumaya et al., 2018). The stress inversions obtained in this study (Fig. 8 WTA, ETA) show a very similar σ1 orientation for the eastern and western of the Tell-Atlas: N149°E (east) and N145°E (east), with a thrust-faulting stress regime to the east, and with a larger strike-slip component in the west, contrary to Soumaya et al. (2018). Both solutions activate NE-SW striking thrust faults, NW-SE right-lateral and N-S left-lateral strike-slip faults.

5.20 GC Gulf of Cádiz

The Gulf of Cadiz appears to be dominated by the south-westward movement of the Betic-Rif orogen, which has built up a sediment stack that is up to 12 km thick in an accretionary prism characterised by W-vergent thrust-spreading anticlines (40). The prism is related to the subduction of the S margin of Iberia below the Rif-Betic-Alboran microplate. Subduction appears to have slowed down significantly during the last 5 Myr, although deformation in the accretionary prism still affects recent sediments (Gutscher et al., 2012). Thermo-mechanical modelling indicates that although the subduction process has ceased, deep slab motion still induces a mantle flow that produces a W-directed basal drag of the Alboran domain lithosphere (Gea et al., 2023; Neres et al., 2019). Some of the selected focal mechanisms are located in the S margin of the Algarve Basin, S of the Portimão Bank (AL) (Ramos et al., 2015; Neres et al, 2018b), providing a fairly homogeneous population.

The focal mechanisms in this tectonic zone are mainly strike-slip, although normal and reverse faulting events are also present. The combination of the mechanisms results in a directional seismic moment tensor but with an oblate shape, characterized by k = 0.417 and fclvd = 0.24. The P-axis has an orientation N161°E and the T-axis N066°E. The inversion provides a strike-slip stress regime (Fig. 8 GC) with σ1 at N150°E, with less thrusting component than that obtained for AL, GH and WCS. Therefore, it does not seem that there is significant seismicity related to thrusting with tectonic transport to the W, but rather to the SE or NW.

5.21 WB Western Betics

The emplacement of the Rif-Betics-Alboran Domain to the W during the Early Middle Miocene, together with the NW-SE oblique convergence between Eurasia and Africa, has influenced the structuring of the Betic Orogen. However, since the Upper Miocene, it is the latter process that seems to have dominated (Ruiz-Constán et al., 2011). The NW Betic Mountain front is the most seismically active sector.Although seismogenic structures do not outcrop at the surface moderate-depth earthquakes indicate the presence of NE-SW thrusts with some related tear faults (41) (Ruiz-Constan 2009).

In our analysis, we used only earthquakes at crustal depths. The population of focal mechanisms is dominated by strike-slip faulting, with several of these mechanisms exhibiting an oblique orientation and a reverse component. However, a significant number of thrust faulting events are also observed. The orientations of the axes of maximum shortening and horizontal extension are scattered, characterised by two families: a major one with a shortening direction N120°E-N150°E and a minor one with a N-S shortening direction. The combination of the focal mechanisms gives rise to a shortening-directional seismic moment tensor with an oblate shape, exhibiting values of k 0.376 and fclvd 0.26. The shortening axis P has an orientation of N143°E and the B axis N046°E, although with a 28° plunge.

The total population of32 mechanisms provides a well-constrained stress inversion result (Fig. 8 WB). The inferred stress tensor indicates a strike-slip stress regime with σ1 at N139°E, which activates NE-SW striking thrusts and strike-slip faults. These faults exhibit right-lateral offset when striking east-northeast to west-southwest (ENE-WSW) and left-lateral offset when striking north-northeast to south-southwest (NNE-SSW).

Stress inversions in this area are considered in terms of the hypocentral depth, as the deepest stresses/deformations could be related to the Iberian slab under the Alboran Domain. Ruiz-Constán et al. (2012) obtained σ1 trends for shallow seismicity at N166°E (4 mechanisms) and N018°E (4 mechanisms). For the intermediate earthquakes, they obtained a σ1 trend between N113°E and N126°E, encompassing 29 mechanisms.). The σ1 trend is located more towards the ESE-WSW concerning the surrounding areas, likely influenced by the remnant effect of the slab (Gea et al., 2023), which is more evident at depth (Ruiz-Constán et al., 2012). To test this effect, we inverted the 7 focal mechanisms corresponding to earthquakes with hypocentral depths of more than 20 km in this zone (WBD), obtaining a σ1 of N114°E, more E-W than the shallow ones (Fig. 8 WB>20). Therefore, our results confirm that the slab effect is more pronounced at greater depths, being negligible in shallow earthquakes.

5.22 BA Betics Antequera

Between the Granada Basin (GB) and the thrusts at the NW edge of the Betics (WB), there is a 70 km long right-lateral transpressional brittle-ductile shear zone. The Torcal Shear Zone (42), that has been active from the Late Miocene until the Quaternary (Barcos et al., 2015). In 1989, a seismic series (117 earthquakes) was reported between Loja and Palenciana, which indicated that the fault zone had a strike of N070°E-N080°E (Posadas et al., 1993). From the focal mechanisms obtained for this crisis, a strike-slip stress regime with σ1 at N135E was previously determined by Vadillo (1999).

The focal mechanisms in this tectonic zone are of strike-slip type with an extensional component, as observed in 5 events. The combination of these events results in a strain tensor very close to a double couple, with a value of k = 1.16 and fclvd -= 0.04. The orientation of the P axis is N125°E and the T axis N028°E. The inversion of the 5 focal mechanisms (Fig. 8 BA) reveals a strike-slip stress regime with a normal component, characterized by σ1 at N105°E, which activates right-lateral strike-slip-normal (transtensional) faults. This σ1 orientation is more like to that of the WB than to those of the other adjacent areas and could indicate a greater effect of the rollback process of the Iberian slab, from here to the west. The extension-normal faulting in the Granada Basin (GB) may therefore be explained by the greater effect of the westernward remanent movement of the Alboran Domain, which is partially decoupled from the indentation zone of the Betic arcs further to the east.

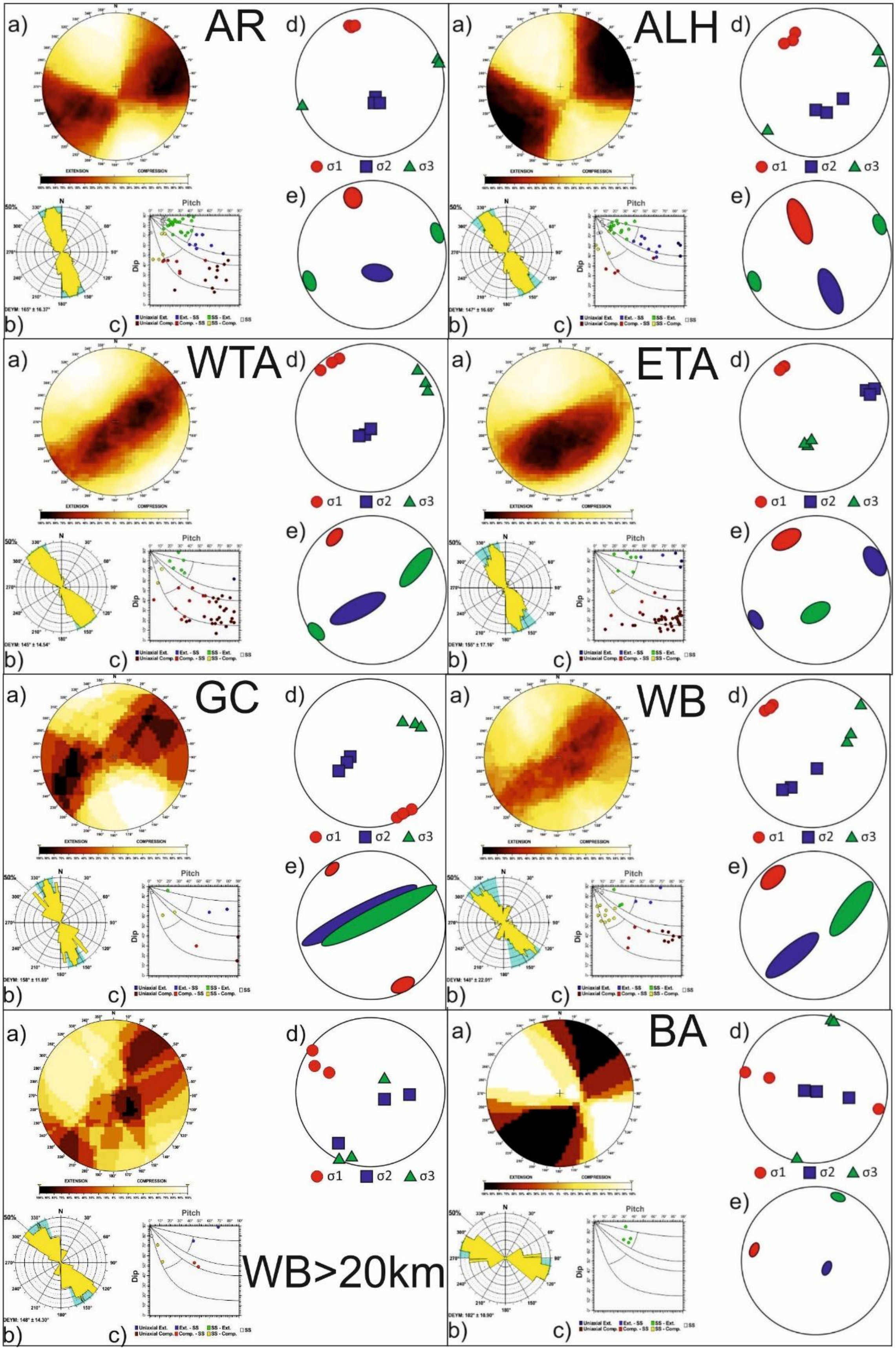
AR
ALH
WTA
ETA
GC
WB
WB>20km
BA
a)
b)
c)
d)
e)
N
EXTENSION
COMPRESSION
50%
Pitch
Dip
σ1
σ2
σ3
Uniaxial Ext.
Ext. - SS
SS - Ext.
SS
Uniaxial Comp.
Comp. - SS
SS - Comp.
DEYM: 165° ± 16.37°
DEYM: 147° ± 16.65°
DEYM: 145° ± 14.54°
DEYM: 155° ± 17.16°
DEYM: 158° ± 11.69°
DEYM: 140° ± 22.01°
DEYM: 148° ± 14.30°
DEYM: 102° ± 10.90°

Figure 8: Results of the stress-strain analyses for different zones: a) Right Dihedra solution. b) Rose diagram of the Deys obtained from the Slip model. C) Pitch/Dip plot for the neo-formed nodal planes obtained from the Slip Model. d) Stress Inversion Results. e) Variability of the three principal stress axes of the stress inversion. AR Alboran Ridge; ALH Al Hoceima; WTA Western Tell Atlas; ETA Eastern Tell Atlas; GC Gulf of Cádiz; WB Western Betics (WB depth > 20 km); BA Betics Antequera.

6 Stress map of Greater Iberia

The new compilation of earthquake focal mechanisms and the results from the stress inversions can be used to update the stress map of Iberia using the quality ranking scheme of the World Stress Map (WSM) project. The WSM is the global resource for stress information on the present-day stress field of the Earth's crust (Heidbach, 2016; Heidbach et al., 2018; Zoback, 1992) and compiles the orientation of maximum horizontal stress σ_{Hmax} from a wide range of stress indicators such as earthquake focal mechanism solutions (FMS), drilling-induced tensile fractures (DIF), borehole breakouts (BO), hydraulic fracturing tests (HF), overcoring (OC) as well as geologic data from seismogenic fault-slip analysis (GFI, GFS) and volcanic vent alignments (GVA) (Amadei and Stephansson, 1997; Ljunggren et al., 2003; Sperner et al., 2003). The stress information is compiled in a standardized data format and quality-ranked to make data from very different methods comparable (Heidbach et al., 2010). The various stress indicators reflect the in-situ stress of very different rock volumes ranging from 10^{-3} to 10^{9} m^{3}. Furthermore, except for the earthquake focal mechanisms and a few very deep boreholes, all stress indicators sample only the stress patterns within the upper 6 km of the Earth's crust, with deep boreholes as a major contributor. The most common visualization of stress data is through stress maps where data from depths between 0 and 40 km is integrated (Heidbach et al., 2004; Heidbach and Höhne, 2008) assuming that the σ_{Hmax} orientation does not change significantly with depth. This assumption was tested qualitatively at the beginning of the WSM project (Zoback, 1992) and confirmed later with significantly higher data density on global (Heidbach et al., 2018) and regional scales (Pierdominici and Heidbach, 2012; Rajabi et al., 2017a).

For the new stress map of Greater Iberia, we re-evaluate all data records from geological data (n=141), borehole breakouts (n=129), overcoring (n=16), and hydraulic fracturing (n=5) and combine these with the σHmax orientations derived from the new compilation of earth-quake focal mechanisms (FMS) and stress inversion results (FMF) obtained in this study. Given that the majority of the WSM data records have not been revisited for almost 30 years, our re-evaluation resulted in a reduction of data records due to double entries and typos (from n=295 to n=271) and down-ranking in quality due to a stricter data assessment. There-fore, the number of stress data records with A-C quality decreased from n=172 to n=132. A-C quality means that the σ_{Hmax} orientation is reliable within ± 25°, D quality data records are only reliable within ± 40° and thus should be used with caution (Rajabi et al., 2024; Tingay et al., 2006; Tingay et al., 2005). E-quality data are poor in quality and X-quality data have not sufficient or missing information to assign a quality. The latter is a new assignment class that is used already in the new WSM quality ranking for stress magnitude data records (Morawietz et al., 2020) and will be also used in the next WSM database release for stress orientation data records (Table 6).

Type/Quality	A	B	C	D	E	X	Total

FMS	0	0	456	0	86	0	**542**
FMF	5	15	0	0	11	18	**49**
FMA	0	0	0	24	0	1	**25**
BO	8	30	36	38	5	5	**122**
HF	1	0	1	1	0	0	**3**
OC	0	0	0	2	0	14	**16**
GFS	0	0	0	12	0	0	**12**
GFI	0	8	48	10	22	30	**118**
Total	**14**	**53**	**541**	**53**	**148**	**68**	**887**

Table 6: Overview of data quality and stress indicators in the new compilation of stress information shown in Fig. 10. Note that most of the downranking of data records from borehole breakouts (BO), hydraulic fracturing (HF), overcoring (OC) and geological indicator (GFI, GFS) are due to missing information in the papers and reports where data are presented. The other abbreviations are FMS for single focal mechanisms, FMF for stress inversion from population of focal mechanisms, and FMA for composite focal mechanisms.

The resulting stress map shows that, at first order, the data records from boreholes agree with earthquake focal mechanisms data from greater depths. An exception is the borehole data in the Aquitaine Basins north of the Pyrenees where some σ_{Hmax} orientations from borehole breakouts confirm the prevailing WNW-ESE strike, but others show different orientations. These data result from a comprehensive study of 55 wells by Bell et al. (1992) and the authors discuss in great detail this somewhat controversial result of varying σ_{Hmax} orientations on local scales which has not been observed in other foreland basins (Reinecker et al., 2010; Reiter et al., 2014). However, for the remaining areas, there is an overall agreement between the σ_{Hmax} orientations inferred from borehole data in comparison with earthquake focal mechanisms results.

To analyze the prevailing σ_{Hmax} orientation pattern we estimate the mean σ_{Hmax} orientation on a 0.5° grid using the tool stress2grid from Ziegler and Heidbach (2019) with a 150 km search radius. For the estimation, a minimum of five data records is required within the search radius. Weights are applied considering data quality and distance to the grid point. The distance weight is cut off when the data record is within 15 km of the grid point to avoid an overrepresentation of data records close to the grid point. Furthermore, we distinguish the resulting mean σ_{Hmax} orientations according to their standard deviation SD. Dark grey bars in Fig. 9 denote mean σ_{Hmax} orientations with SD $\leq 25°$, light grey ones with SD $> 25°$. The resulting mean σ_{Hmax} orientation in Fig. 9 shows that in particular in the center of Iberia, the stress pattern does not show a clear trend, in contrast to mostly all the other regions, with the exception of the Pyrenees. This is expressed in rotations of the mean σ_{Hmax} orientation and the significantly higher SD values in center of Spain. The changes of the mean σ_{Hmax} orientation on short scales could be either due to low data density, which allows for a single outlier or local deviation from the stress pattern has a high impact on the mean trend, or to the stress pattern being indeed quite variable, for example due to low anisotropy of the horizontal stresses which, results in less stable horizontal stress orientations (Heidbach et al., 2007; Lundstern and Zoback, 2020; Rajabi et al., 2017b).

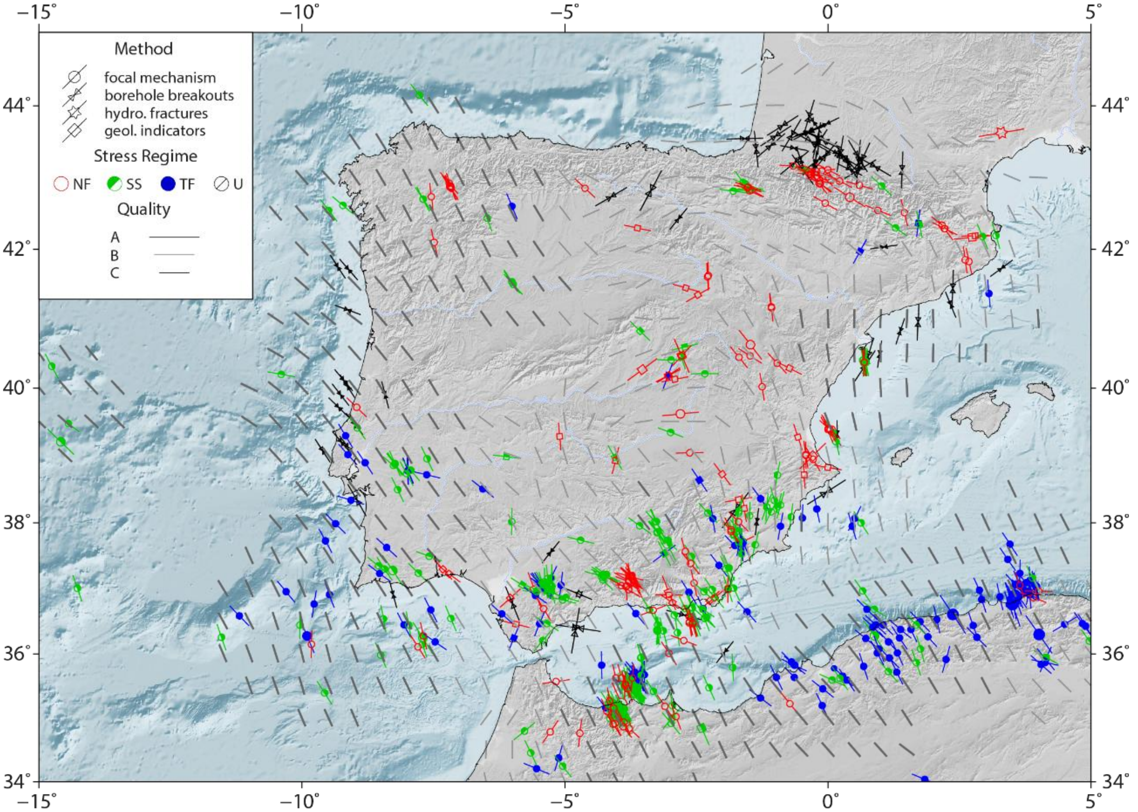

Figure 9: Stress map of Greater Iberia based on A-C quality data records from this study and from re-evaluated data of the WSM database release 2016 (*Heidbach et al.*, 2016). Plotted is the orientation of maximum horizontal stress σ_{Hmax} for depths between 0-40 km. See the inset legend for details on data types, stress regime (NF= normal faulting, SS= strike-slip, TF= thrust faulting, U= unknown). Data symbols indicate the type of stress indicator and line length are proportional to data quality. Grey bars on a 0.5° grid show the mean σ_{Hmax} orientation that is estimated with a search radius of 150 km using weights for data quality and distance to the grid point. Dark grey bars on the grid show mean σ_{Hmax} orientations with a standard deviation ≤ 25°, light grey bars with standard deviation > 25°. Topography and bathymetry is taken from SRTM15+ (Tozer et al., 2019)

7 Discussion

Our analysis focuses on the Iberian Peninsula, excluding the Gloria Fault, which lies between the Terceira Ridge in the Azores Islands and the Gorringe Bank. The tectonic stresses that generate seismicity are related to strike-slip faults (e.g., de Vicente et al., 2008).

As shown in Fig. 10a, the combined tensors have distinct characteristics depending on their position within the tectonic context. Thus, in the plate boundary zone, the tensors present typical characteristics of reverse or reverse directional faults with positive fclvd values. In contrast, the tensors of the Pyrenees and the central-eastern Iberian Peninsula display normal or normal-directional focal mechanisms with negative fclvd values. An exception to this rule is the combined tensor of the Granada Basin, with a very pure normal faulting tensor.

When we consider the combined moment tensor by rupture type, the reverse component (Fig. 10b) shows the predominant NW-SE shortening orientation in the area, with nodal planes of approximately N040°E to N070°E strike. This broadly northeast to east-northeast orientation of the moment tensor nodal planes strike is found in all combined plate boundary tensors from northern Algeria to the Gulf of Cádiz. Only the combined tensor at the eastern tip of the Betics (EB) has an orientation of its nodal planes that is more east-west (E-W), corresponding to a north-south (N-S) shortening. These fault orientations are found in the northern sector of the Arco de Águilas and the Bajo Segura Fault system. In the north of the Iberian Peninsula, the seismic moment released in the form of reverse fault earthquakes is much smaller. They present oblique tensors whose P-axes are consistent with the regional shortening axes, which are more clearly marked on the combined strike-slip tensors in these cases.

The strike-slip combined tensors (Fig. 10c) present nodal planes oriented from N000°E to N050°E for the left-lateral kinematics, which is compatible with the NW-SE shortening orientation described above. All the strike-slip tensors exhibit these characteristics, except for thetesnor from the Western Pyrenees (WP) and Central Basins (CB) , which display right-lateral kinematics for NE-SW planes. These two cases are also characterised by E-W shortening axis orientations and prolate tensor shapes (K values > 1, fclvd < 0), having the highest K values together with the tensor from the northwest of the Iberian Peninsula (NWG). Although the strike-slip tensors are dominant throughout the peninsula (Fig. 10e), they are particularly relevant in the Trans-Alboran system.

Regarding the combined normal faulting tensors, we can find two groups. On the one hand, tensors whose extension axes have an orientation from E-W to NE-SW and on the other hand, those with an extension axis orientation N-S. The latter are found in the central and western Pyrenees (CP, WP), as well as in the central basins (CB). In the rest of the peninsula, the normal tensors present nodal planes whose orientation is approximately parallel to the axes of maximum horizontal shortening. The normal tensors are more significant in a band that connects the Al Hoceima area in North Africa to the central Pyrenees passing through the Iberian chain (Figs. 10d and 11b). Also, in the northwest of the Iberian Peninsula (NWG), normal faulting mechanisms have a predominant role in the combined tensor (Fig. 12b).

If we project the combined tensors in classification diagram (Fig. 10e), we see how most of them are tensors clearly located in the fields of pure rupture types, with a predominance of strike-slip tensors, often combination with compression or extension. If in the diagram we represent the combined tensors by rupture type for each zone (Fig. 10f) we see how the pure tensors are still dominant, which indicates that the combination between different rupture types takes place by permutation of the principal axes, being compatible with each other and therefore defining a distributed deformation.

The orientations of the principal axes for each zone are shown in Fig. 11a. NW-SE shortening is predominant in North Africa, the Alboran Sea, and the western half of the Iberian Peninsula. In the eastern part, the shortenings trends tend to be N-S, except in the areas where the extension is predominant (Fig. 11b), i.e. in the Pyrenees and the central basins, where the extension is N-S and therefore the maximum horizontal shortening is E-W.

For every zone for which we have determined focal mechanisms for the various faulting types, we computed the minimum rotation angle between pairs of tensors (Fig. 11 c). Most of the rotation angles are between 60° and 110°. These values are indicative of the activation of structures sharing a common strain tensor orientation, where permutations between the axes (rotations of 90o) take place, responding to a coherent tectonic framework. An example, of such process is the permutation between the shortening axis of reverse faults and the intermediate axis of normal faults. The results for the WVT zone deserve a special mention. They consist of the focal mechanisms related to the Castor Project seismic crisis, a natural gas submarine storage project (Villaseñor et al., 2020; Cesca et al., 2021). As can be seen, the rotation angle between the tensors of the different rupture types is very small, showing that the rupture type of all the events is similar and consists of oblique focal mechanisms located near the centre of the classification diagram (Fig. 10 f).

In Fig. 11 d, the combined tensors are represented in the Flinn-type diagram for moment tensors with the colour showing the k-value. The zones with prolate ellipsoids (K>1), located above the plane strain diagonal of the Flinn-type diagram, are those also characterised by a significant normal rupture component, these are the Pyrenean zones (EPCE, WP, NWG), the Valencia Trough (SVT) and the Central Basins (CB). These results evidence the relationship of these prolate ellipsoids with extensional and transtensional tectonic settings. On the other hand, the areas with oblate ellipsoids are those related to transpressional tectonic settings, mainly in the southwestern margin of the Iberian Peninsula (AL, GH, WB, GC, WCS). This relationship between of the strain tensor shape and the position with respect to the plate boundary is highlighted when we plot the k-value as a function of the latitude (Fig. 12). Near the plate boundary the shapes of the strain tensors are mainly oblate, with k < 1; and as we move away from the plate boundary the k values increase, with mostly prolate strain tensors to the north of the Betics (k > 1).

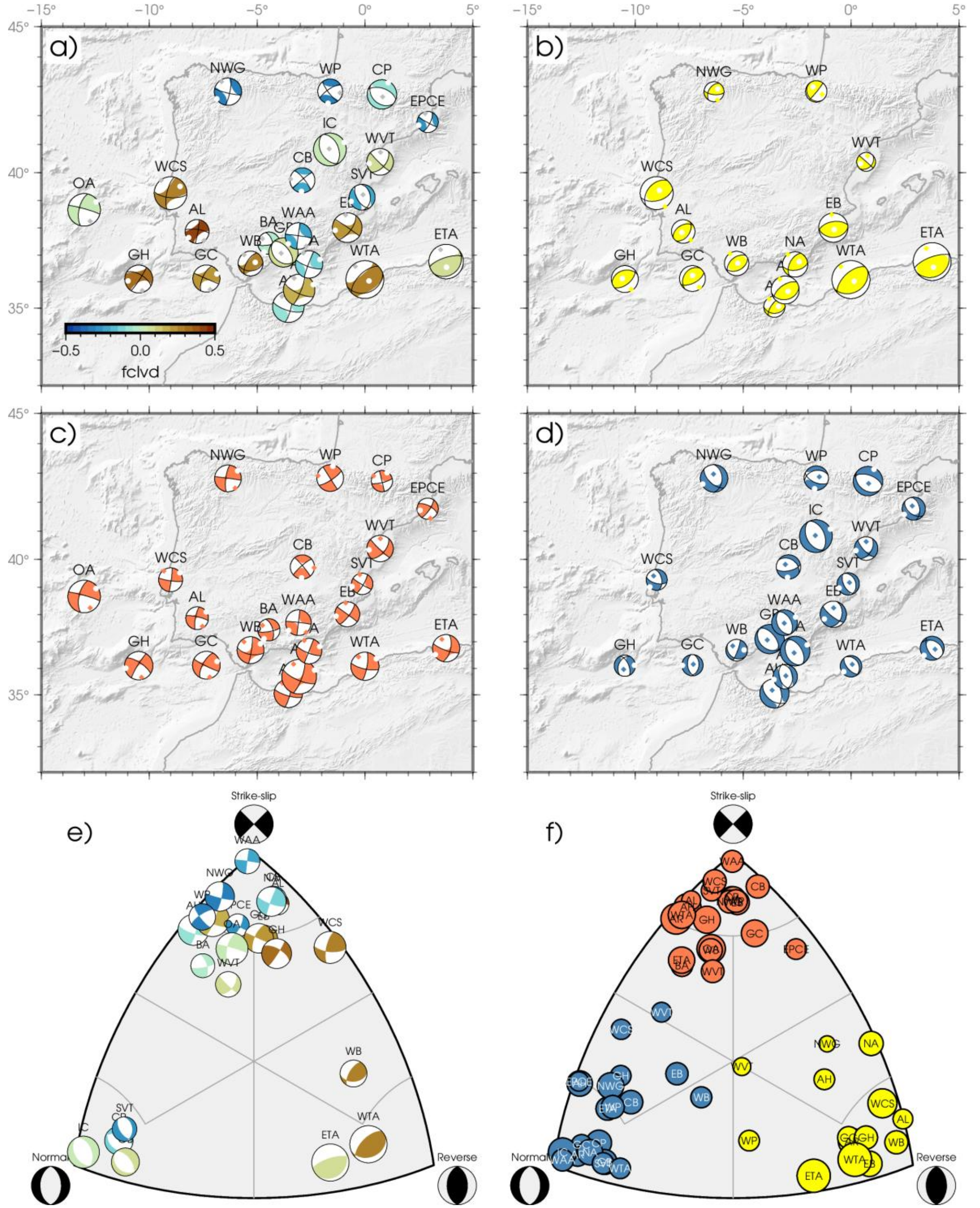

Figure 10: a) Combined strain focal mechanisms for each of the tectonic zones. The colour of the beach ball represents the compensated linear vector dipole factor fclvd. b) Combined focal mechanism for reverse faulting earthquakes in each zone. c) Combined focal mechanism for strike-slip earthquakes in each zone. d) Combined focal mechanism for normal earthquakes in each

zone. e) Focal mechanism classification diagram for the combined mechanisms shown in a). f) Focal mechanism classification diagram for the different rupture type combined mechanisms shown in b), c) and d).

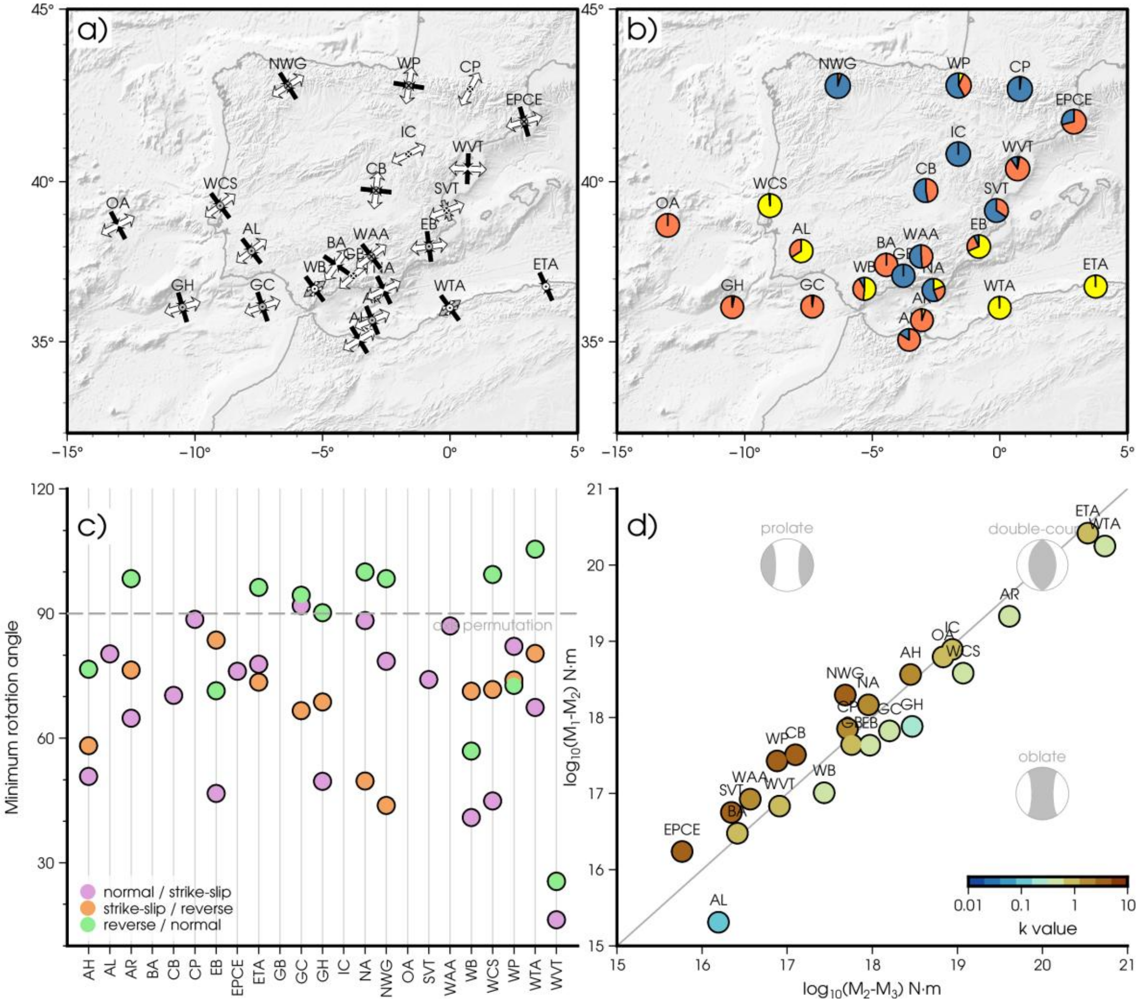

Figure 11: a) Strain principal directions derived from the combined moment tensors. Black shows the orientation of the shortening (P) axis; in white is shown the stretching axis (T) and grey the intermediate axis. The orientations are simplified showing only the trend of the principal axes and omitting the plunge. Note that the intermediate axis (in grey) can be a shortening or a stretching axis; when it is the vertical axis it is represented by a circle with a cross or with a dot respectively. b) Pie diagram showing the proportion of seismic moment released by strike-slip (red), reverse (yellow) and normal (blue) events on each zone. c) Representation of the minimum rotation angle (Kagan angle) between combined focal mechanisms for the different rupture types in each zone. A 90° angle represents a pure axes permutation. d) Flinn-like diagram showing the combined seismic moment strain tensor shape. The k-value is defined as (M1-M2)/(M2-M3).

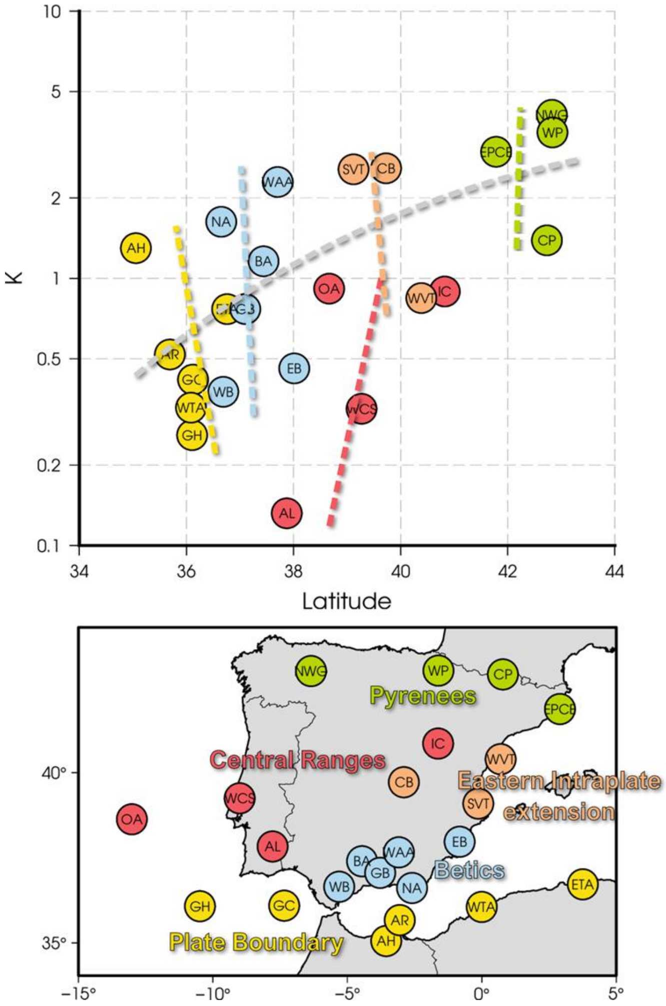

Figure 12: Relationship between the k-value of the strain tensor and the latitude of the zone. The colours are related to the tectonic setting as shown in the map. The coloured dashed lines show the trend of each population, while the grey dashed line shows the general trend of K-value increment with latitude.

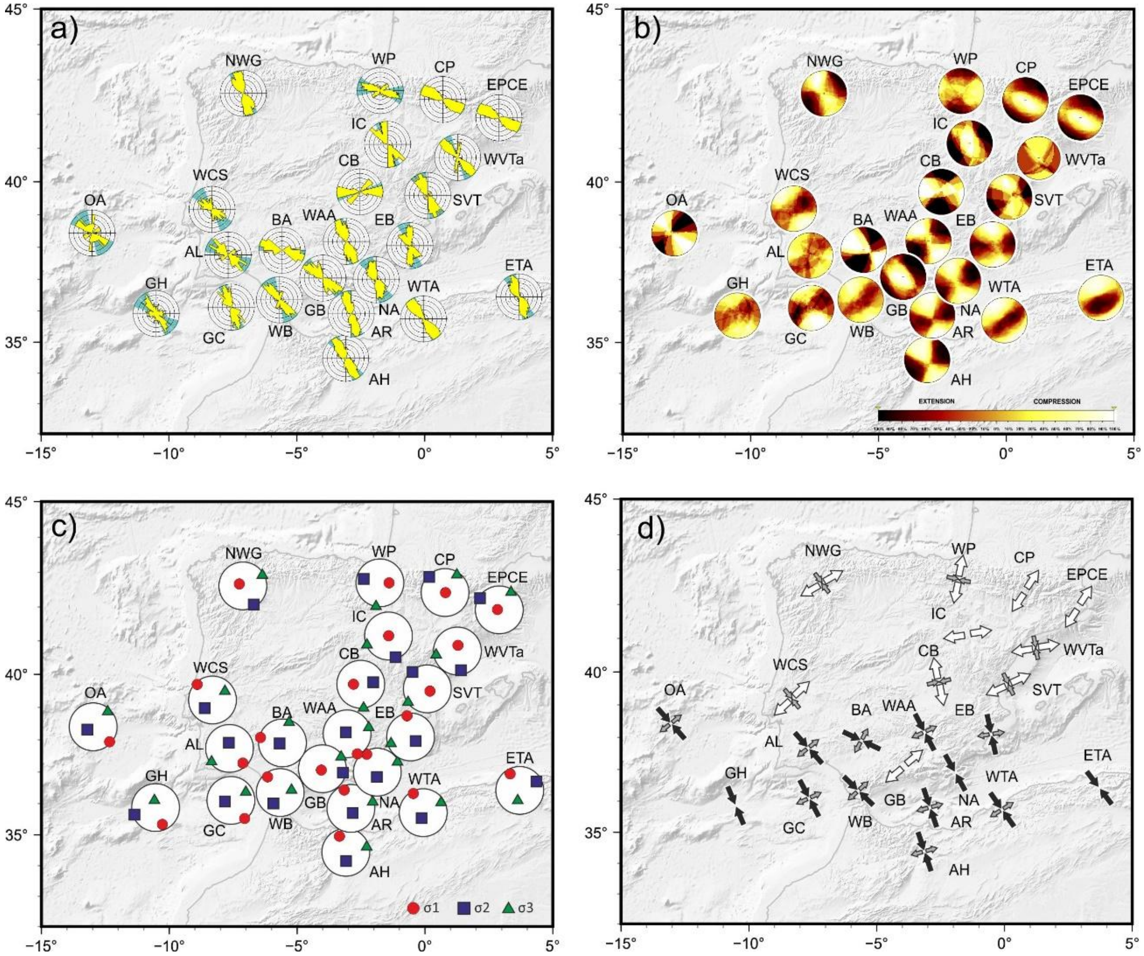

Figure 13: a) Deduced E_{Hmax} (Dey, maximum horizontal shortening / minimum horizontal extension) in every considered zone from the Slip Model. b) Combined Right Dihedra plots. c) Stress inversions from focal mechanism populations in all the zones. d) scaled sizes of the stress horizontal axes, σ_1 (black), σ_2 (grey) and σ_3 (white).

Results regarding the type of active deformation from the slip model analysis are shown in Fig. 3. The varying distribution of data densityresults in poorly defined interpolations in areas with low data. Nevertheless, the inferred S_{Hmax} (Dey, maximum horizontal shortening / minimum horizontal extension) in every considered zone (Fig. 13 a) leads to a well-defined image of the progressive rotations of S_{Hmax} in Iberia. Composed Right Dihedra plots qualitatively show similar results (Fig. 13 b).

The stress inversion solutions (Figs. 13 c, 13 d and 14) indicate that the clearest thrust faulting stress regimes occur at the edges of the study area (Gorringe and Eastern Atlas) with a vertical σ3 and an R around 0.4. In between, and throughout southern Iberia, strike-slip faulting stress regimes with a thrusting component (transpression) predominate (vertical σ2 and 0.5< R > 0), as well as in the SW (Western Spanish-Portuguese Central System and Algarve). The exception to this rule is the Granada Basin, where almost radial normal faulting stress regime occurs. These stresses influence the closest earthquakes to the E and W (Western Alcaraz and Antequera), where strike-slip faulting stress regimes with a normal component (transtension) (vertical

$\sigma2$ and $1< R > 0.5$) are active (Fig. 14). This type of stresses is also found in Al Hoceima and the offshore Atlantic. The remaining inversions (N and NE) yield normal faulting stress regimes (vertical $\sigma1$ and R close to 0.5). The $\sigma1$ trend along the plate limit (yellow in Fig. 14) remains very consistently close to N154ºE. Some more variability occurs in the Betics (blue in Fig. 14). However, the mean value of $\sigma1$ is also close to N155ºE, except in the Granada Basin, Antequera and the deep population of the Western Betics, which approaches N114°E, likely influenced by the remanent effect of the Alboran Slab. In the Central Ranges and offshore Atlantic (red in Fig. 14), the $\sigma1$ trend rotates slightly anticlockwise to N140°E, in agreement with the Eulerian pole of plate motion between Africa and Eurasia. In the Pyrenees, the clusters E and W of the main topographical relief show $\sigma1$ orientations close to N154°E, as in most Iberian populations. Nevertheless, the central part (CO and WP) has a σ_3 perpendicular to the range, so that local stresses (post-orogenic collapse or isostatic reset) predominate over the regional ones. The Central Basins is clearly out of this global arrangement. The solution in the Eastern Pyrenees is very similar to those of the Valencia Through and the Iberian Chain (EPCE, WVT, SVT and IC), defining a cluster of solutions for the E of the Iberian Peninsula (Fig. 14). It should be noted that, in these solutions, σ_2 is oriented in the NW-SE direction and not in NE-SW so that the present-day normal faulting stress regime is likely to be more affected by the convergence between Africa and Eurasia than by the back-arc extension of the easternmost subduction zones.

The presence of thrusting focal mechanisms in front of the Alboran Domain supports the idea that its emplacement has been mechanically decoupling of Iberia from Africa, from east to west. Similarly, the SPCS has been losing its thrust faulting stress regime from E to W, deactivating the thrusts N of Madrid since the Late Miocene, while in its Portuguese sector, it is still an active intraplate orogen. Therefore, in central Iberia, from E to W, the state of stress changes from a clearly normal faulting stress regime in the IC (R=0.43 with σ_1 in the vertical), with normal faulting also in the middle (CB), to a thrust-faulting stress regime in the WCS, and a strike-slip faulting stress regime in the offshore (OA), progressively passing σ_2 or σ_1 from N148°E to N131°E (except in CB), according to the position of the Eulerian pole. Thus, in the offshore continuation of the SPCS, the expected tectonic environment would be transtensive.

Fig. 15 summarizes the stress inversion results. Where normal faulting stress regimes are inferred (blue arrows in Fig. 15), Cenozoic thrusts are not active (North, Central and Northeast Iberia), however, normal faulting stress regimes are active in areas that display previous compressional features, as in the IC. Transtensional areas (green arrows in Fig. 15) are also likely deactivating thrusts in the Estremadura Spur (OC) and the closest zones to the Granada Basin (WAA and BA), where an active normal faulting stress regime is present. Mapped thrusts are predominant in the Gorringe Bank and eastern Algeria (red arrows in Fig. 15). In the remaining areas, including easternmost and westernmost Betics, and southwestern Iberia, transpression is the prevailing tectonic regime. Therefore, mapped thrusts and strike-slip faults must be considered active structures.

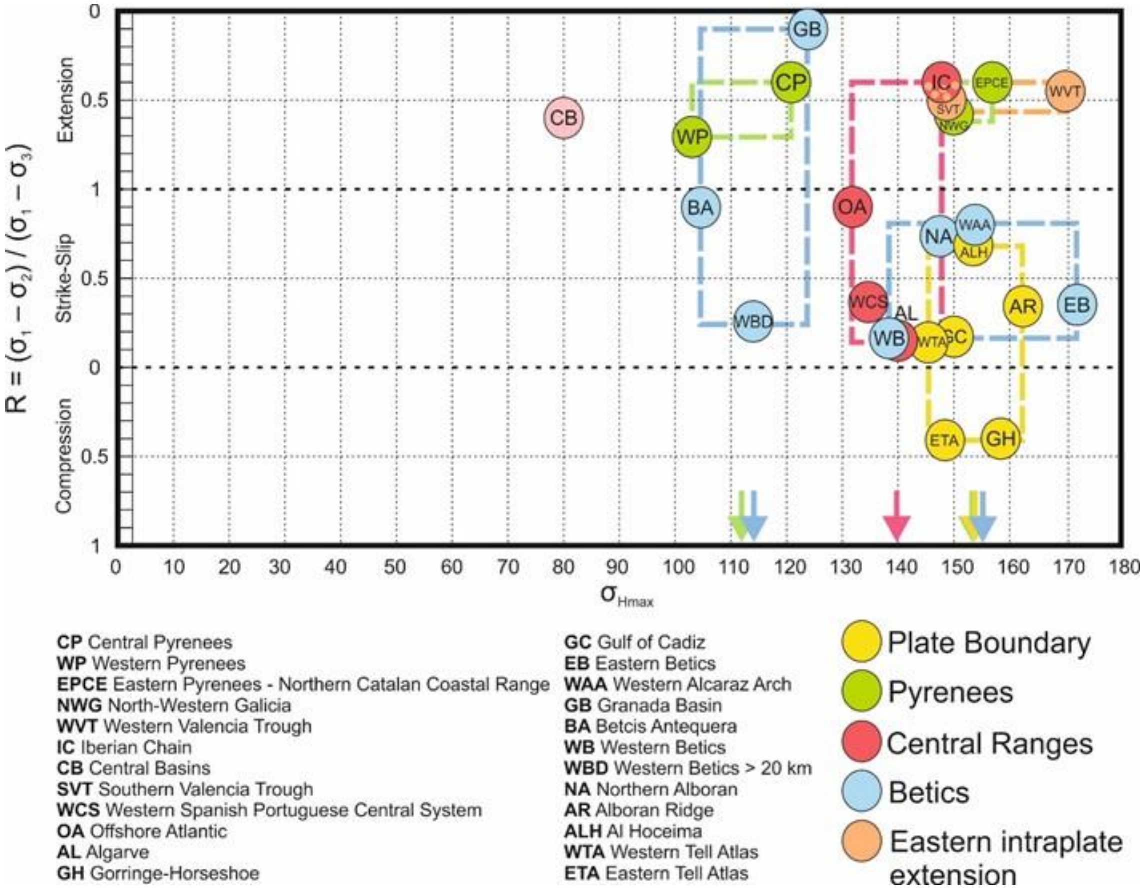

Figure 14: R (Stress tensor ratio) Vs σ_{Hmax} trend (σ_1 for thrusts and strike-slip faults stress regimes, σ_2 normal faulting stress regimes). The N-S direction is marked by 0° and 180°, while the E-W direction coincides with the value of 90. The areas considered have been grouped into those at the plate boundary (yellow, AR, GH, ETA, GC, WTA, and ALH), those in the Pyrenees (green, EPCE, NWG, CP, and WP), those in the Central Ranges (in red, OA, WCS, AL and IC), those in the Betics (in blue, separated BA, GB, WBD from the strike-strike solutions BA, GB, WBD), those related to the intraplate extension in E Iberia (Mediterranean) (in orange, WVT, SVT and IC. The latter is also included in the Central Ranges solution). CB (in pink) does not seem to be related to any of the previous groupings. The dashed rectangles mark each group's maximum and minimum values of R and σ_{Hmax}, with their corresponding colour. The lower arrows indicate the average values of σ_{Hmax} for each group.

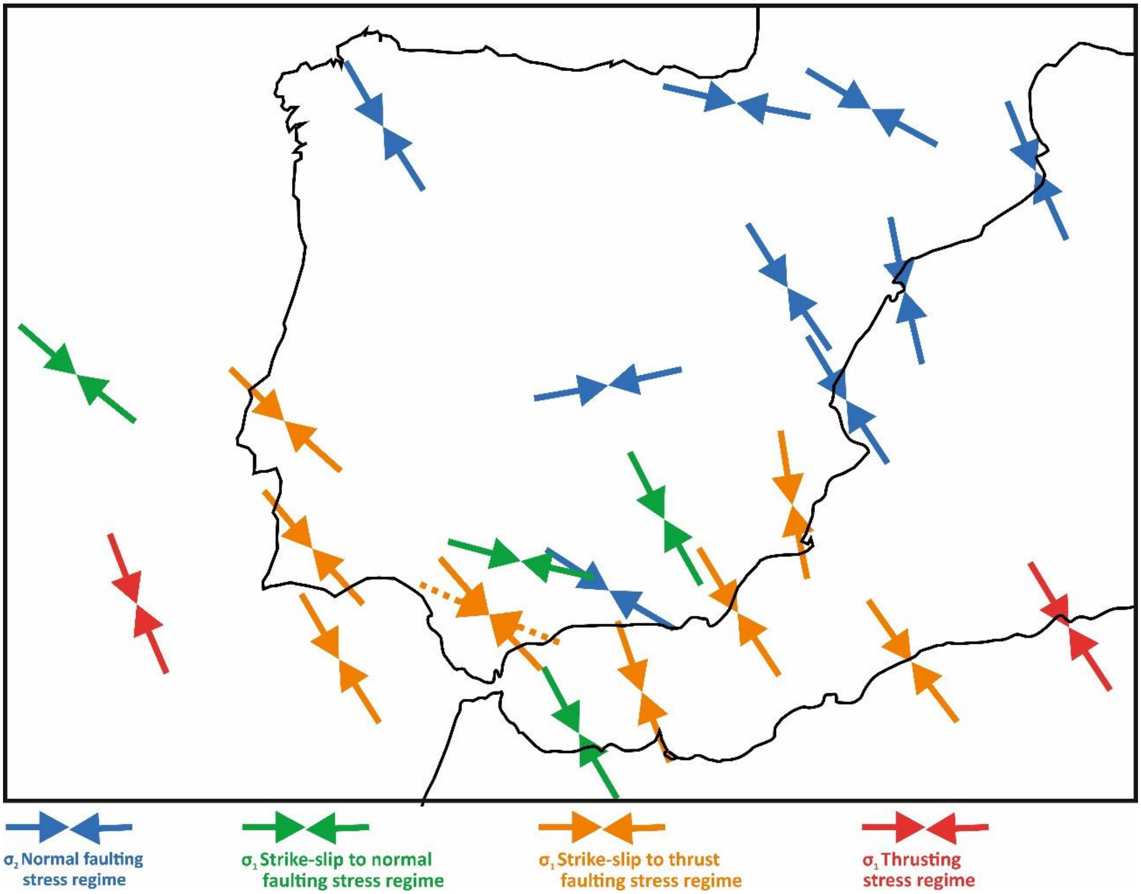

Figure 15: Summarized state of stress of Iberia based on focal mechanism stress inversion from this study.

7 Conclusions

In general, the shape of the combined seismic moment tensors at the plate boundary is oblate ($k < 1$), showing a predominance of transpressive tensors. As we move away from the plate boundary, the tensors become prolate in shape ($k > 1$), characterizing the extensional contexts of the Pyrenees, the Valencia Trough, and the Central Basins. An exception to this rule is the combined tensor of the Granada Basin, which yielded a pure normal faulting tensor close to the plate boundary.

Similar tendencies are observed from the rescaled shape factor (k´). Northern Algeria and southwestern Portugal represent the areas of maximum compression, related to the plate boundary, while the Pyrenees and the Iberian Chain are characterized by extension. Individual calculations obtained from the Slip Model allow to distinguish local variations. The proposed methodology optimizes the selection of populations selection for kinematic and dynamic analyses.

Although most of the defined tectonic zones exhibit focal mechanisms of different faulting types, the minimum rotation angle between their combined mechanisms indicates that they are compatible with each other, considering the permutation of their axes, in a context of distributed deformation.

The obtained orientations of the shortening and extension axes in the combined deformation tensors are similiar to those of the maximum and minimum principal stress axes obtained from the stress inversion. However, the results may differ significantly for some populations.

Outside of the Iberian Peninsula, our stress inversions yielded thrust faulting stress regimes in the Gorringe and Eastern Atlas zones, with a vertical σ3 and R around 0.4. In southern Iberia, transpression predominates, characterized bystrike-slip faulting stress regimes with a thrusting component, where vertical vertical σ2 and 0.5> R > 0. This type of stresses is also found in the southwestern corner of the Iberian Peninsula, specifically in the Western Spanish-Portuguese Central System and Algarve. Transtensional (strike-slip faulting stress regimes with a normal faulting component, vertical σ2 and 1> R > 0,5) surround the normal faulting stress regime inferred for the Granada Basin (Western Alcaraz and Antequera), and are also present in northern Morocco (Al Hoceima) and offshore Atlantic. Towards the Betics foreland and to the east of the westernmost sector of the Spanish-Portuguese Central System, including the Pyrenees, a normal faulting stress regime predominates. Within these zones, a slightly more strike-slip component is observed west of the Central Pyrenees, in Western Pyrenees and North-Western Galicia. Regardless, R values in these zones are close to 0.5, except in the Granada Basin inversion, where an almost radial normal faulting stress regime is found.

The σ_{Hmax} mean values range from N105°E to N155°E (except for the Central Basins solution). The σ_{Hmax} orientation from this study, based on individual focal mechanisms and the stress inversion, is in good overall agreement with data records from other stress indicators, particularly from the numerous borehole logging data previously published as part of the World Stress Map (Heidbach et al., 2018). Only in the center of Iberia this is not true, either due to the low data density resulting in large rotations of σ_{Hmax} from the regional trend, or to horizontal stress magnitudes being close to each other, allowing for local stress variability due to stiffness and density contrasts.

The ESE-WNW closest stress inversion results that can be considered anomalous at a regional scale are related to the Granada Basin and the Pyrenees, where local stresses arise. Out of this, the Central Ranges (IC, WCS, OA and AL) have a common σ_{Hmax} trend around N140°E. Although the Betics solutions (far from the Granada Basin) exhibit some variability, they follow an N155°E mean σ_{Hmax} trend, like the ones found in the NW and NE corners of Iberia (EPCS and NWG). Solutions along the plate limit also concur with this σ_{Hmax} trend; N155°E can then be considered the likely result of Africa approaching Iberia. The 15º anticlockwise rotation to the north must be related to the location of the Eulerian pole between both plates. This general tectonic context seems to be overprinting the back-arc subduction-related extension in the east of Iberia and the Alboran Sea.

Appendix A

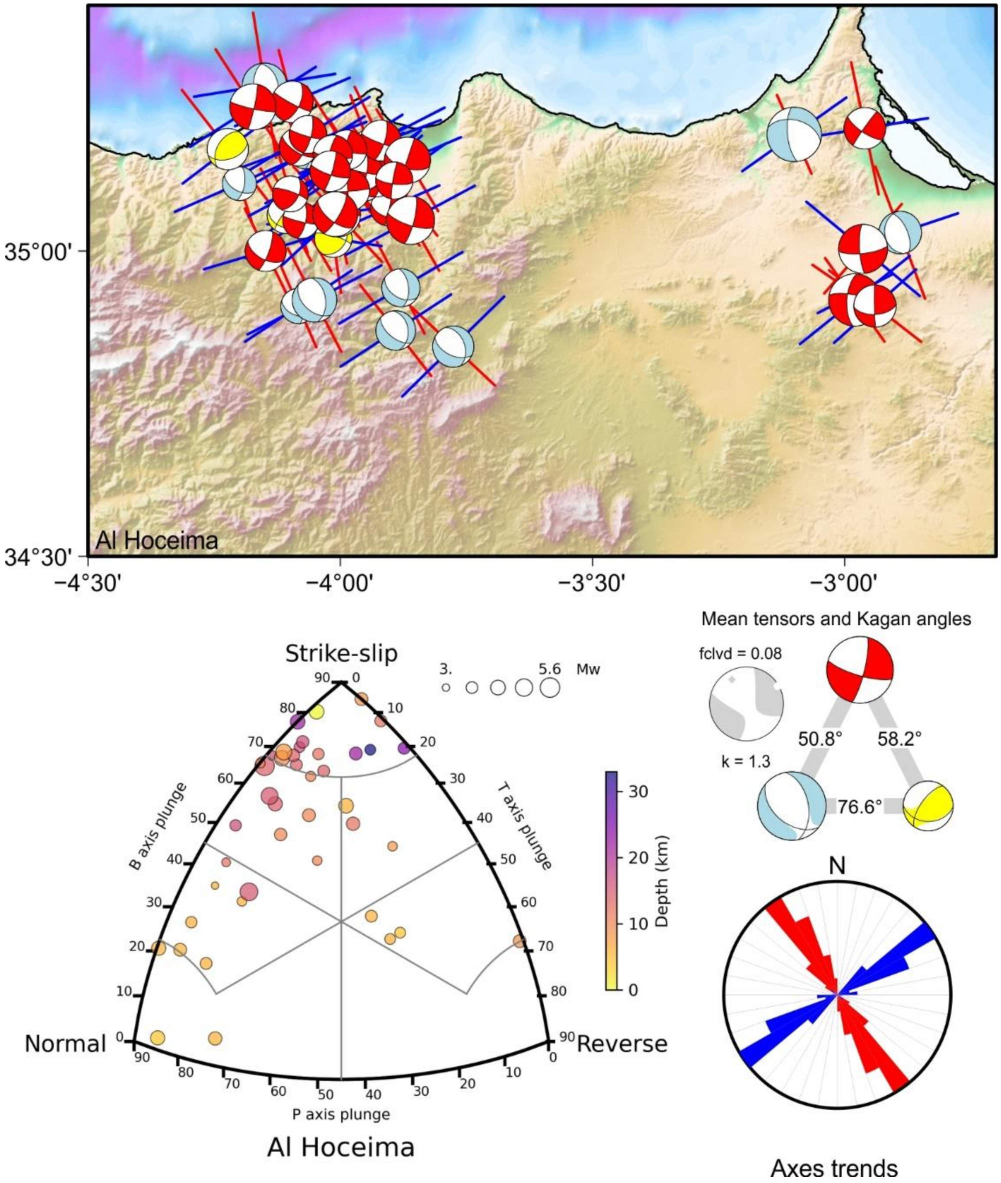

Fig. A1: Al Hoceima tectonic zone. Top map: focal mechanisms with maximum horizontal axis (P or B for normal ruptures) and minimum horizontal axis (T or B for reverse ruptures) orientation. Bottom left classification diagram for earthquake rupture types. Middle right: Average tensors (complete in gray) and Kagan angles between the average tensors for each rupture type. Bottom right: Rose diagram of maximum and minimum horizontal axes orientation.

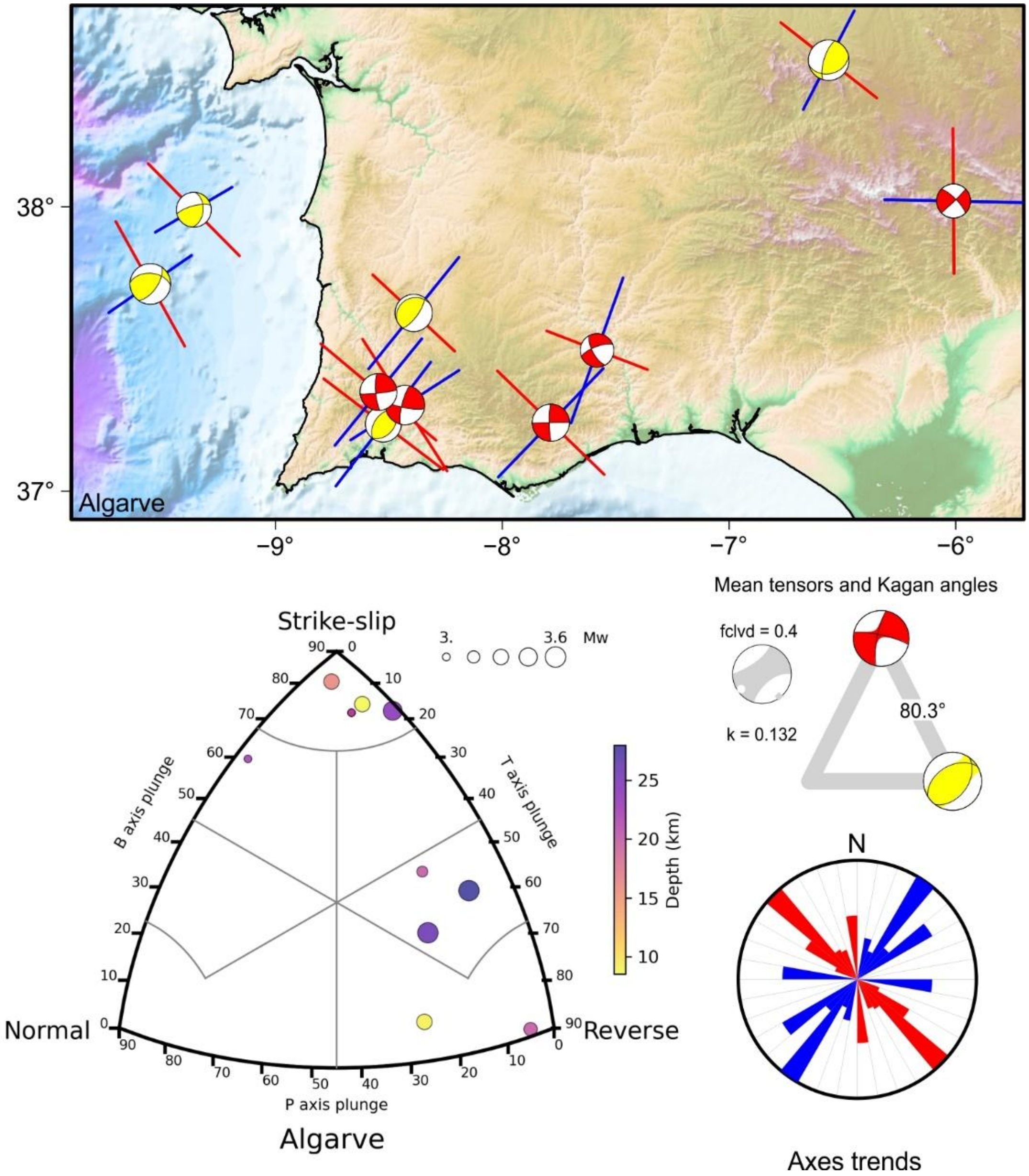

Fig. A2: Algarve tectonic zone. Top map: focal mechanisms with maximum horizontal axis (P or B for normal ruptures) and minimum horizontal axis (T or B for reverse ruptures) orientation. Bottom left classification diagram for earthquake rupture types. Middle right: Average tensors (complete in gray) and Kagan angles between the average tensors for each rupture type. Bottom right: Rose diagram of maximum and minimum horizontal axes orientation.

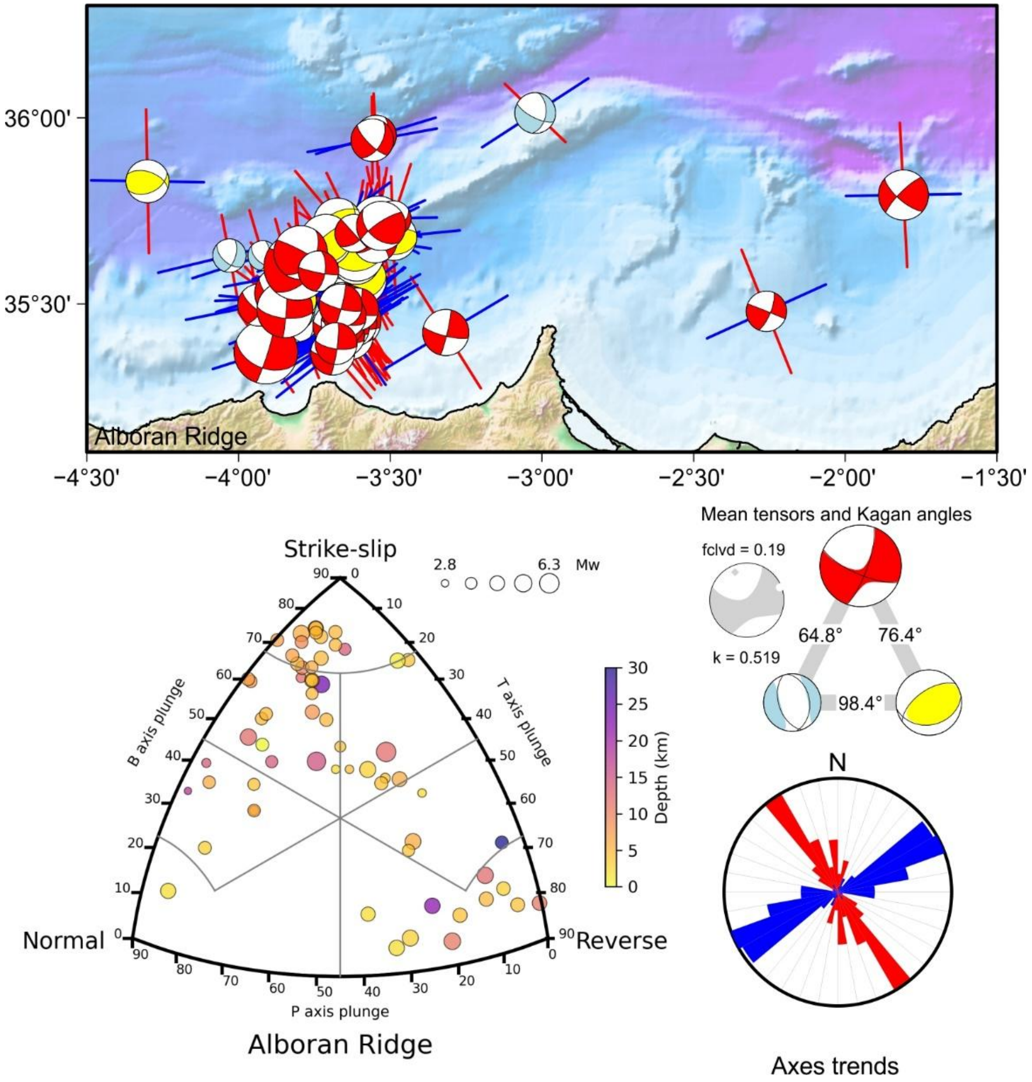

Fig. A3: Alboran Ridge tectonic zone. Top map: focal mechanisms with maximum horizontal axis (P or B for normal ruptures) and minimum horizontal axis (T or B for reverse ruptures) orientation. Bottom left classification diagram for earthquake rupture types. Middle right: Average tensors (complete in gray) and Kagan angles between the average tensors for each rupture type. Bottom right: Rose diagram of maximum and minimum horizontal axes orientation.

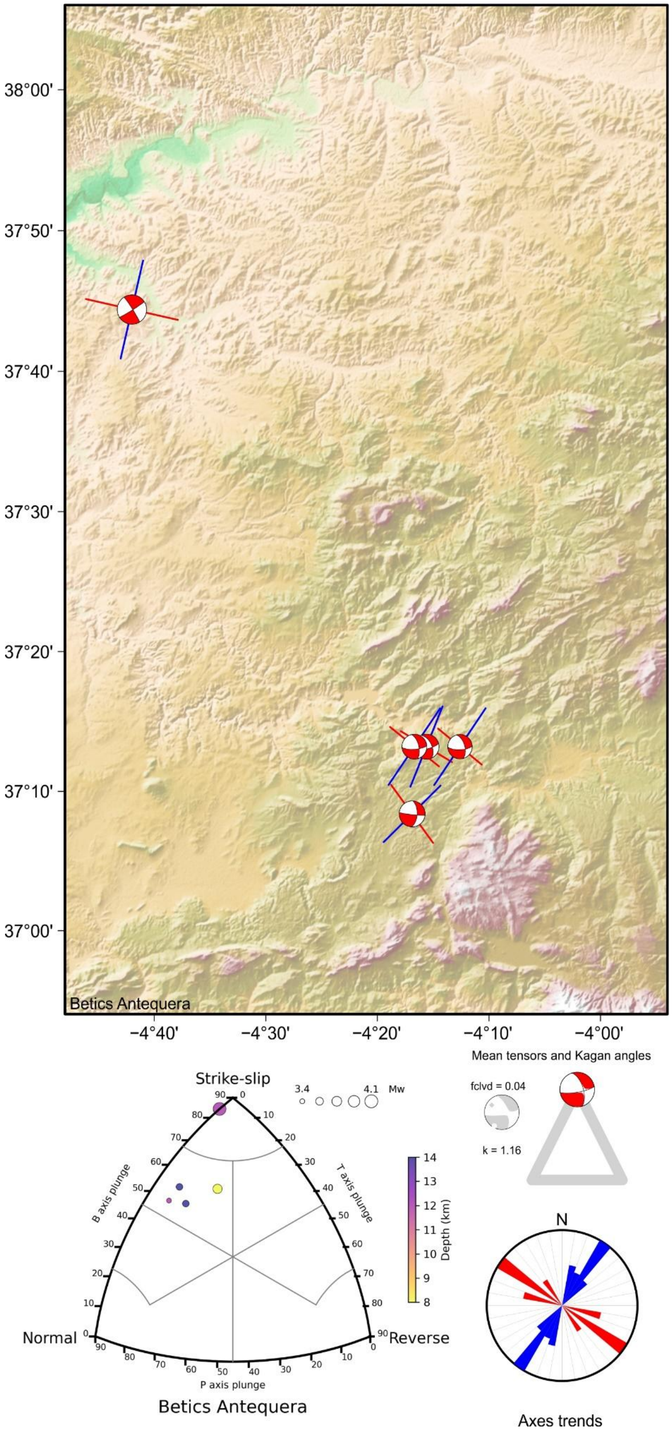

Fig. A4: Betics Antequera tectonic zone. Top map: focal mechanisms with maximum horizontal axis (P or B for normal ruptures) and minimum horizontal axis (T or B for reverse ruptures) orientation. Bottom left classification diagram for earthquake rupture types. Middle right: Average tensors (complete in gray) and Kagan angles between the average tensors for each rupture type. Bottom right: Rose diagram of maximum and minimum horizontal axes orientation.

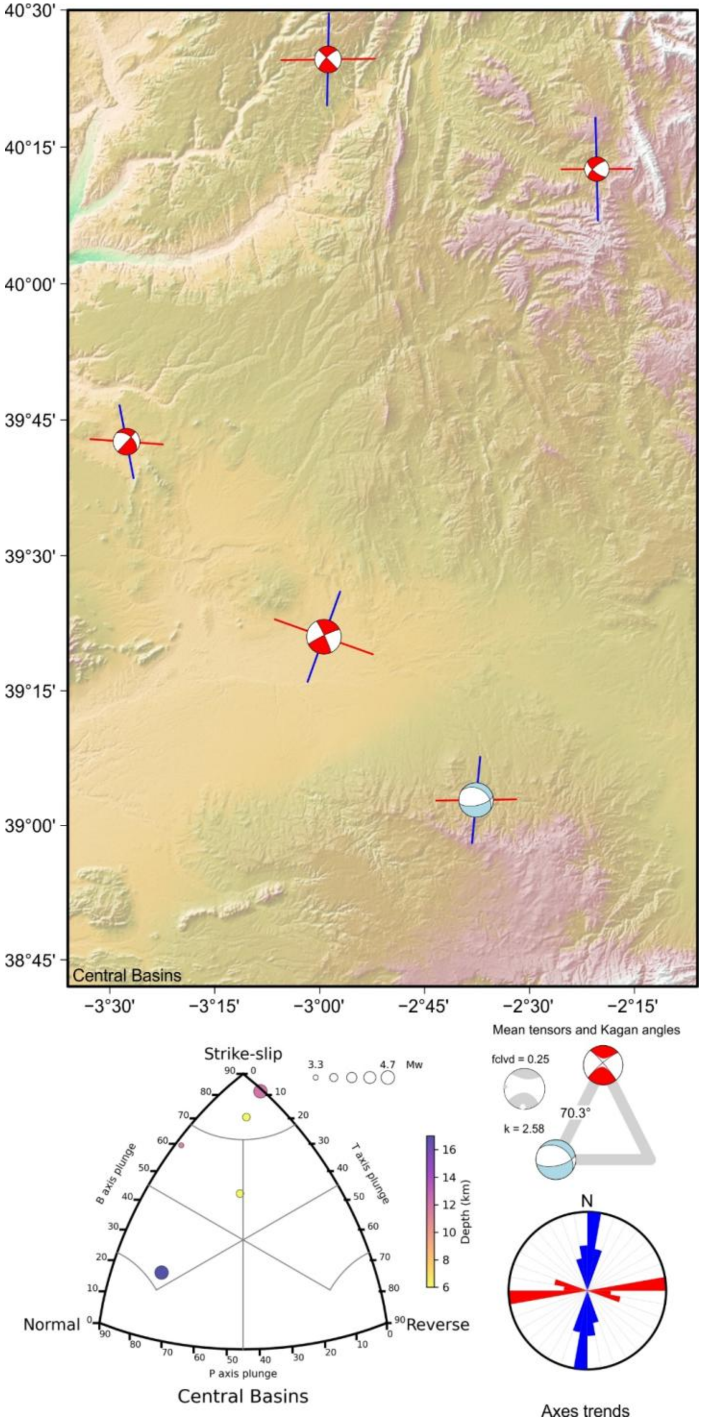

Fig. A5: Central Basins tectonic zone. Top map: focal mechanisms with maximum horizontal axis (P or B for normal ruptures) and minimum horizontal axis (T or B for reverse ruptures) orientation. Bottom left classification diagram for earthquake rupture types. Middle right: Average tensors (complete in gray) and Kagan angles between the average tensors for each rupture type. Bottom right: Rose diagram of maximum and minimum horizontal axes orientation.

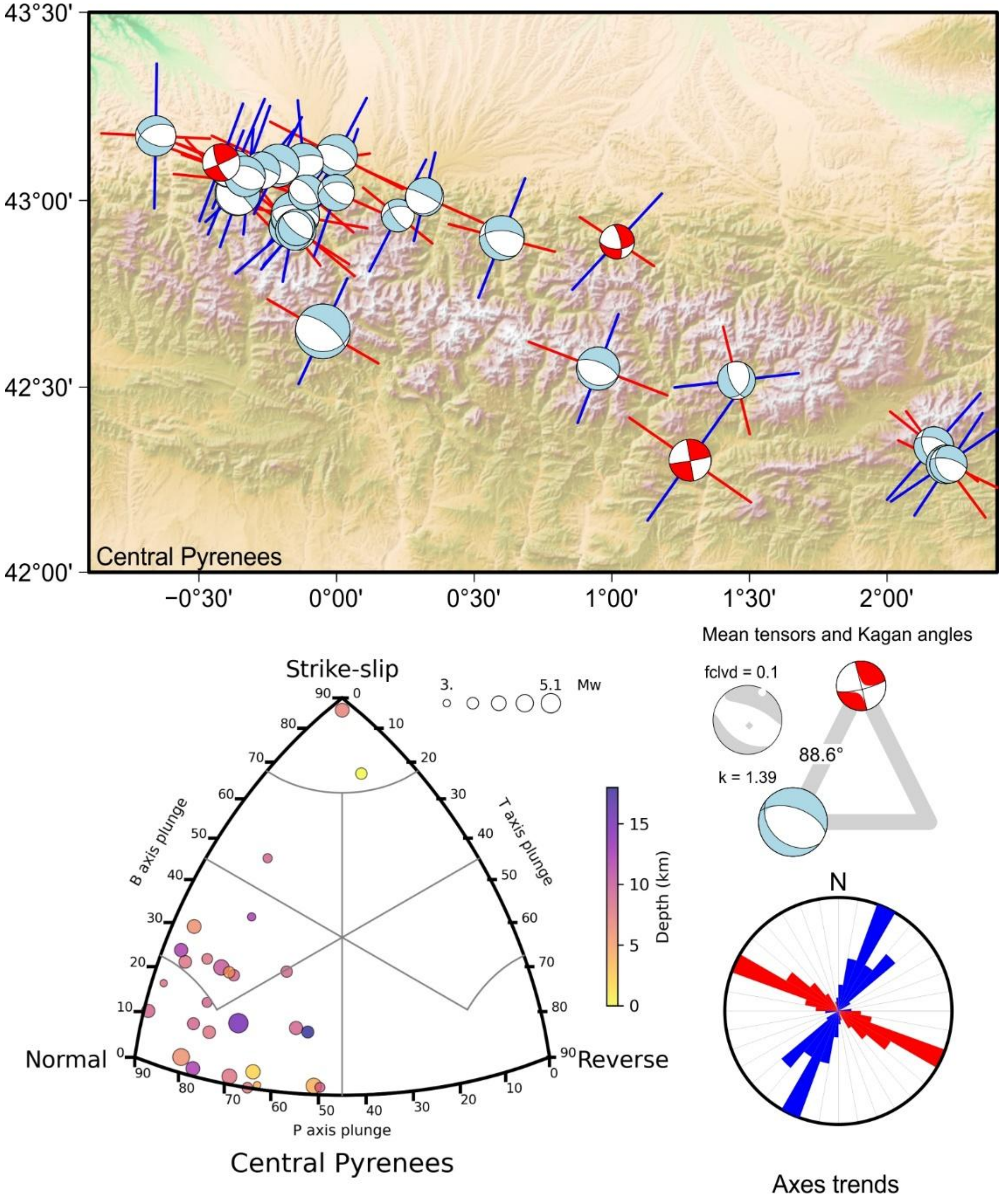

Fig. A6: Central Pyrenees tectonic zone. Top map: focal mechanisms with maximum horizontal axis (P or B for normal ruptures) and minimum horizontal axis (T or B for reverse ruptures) orientation. Bottom left classification diagram for earthquake rupture types. Middle right: Average tensors (complete in gray) and Kagan angles between the average tensors for each rupture type. Bottom right: Rose diagram of maximum and minimum horizontal axes orientation.

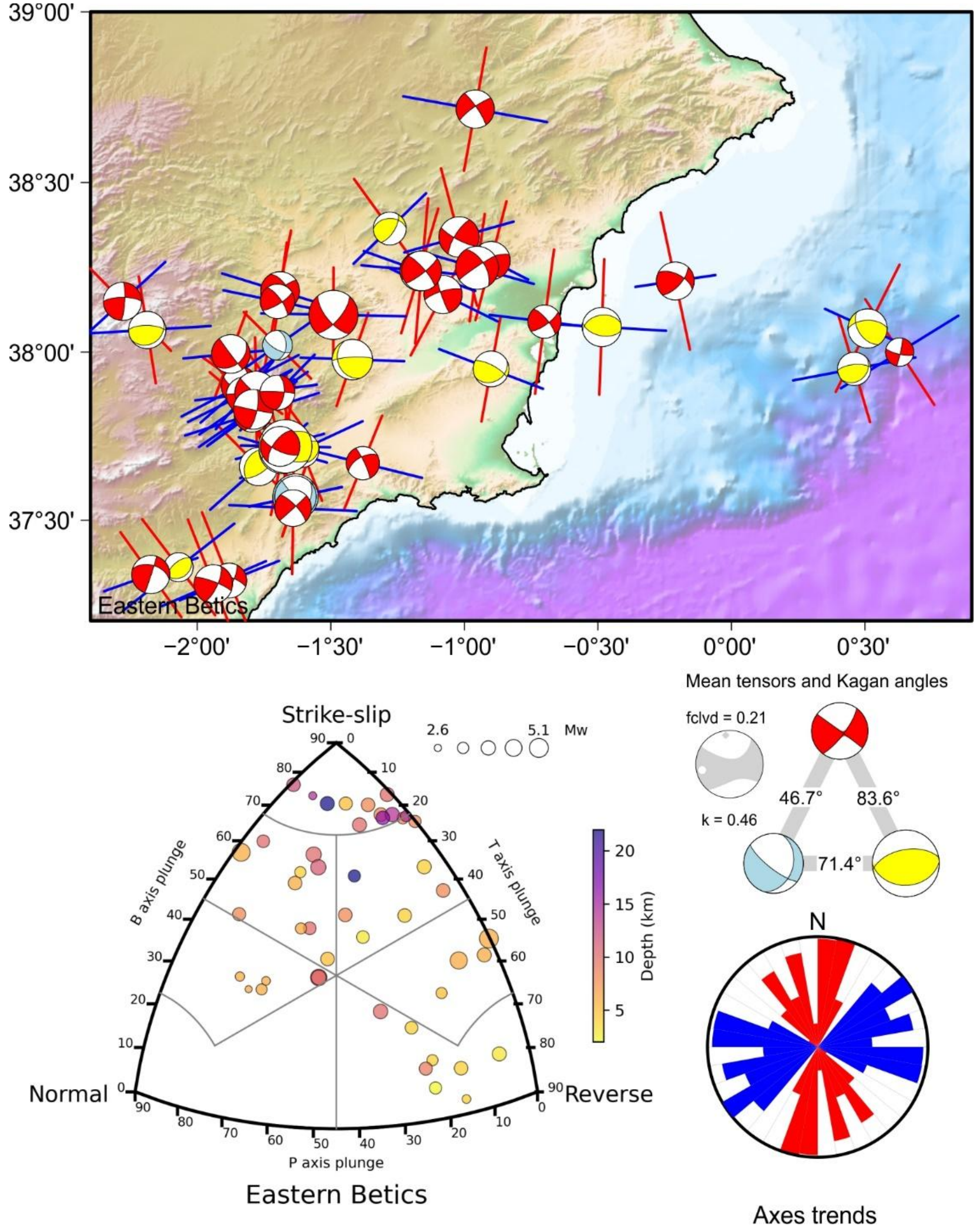

Fig. A7: Eastern Betics tectonic zone. Top map: focal mechanisms with maximum horizontal axis (P or B for normal ruptures) and minimum horizontal axis (T or B for reverse ruptures) orientation. Bottom left classification diagram for earthquake rupture types. Middle right: Average tensors (complete in gray) and Kagan angles between the average tensors for each rupture type. Bottom right: Rose diagram of maximum and minimum horizontal axes orientation.

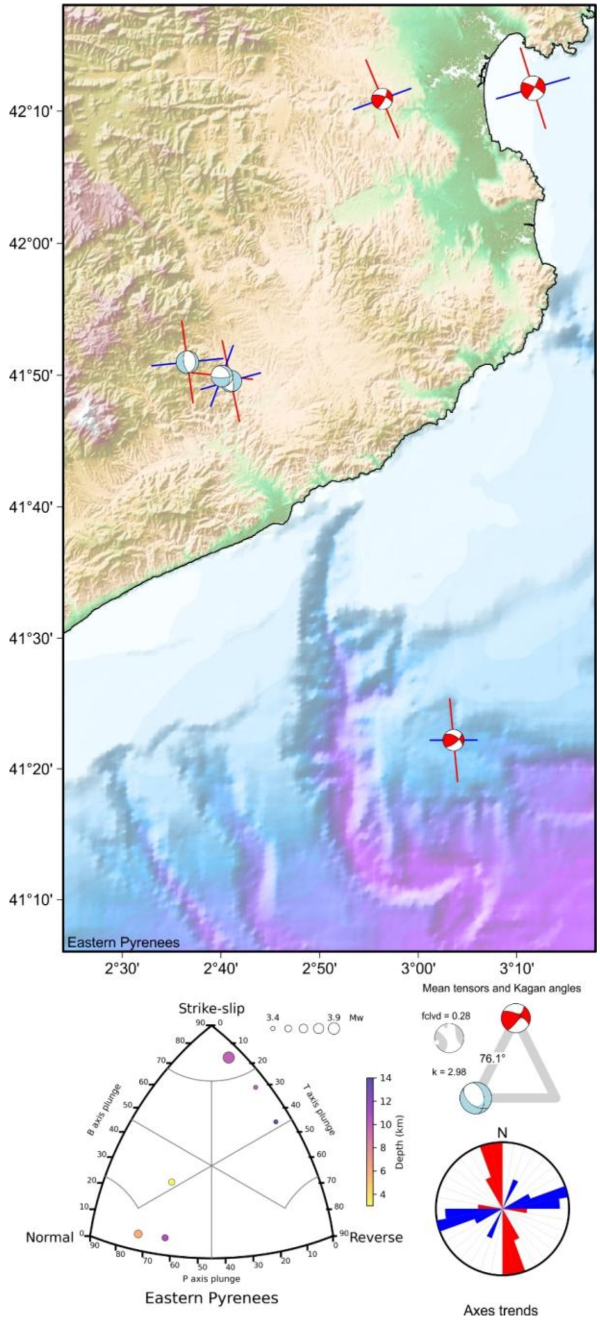

Fig. A8: Eastern Pyrenees tectonic zone. Top map: focal mechanisms with maximum horizontal axis (P or B for normal ruptures) and minimum horizontal axis (T or B for reverse ruptures) orientation. Bottom left classification diagram for earthquake rupture types. Middle right: Average tensors (complete in gray) and Kagan angles between the average tensors for each rupture type. Bottom right: Rose diagram of maximum and minimum horizontal axes orientation.

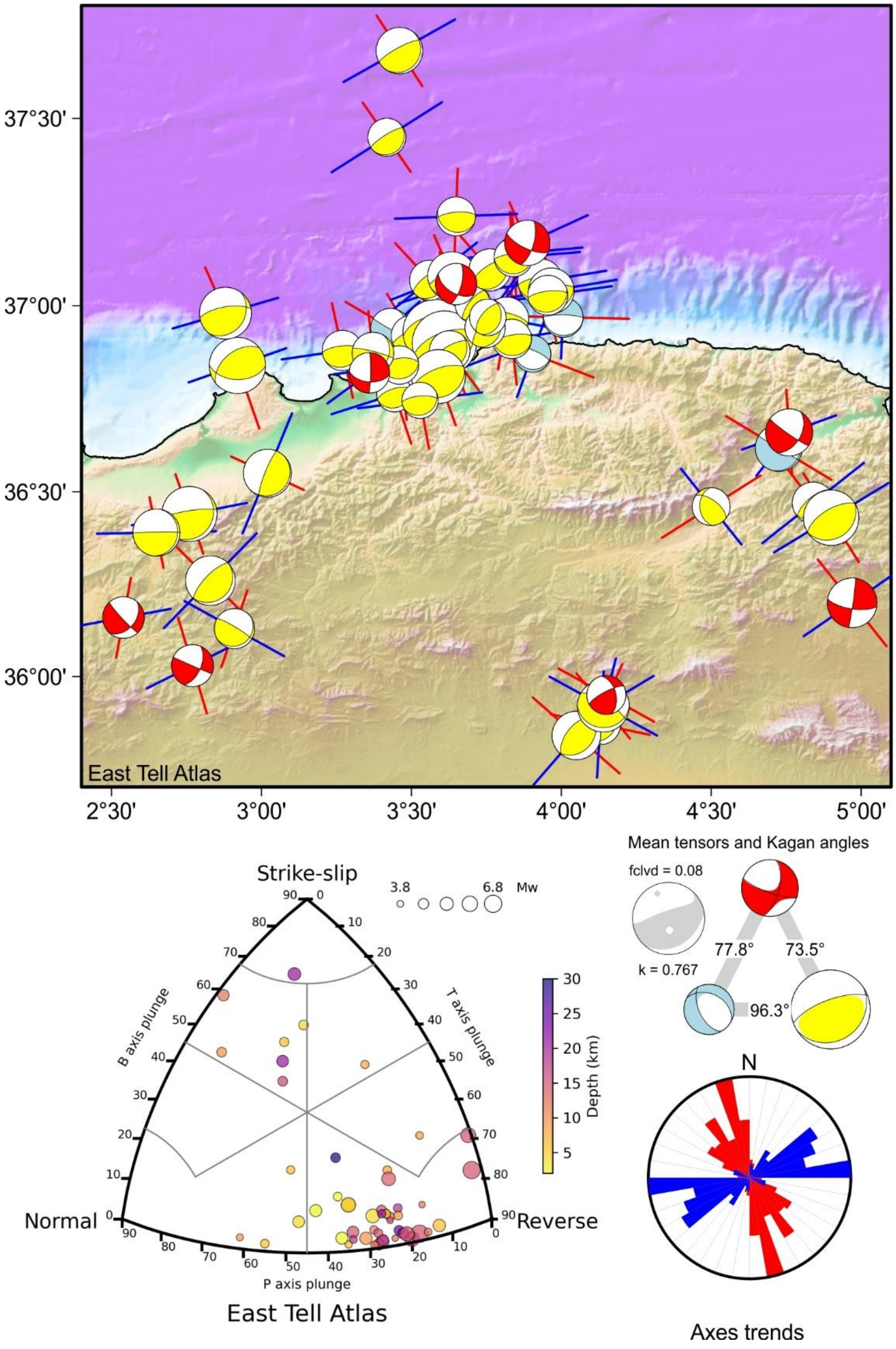

Fig. A9: East Tell Atlas tectonic zone. Top map: focal mechanisms with maximum horizontal axis (P or B for normal ruptures) and minimum horizontal axis (T or B for reverse ruptures) orientation. Bottom left classification diagram for earthquake rupture types. Middle right: Average tensors (complete in gray) and Kagan angles between the average tensors for each rupture type. Bottom right: Rose diagram of maximum and minimum horizontal axes orientation.

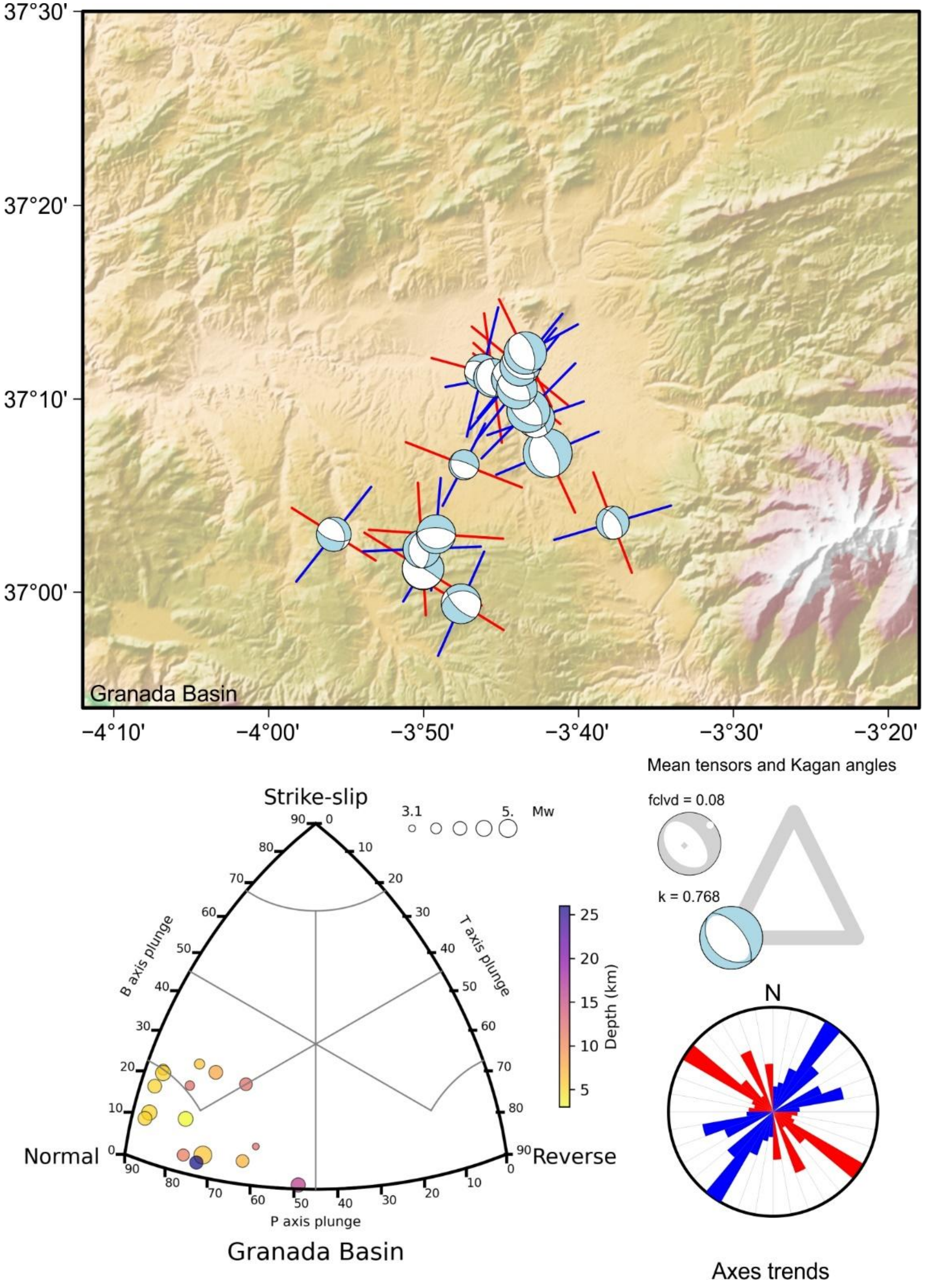

Fig. A10: Granada Basin tectonic zone. Top map: focal mechanisms with maximum horizontal axis (P or B for normal ruptures) and minimum horizontal axis (T or B for reverse ruptures) orientation. Bottom left classification diagram for earthquake rupture types. Middle right: Average tensors (complete in gray) and Kagan angles between the average tensors for each rupture type. Bottom right: Rose diagram of maximum and minimum horizontal axes orientation.

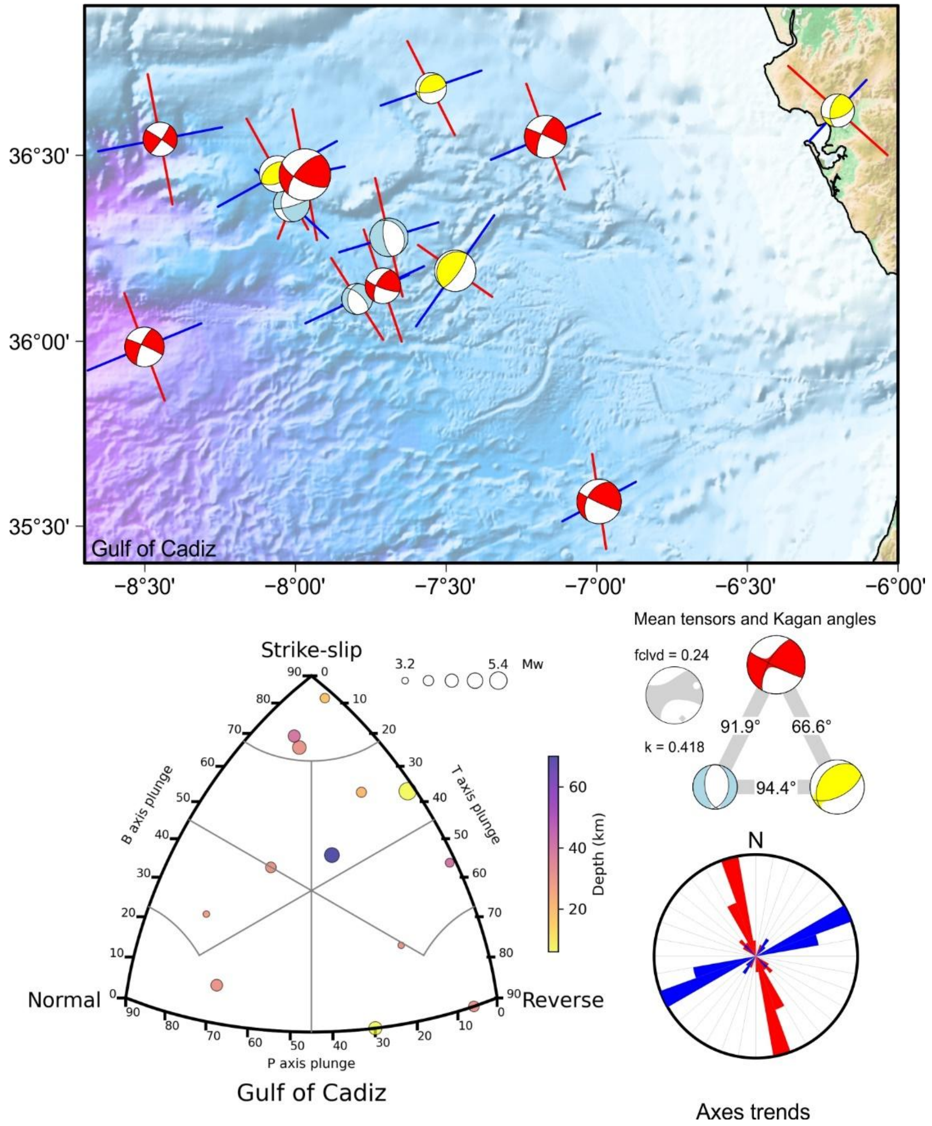

Fig. A11: Gulf of Cádiz tectonic zone. Top map: focal mechanisms with maximum horizontal axis (P or B for normal ruptures) and minimum horizontal axis (T or B for reverse ruptures) orientation. Bottom left classification diagram for earthquake rupture types. Middle right: Average tensors (complete in gray) and Kagan angles between the average tensors for each rupture type. Bottom right: Rose diagram of maximum and minimum horizontal axes orientation.

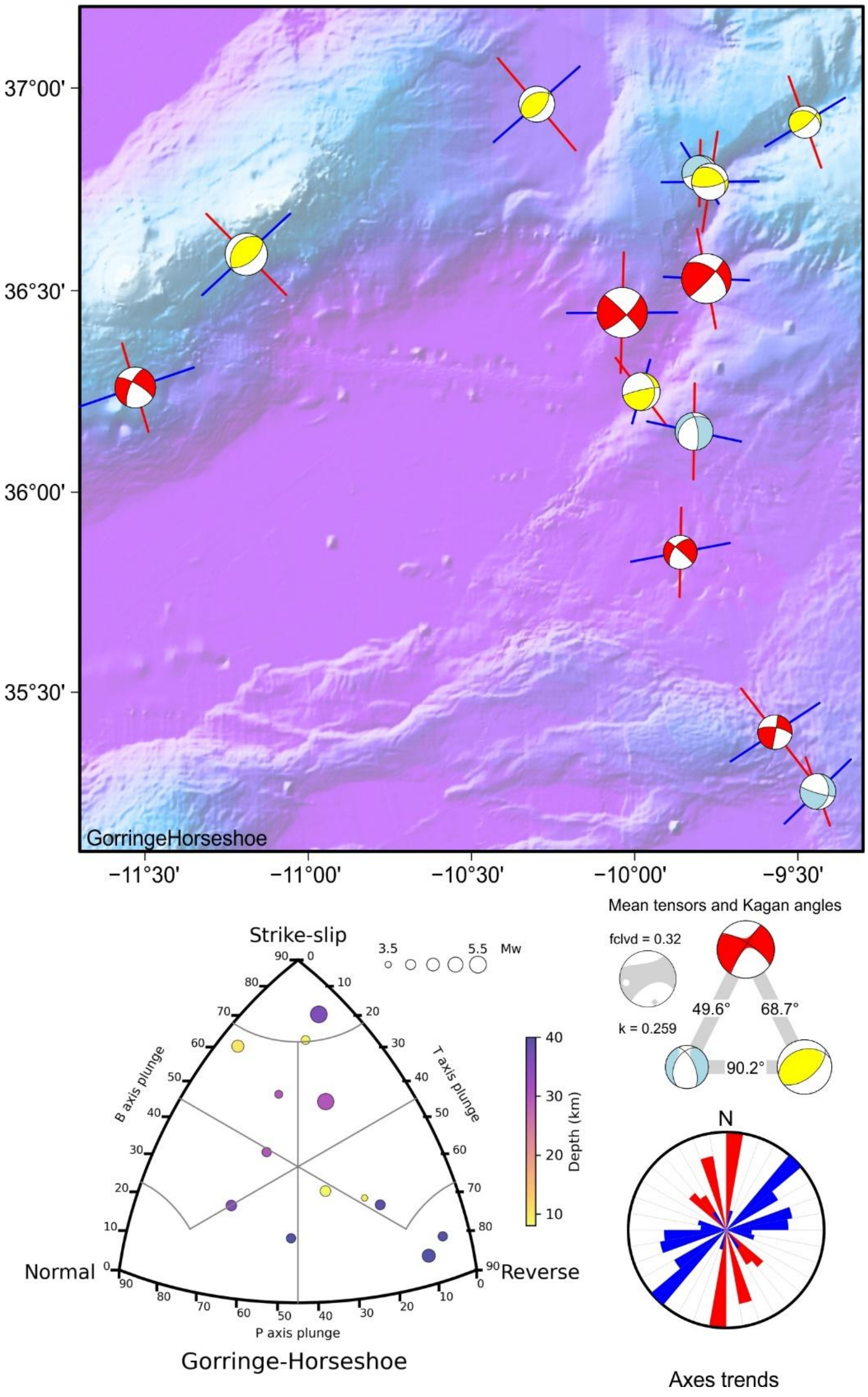

Fig. A12: Gorringe-Horseshoe tectonic zone. Top map: focal mechanisms with maximum horizontal axis (P or B for normal ruptures) and minimum horizontal axis (T or B for reverse ruptures) orientation. Bottom left classification diagram for earthquake rupture types. Middle right: Average tensors (complete in gray) and Kagan angles between the average tensors for each rupture type. Bottom right: Rose diagram of maximum and minimum horizontal axes orientation.

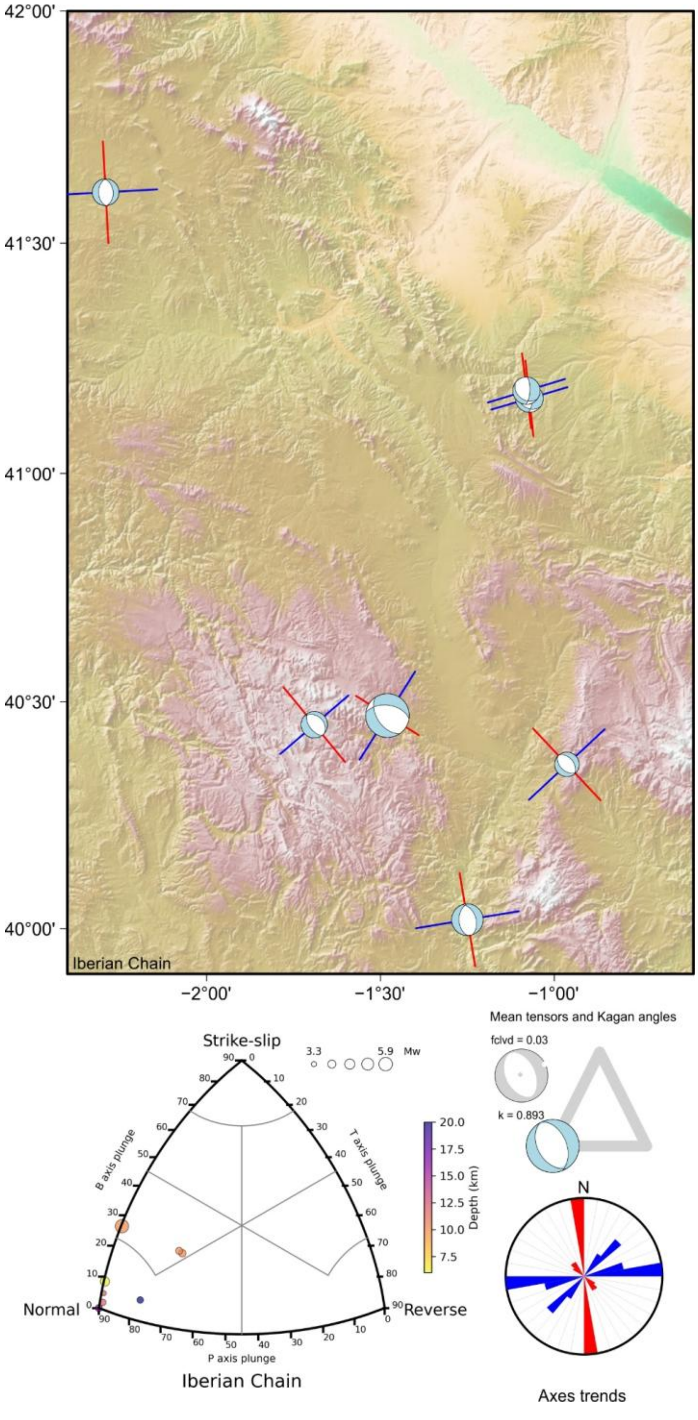

Fig. A13: Iberian Chain tectonic zone. Top map: focal mechanisms with maximum horizontal axis (P or B for normal ruptures) and minimum horizontal axis (T or B for reverse ruptures) orientation. Bottom left classification diagram for earthquake rupture types. Middle right: Average tensors (complete in gray) and Kagan angles between the average tensors for each rupture type. Bottom right: Rose diagram of maximum and minimum horizontal axes orientation.

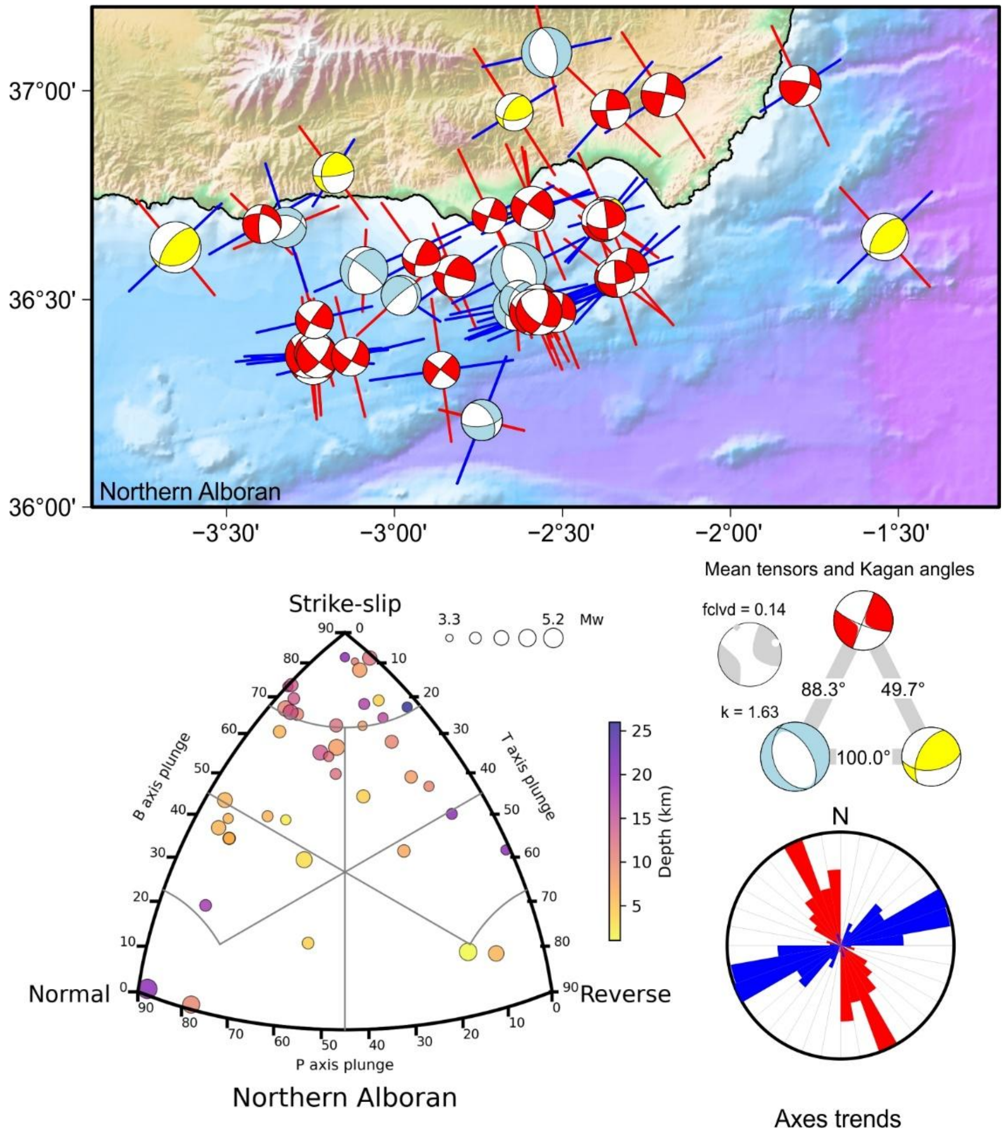

Fig. A14: Northern Alboran tectonic zone. Top map: focal mechanisms with maximum horizontal axis (P or B for normal ruptures) and minimum horizontal axis (T or B for reverse ruptures) orientation. Bottom left classification diagram for earthquake rupture types. Middle right: Average tensors (complete in gray) and Kagan angles between the average tensors for each rupture type. Bottom right: Rose diagram of maximum and minimum horizontal axes orientation.

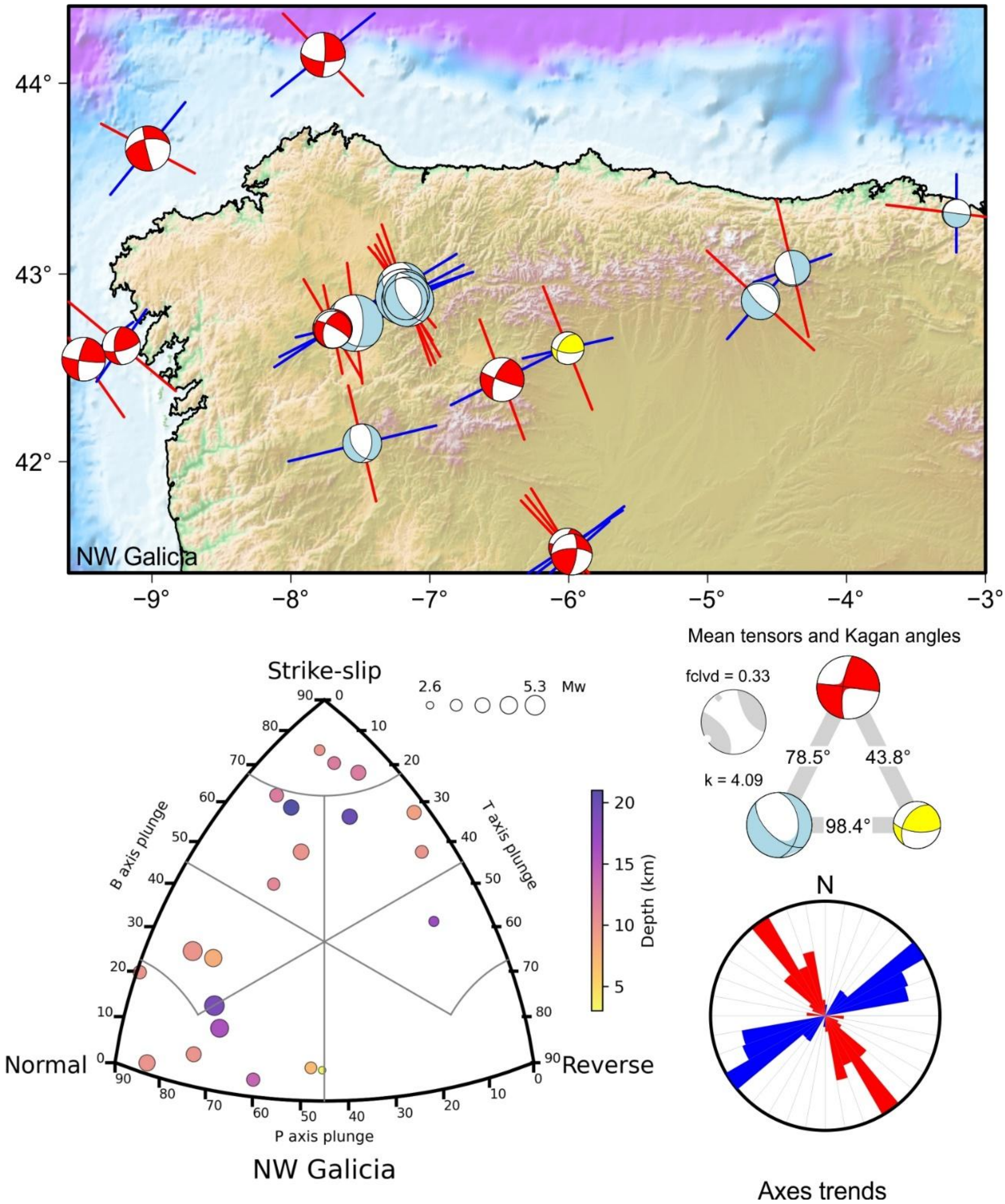

Fig. A15: NW Galicia tectonic zone. Top map: focal mechanisms with maximum horizontal axis (P or B for normal ruptures) and minimum horizontal axis (T or B for reverse ruptures) orientation. Bottom left classification diagram for earthquake rupture types. Middle right: Average tensors (complete in gray) and Kagan angles between the average tensors for each rupture type. Bottom right: Rose diagram of maximum and minimum horizontal axes orientation.

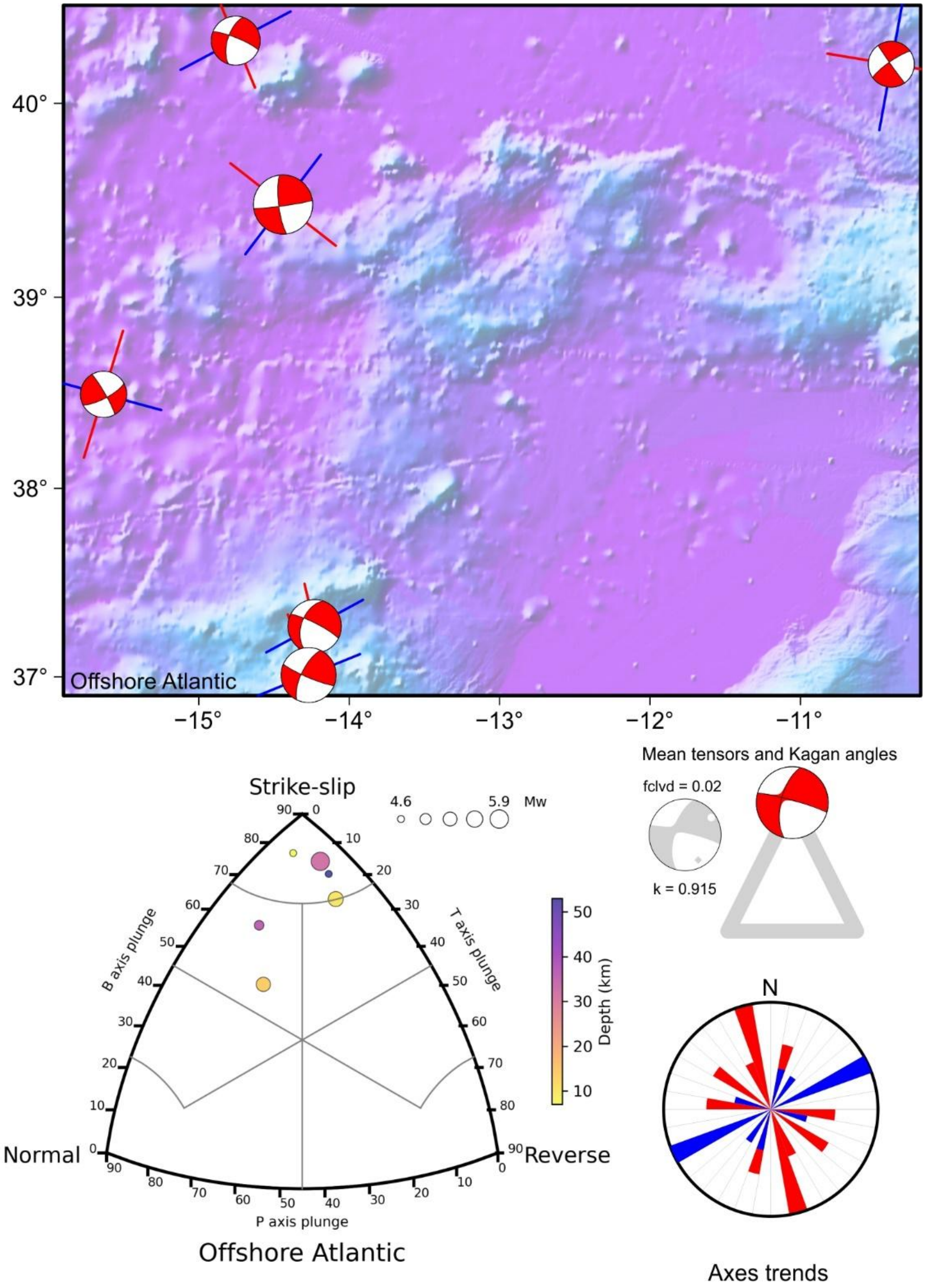

Fig. A16: Offshore Atlantic tectonic zone. Top map: focal mechanisms with maximum horizontal axis (P or B for normal ruptures) and minimum horizontal axis (T or B for reverse ruptures) orientation. Bottom left classification diagram for earthquake rupture types. Middle right: Average tensors (complete in gray) and Kagan angles between the average tensors for each rupture type. Bottom right: Rose diagram of maximum and minimum horizontal axes orientation.

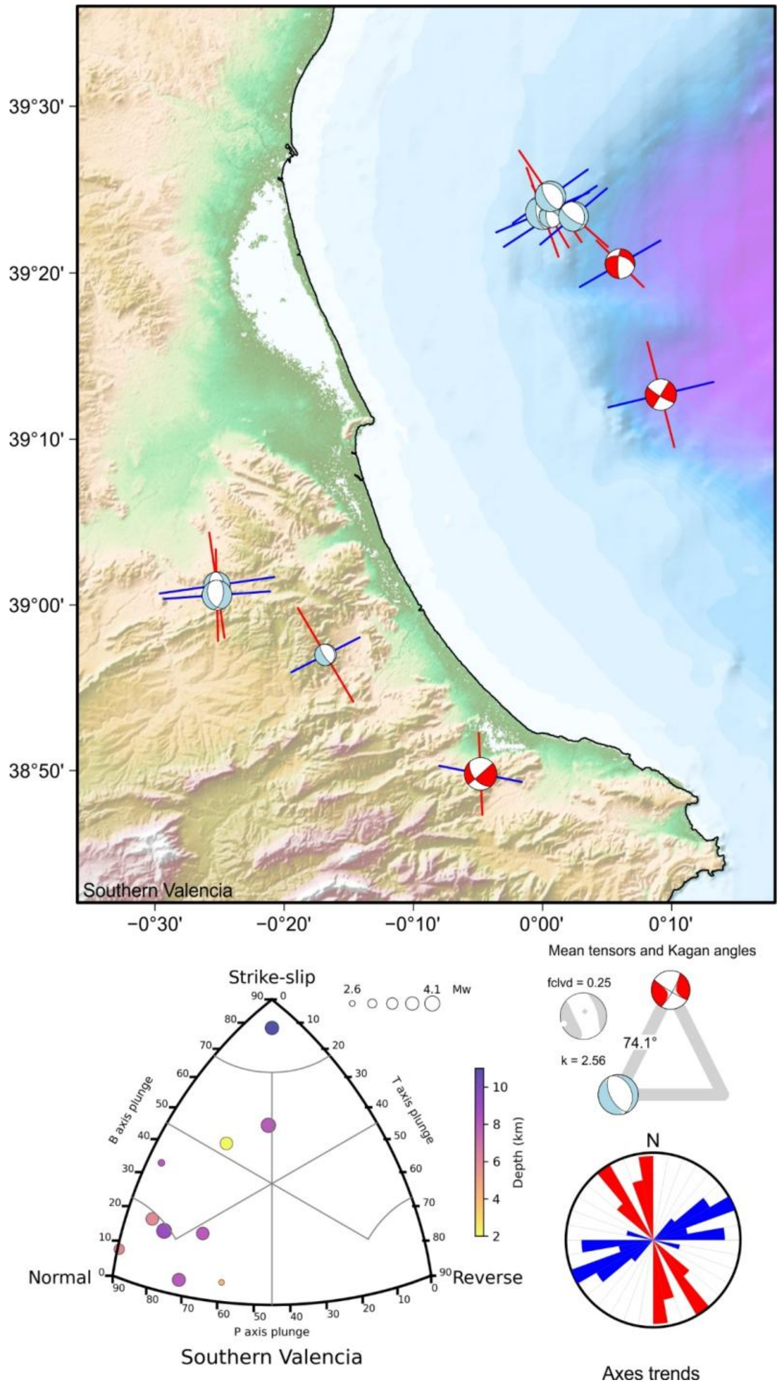

Fig. A17: Southern Valencia tectonic zone. Top map: focal mechanisms with maximum horizontal axis (P or B for normal ruptures) and minimum horizontal axis (T or B for reverse ruptures) orientation. Bottom left classification diagram for earthquake rupture types. Middle right: Average tensors (complete in gray) and Kagan angles between the average tensors for each rupture type. Bottom right: Rose diagram of maximum and minimum horizontal axes orientation.

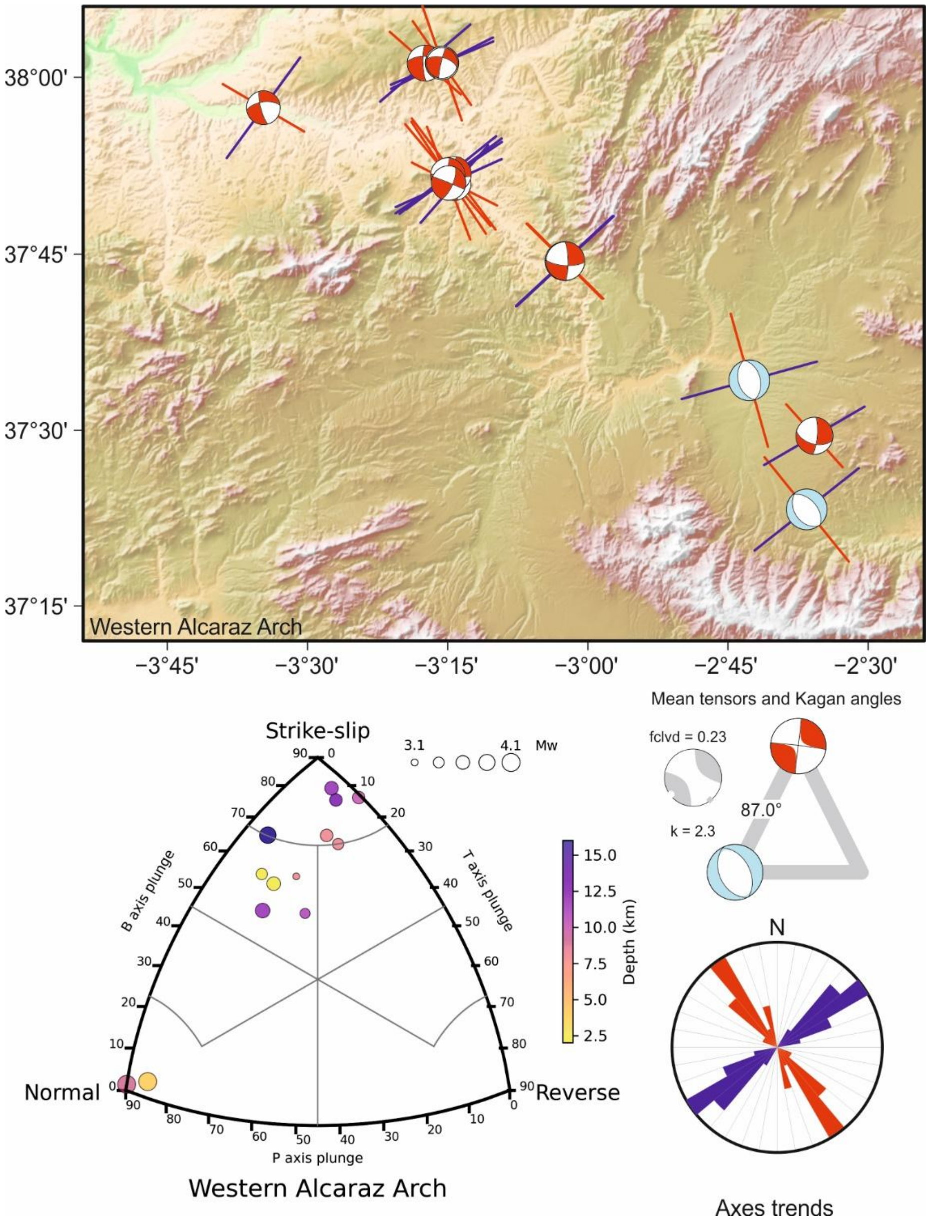

Fig. A18: Western Alcaraz Arch tectonic zone. Top map: focal mechanisms with maximum horizontal axis (P or B for normal ruptures) and minimum horizontal axis (T or B for reverse ruptures) orientation. Bottom left classification diagram for earthquake rupture types. Middle right: Average tensors (complete in gray) and Kagan angles between the average tensors for each rupture type. Bottom right: Rose diagram of maximum and minimum horizontal axes orientation.

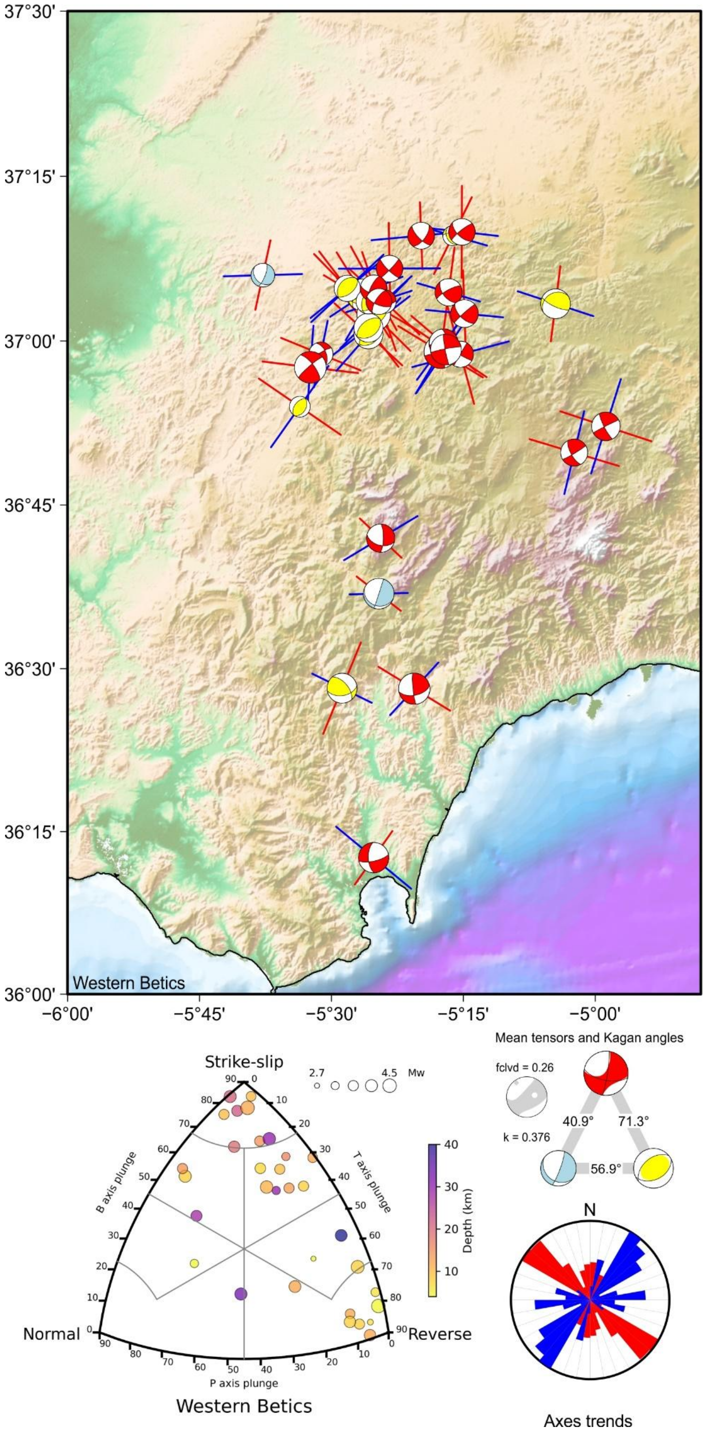

Fig. A19: Western Betics tectonic zone. Top map: focal mechanisms with maximum horizontal axis (P or B for normal ruptures) and minimum horizontal axis (T or B for reverse ruptures) orientation. Bottom left classification diagram for earthquake rupture types. Middle right: Average tensors (complete in gray) and Kagan angles between the average tensors for each rupture type. Bottom right: Rose diagram of maximum and minimum horizontal axes orientation.

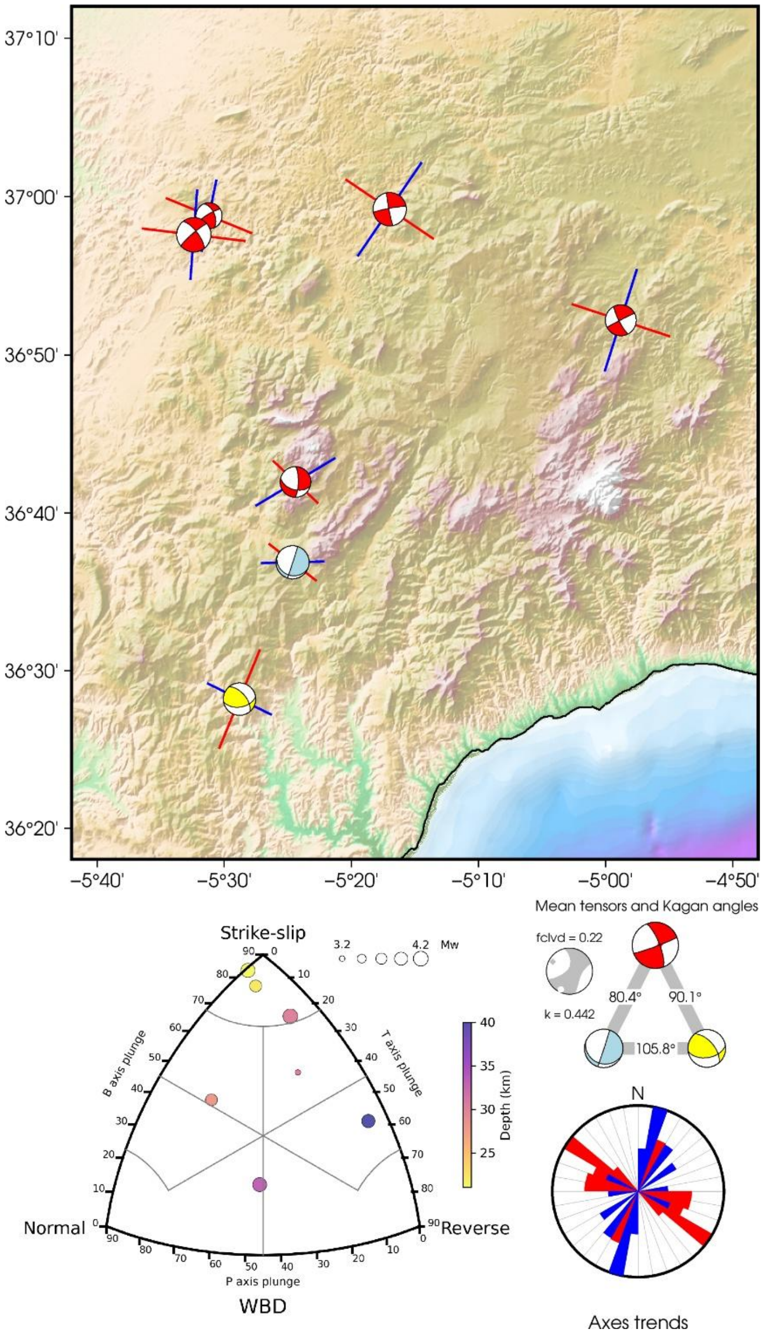

Fig. A20 Western Betics >20 km tectonic zone. Top map: focal mechanisms with maximum horizontal axis (P or B for normal ruptures) and minimum horizontal axis (T or B for reverse ruptures) orientation. Bottom left classification diagram for earthquake rupture types. Middle right: Average tensors (complete in gray) and Kagan angles between the average tensors for each rupture type. Bottom right: Rose diagram of maximum and minimum horizontal axes orientation.

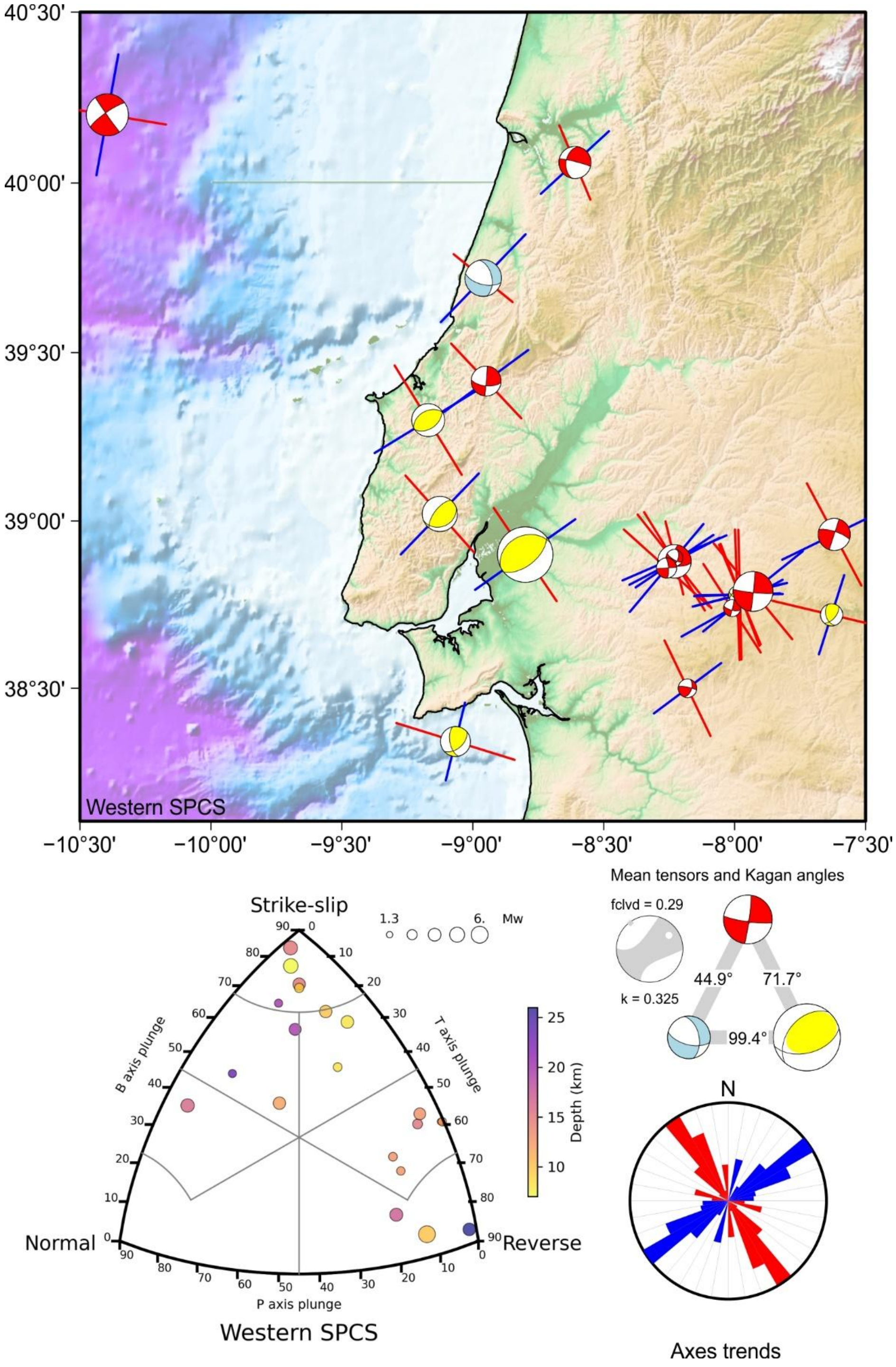

Fig. A21: Western Spanish Portugues Central System tectonic zone. Top map: focal mechanisms with maximum horizontal axis (P or B for normal ruptures) and minimum horizontal axis (T or B for reverse ruptures) orientation. Bottom left classification diagram for earthquake rupture types. Middle right: Average tensors (complete in gray) and Kagan angles between the average tensors for each rupture type. Bottom right: Rose diagram of maximum and minimum horizontal axes orientation.

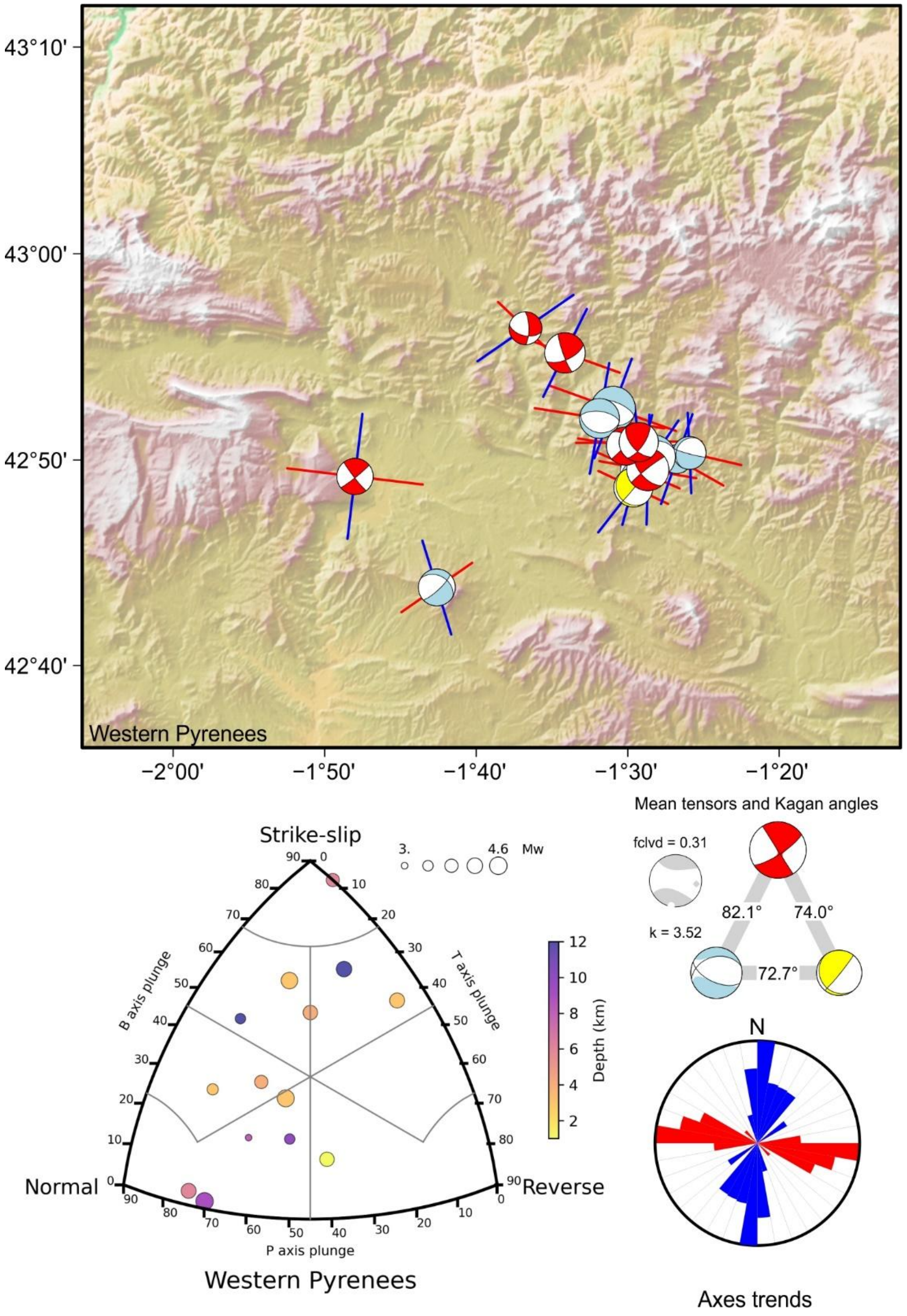

Fig. A22: Western Pyrenees tectonic zone. Top map: focal mechanisms with maximum horizontal axis (P or B for normal ruptures) and minimum horizontal axis (T or B for reverse ruptures) orientation. Bottom left classification diagram for earthquake rupture types. Middle right: Average tensors (complete in gray) and Kagan angles between the average tensors for each rupture type. Bottom right: Rose diagram of maximum and minimum horizontal axes orientation.

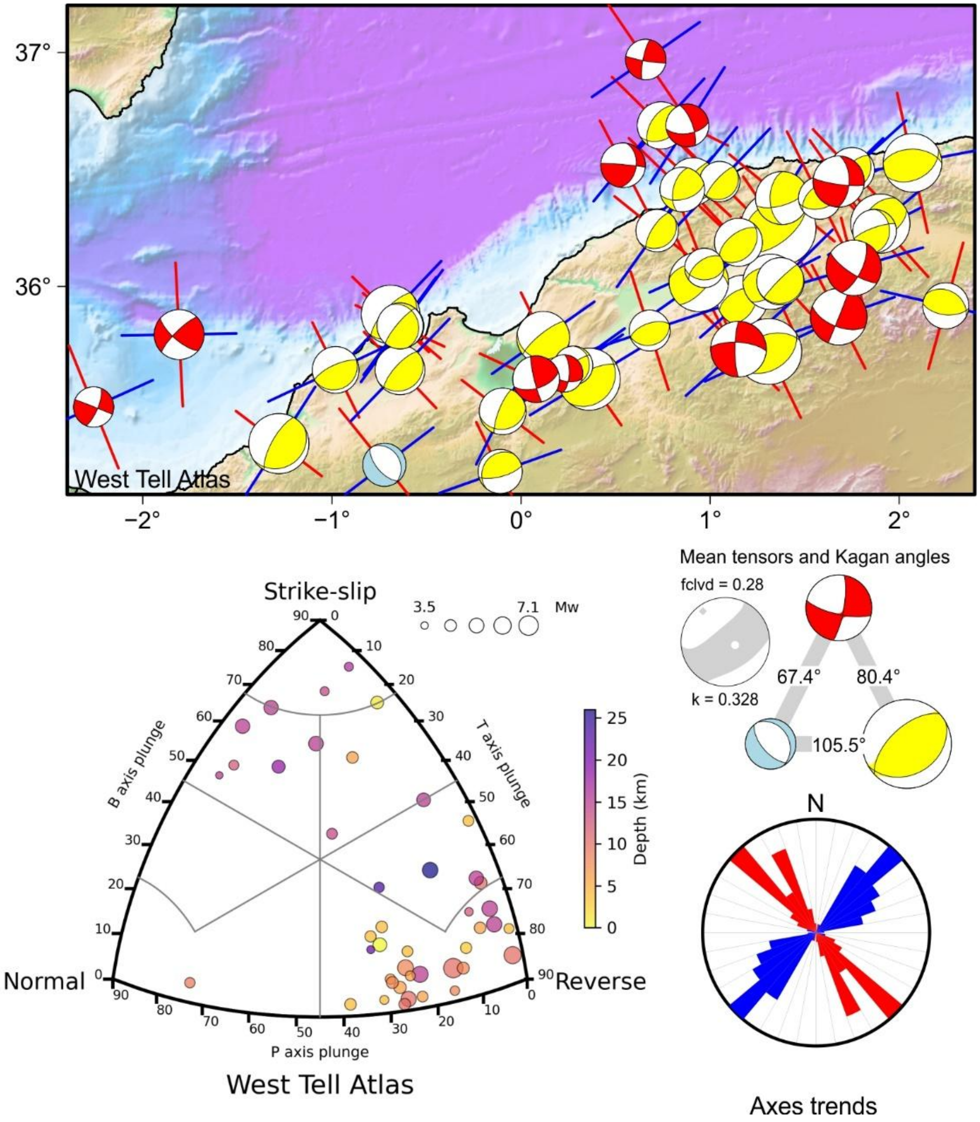

Fig. A23: West Tell Atlas tectonic zone. Top map: focal mechanisms with maximum horizontal axis (P or B for normal ruptures) and minimum horizontal axis (T or B for reverse ruptures) orientation. Bottom left classification diagram for earthquake rupture types. Middle right: Average tensors (complete in gray) and Kagan angles between the average tensors for each rupture type. Bottom right: Rose diagram of maximum and minimum horizontal axes orientation.

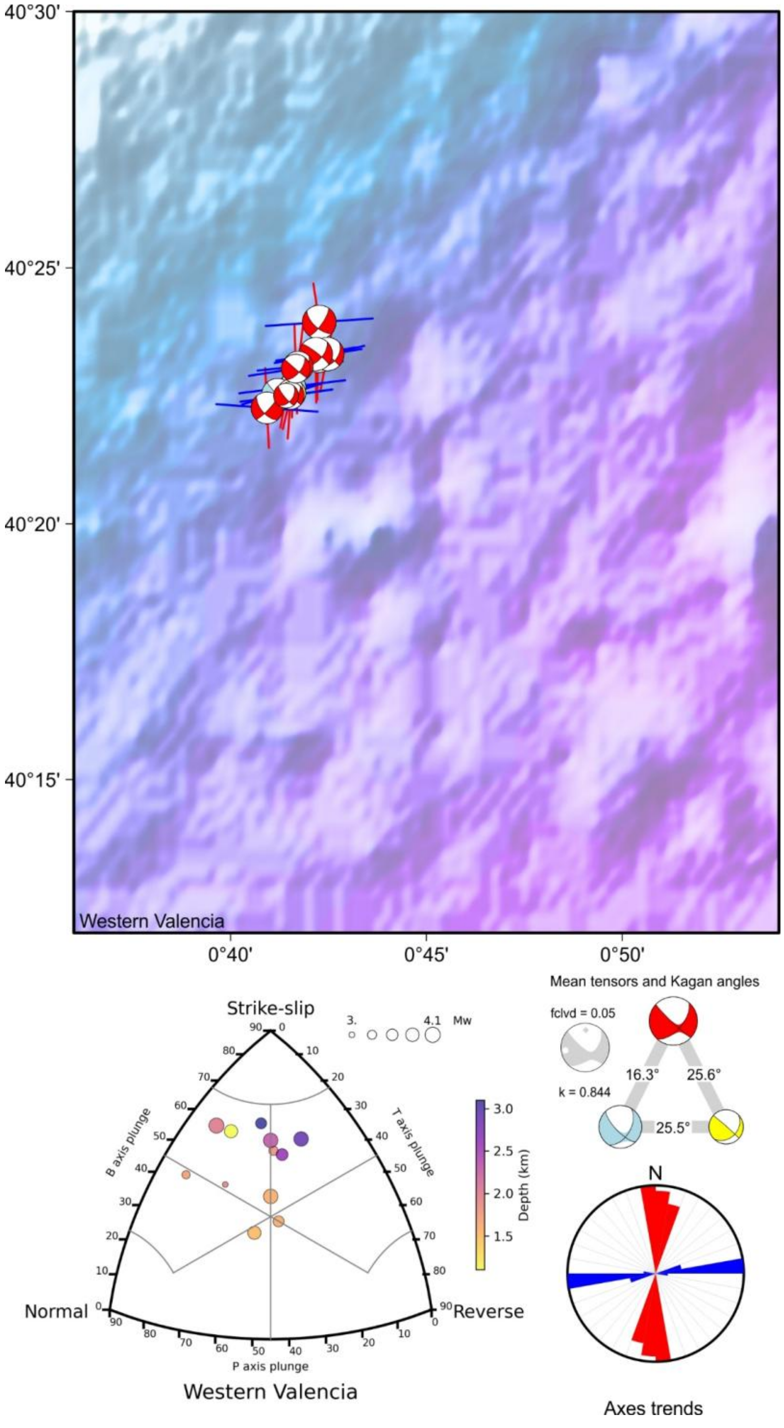

Fig. A24: Western Valencia tectonic zone. Top map: focal mechanisms with maximum horizontal axis (P or B for normal ruptures) and minimum horizontal axis (T or B for reverse ruptures) orientation. Bottom left classification diagram for earthquake rupture types. Middle right: Average tensors (complete in gray) and Kagan angles between the average tensors for each rupture type. Bottom right: Rose diagram of maximum and minimum horizontal axes orientation.

Appendix B

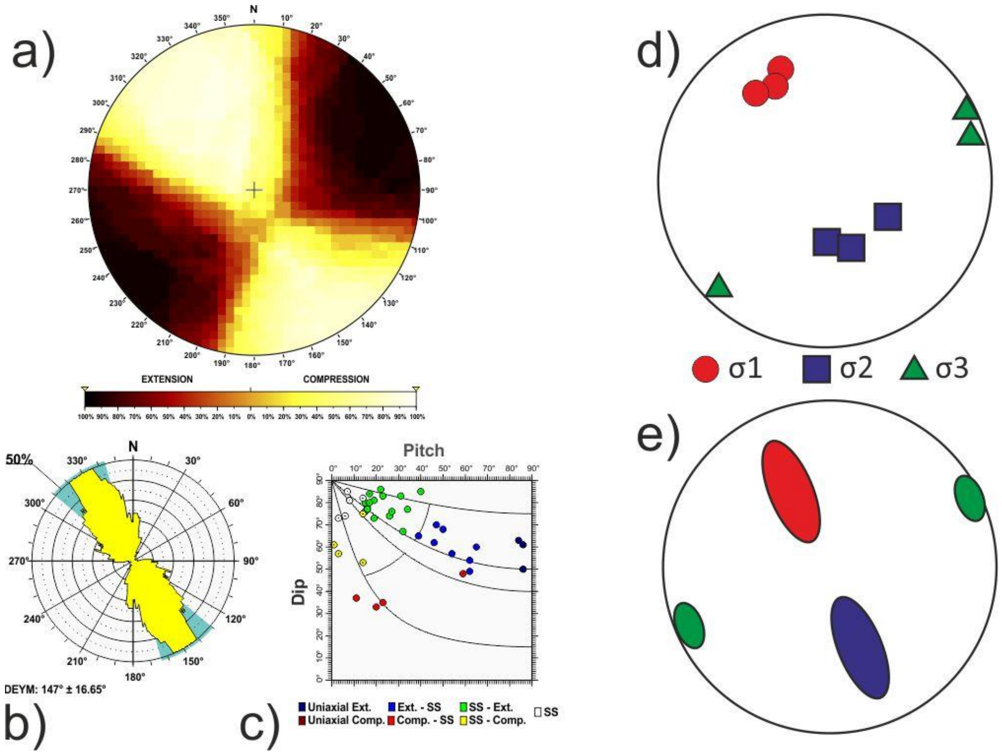

Fig. B1 Al Hoceima tectonic zone. Results of the stress and strain analyses for different zones: a) Right Dihedra solution. b) Rose diagram of the Dey (horizontal shortening direction) obtained from the Slip model. C) Pitch/Dip plot for the neo-formed nodal planes obtained from the Slip Model. d) Stress Inversion Results. e) Variability of the three principal stress axes of the stress inversion. e) Variability of the three principal stress axes of the stress inversion.

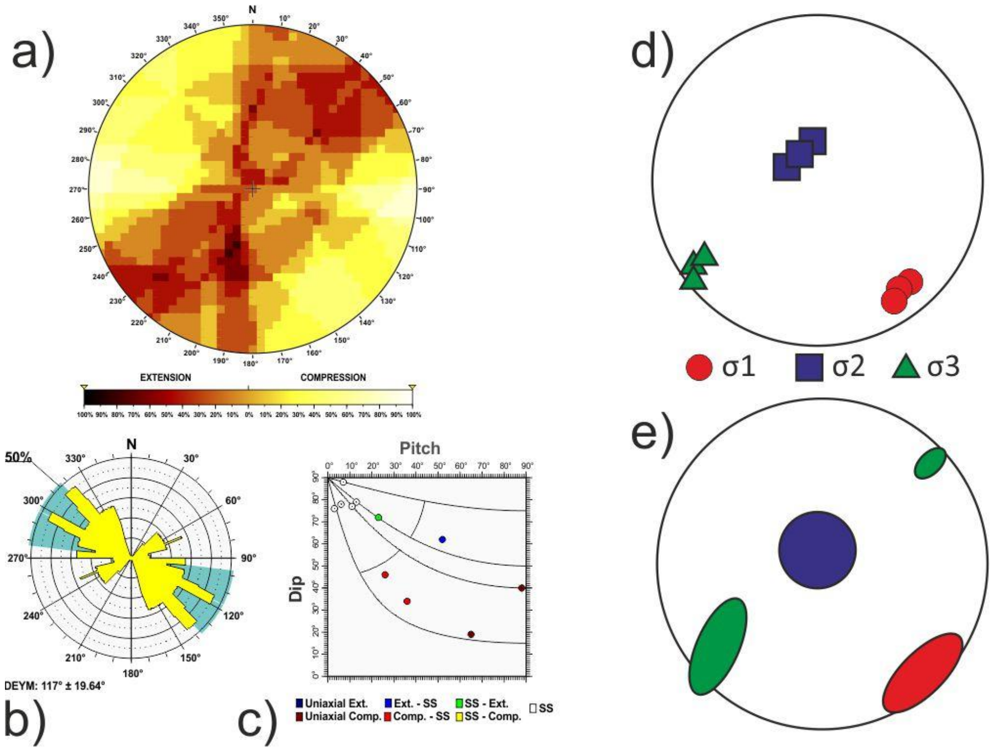

Fig. B2 Algarve tectonic zone. Results of the stress and strain analyses for different zones: a) Right Dihedra solution. b) Rose diagram of the Dey (horizontal shortening direction) obtained from the Slip model. C) Pitch/Dip plot for the neo-formed nodal planes obtained from the Slip Model. d) Stress Inversion Results. e) Variability of the three principal stress axes of the stress inversion.

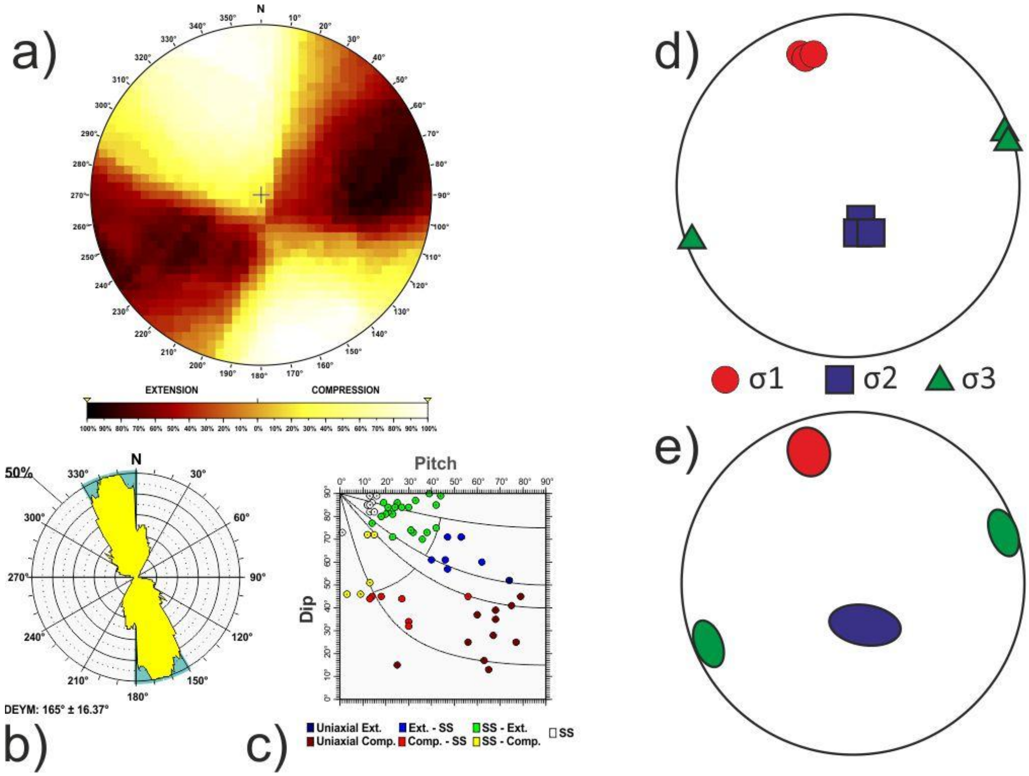

Fig. B3 Alboran Ridge tectonic zone. Results of the stress and strain analyses for different zones: a) Right Dihedra solution. b) Rose diagram of the Dey (horizontal shortening direction) obtained from the Slip model. C) Pitch/Dip plot for the neo-formed nodal planes obtained from the Slip Model. d) Stress Inversion Results. e) Variability of the three principal stress axes of the stress inversion.

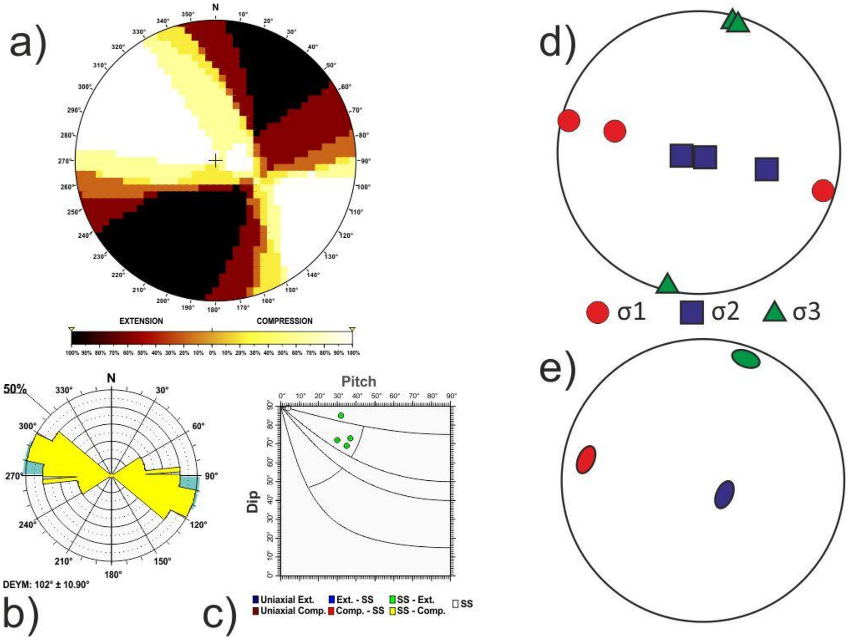

Fig. B4 Betics Antequera tectonic zone. Results of the stress and strain analyses for different zones: a) Right Dihedra solution. b) Rose diagram of the Dey (horizontal shortening direction) obtained from the Slip model. C) Pitch/Dip plot for the neo-formed nodal planes obtained from the Slip Model. d) Stress Inversion Results. e) Variability of the three principal stress axes of the stress inversion.

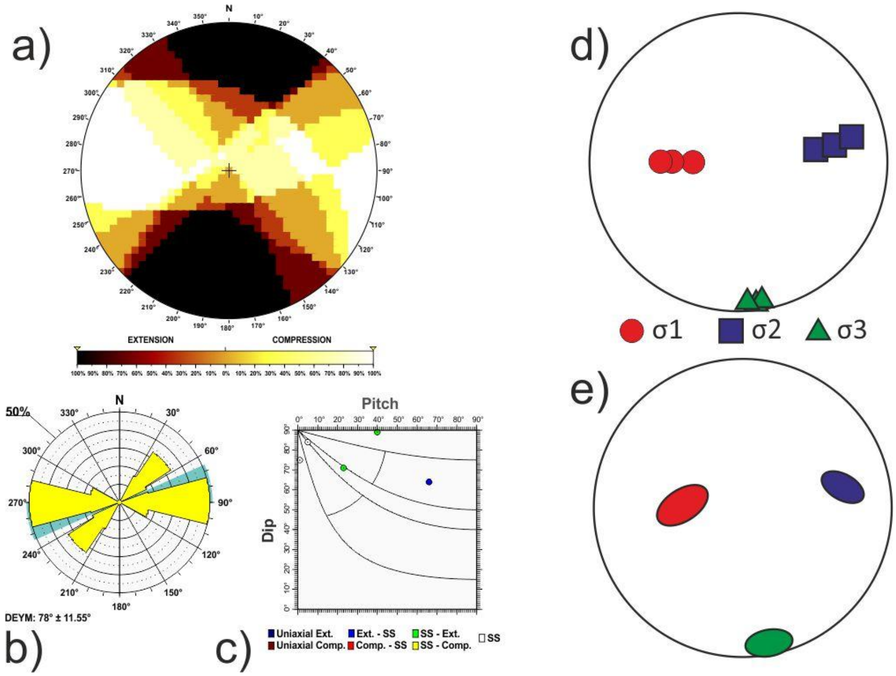

Fig. B5 Central Basins tectonic zone. Results of the stress and strain analyses for different zones: a) Right Dihedra solution. b) Rose diagram of the Dey (horizontal shortening direction) obtained from the Slip model. C) Pitch/Dip plot for the neo-formed nodal planes obtained from the Slip Model. d) Stress Inversion Results. e) Variability of the three principal stress axes of the stress inversion.

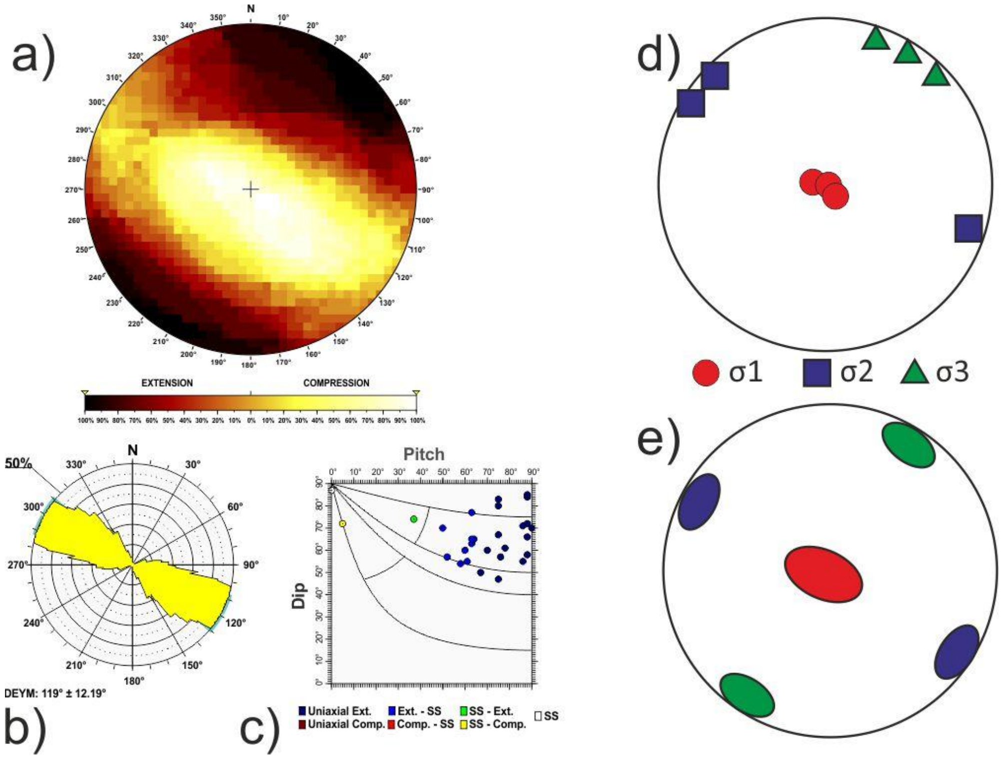

Fig. B6 Central Pyrenees tectonic zone. Results of the stress and strain analyses for different zones: a) Right Dihedra solution. b) Rose diagram of the Dey (horizontal shortening direction) obtained from the Slip model. C) Pitch/Dip plot for the neo-formed nodal planes obtained from the Slip Model. d) Stress Inversion Results. e) Variability of the three principal stress axes of the stress inversion.

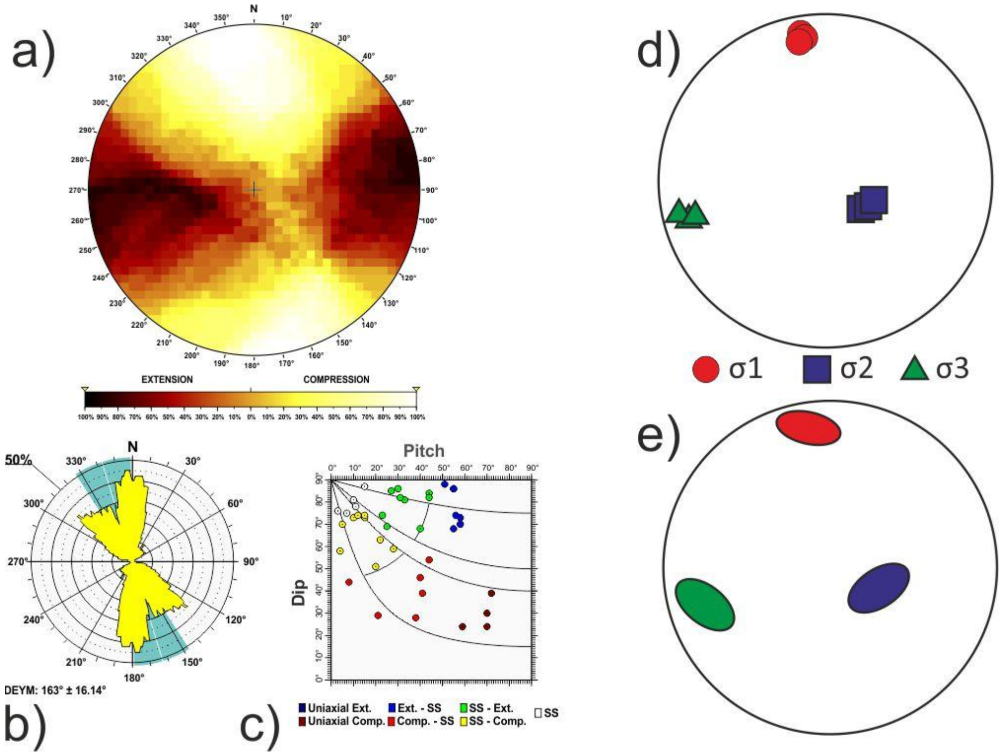

Fig. B7 Eastern Betics tectonic zone. Results of the stress and strain analyses for different zones: a) Right Dihedra solution. b) Rose diagram of the Dey (horizontal shortening direction) obtained from the Slip model. C) Pitch/Dip plot for the neo-formed nodal planes obtained from the Slip Model. d) Stress Inversion Results. e) Variability of the three principal stress axes of the stress inversion.

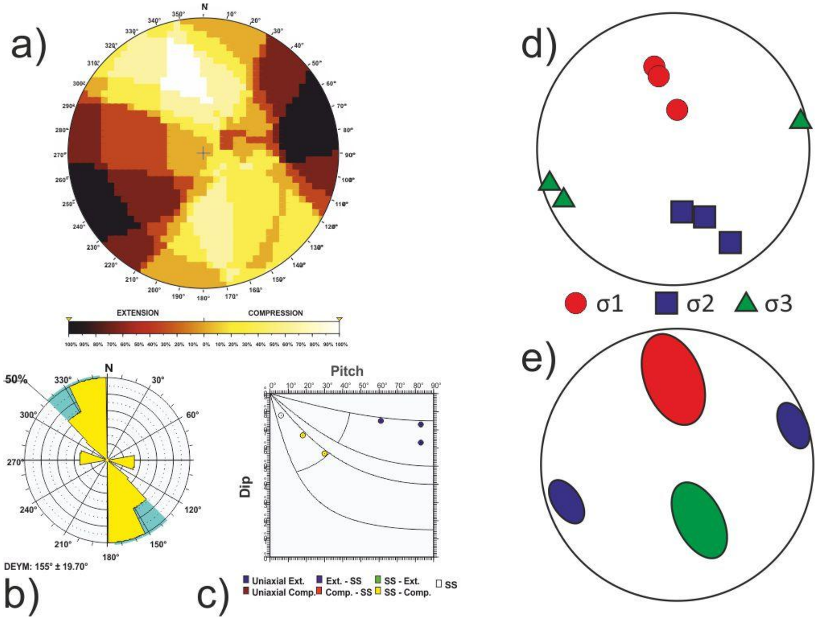

Fig. B8 Eastern Pyrenees tectonic zone. Results of the stress and strain analyses for different zones: a) Right Dihedra solution. b) Rose diagram of the Dey (horizontal shortening direction) obtained from the Slip model. C) Pitch/Dip plot for the neo-formed nodal planes obtained from the Slip Model. d) Stress Inversion Results. e) Variability of the three principal stress axes of the stress inversion.

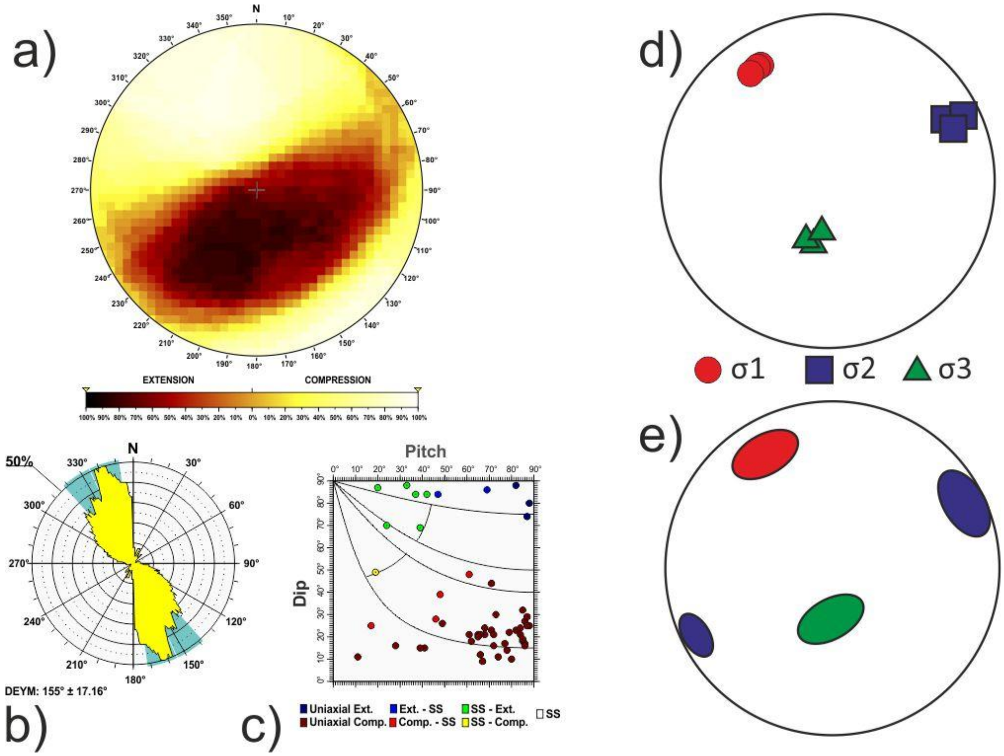

Fig. B9 East Tell Atlas tectonic zone. Results of the stress and strain analyses for different zones: a) Right Dihedra solution. b) Rose diagram of the Dey (horizontal shortening direction) obtained from the Slip model. C) Pitch/Dip plot for the neo-formed nodal planes obtained from the Slip Model. d) Stress Inversion Results. e) Variability of the three principal stress axes of the stress inversion.

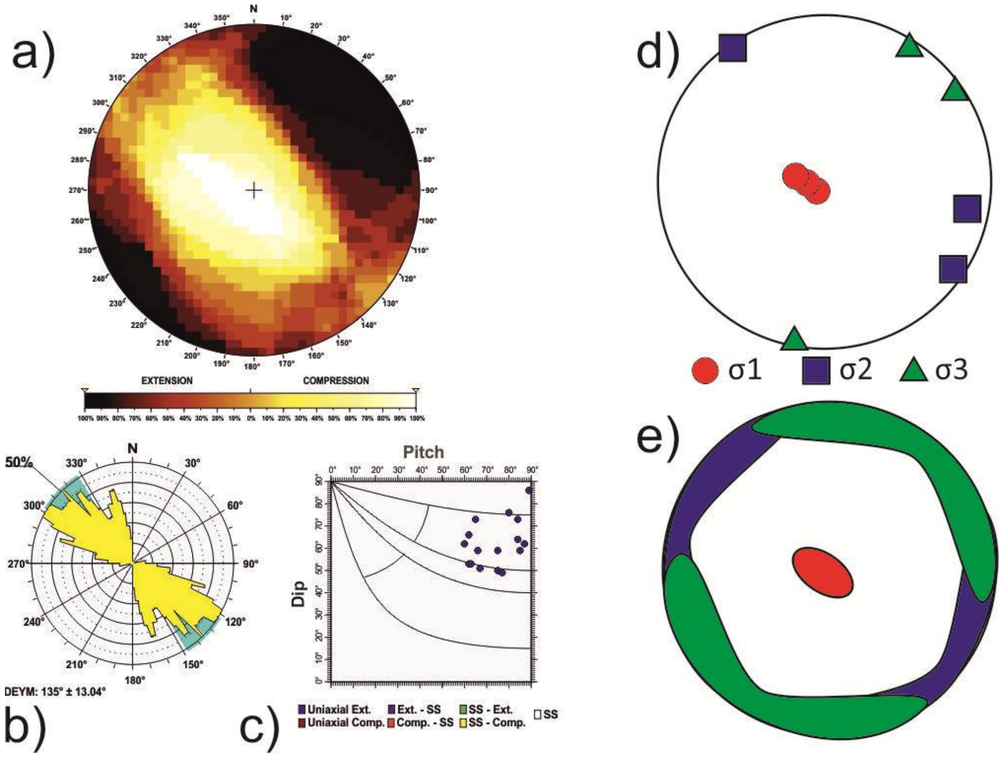

Fig. B10 Granada Basin tectonic zone. Results of the stress and strain analyses for different zones: a) Right Dihedra solution. b) Rose diagram of the Dey (horizontal shortening direction) obtained from the Slip model. C) Pitch/Dip plot for the neo-formed nodal planes obtained from the Slip Model. d) Stress Inversion Results. e) Variability of the three principal stress axes of the stress inversion.

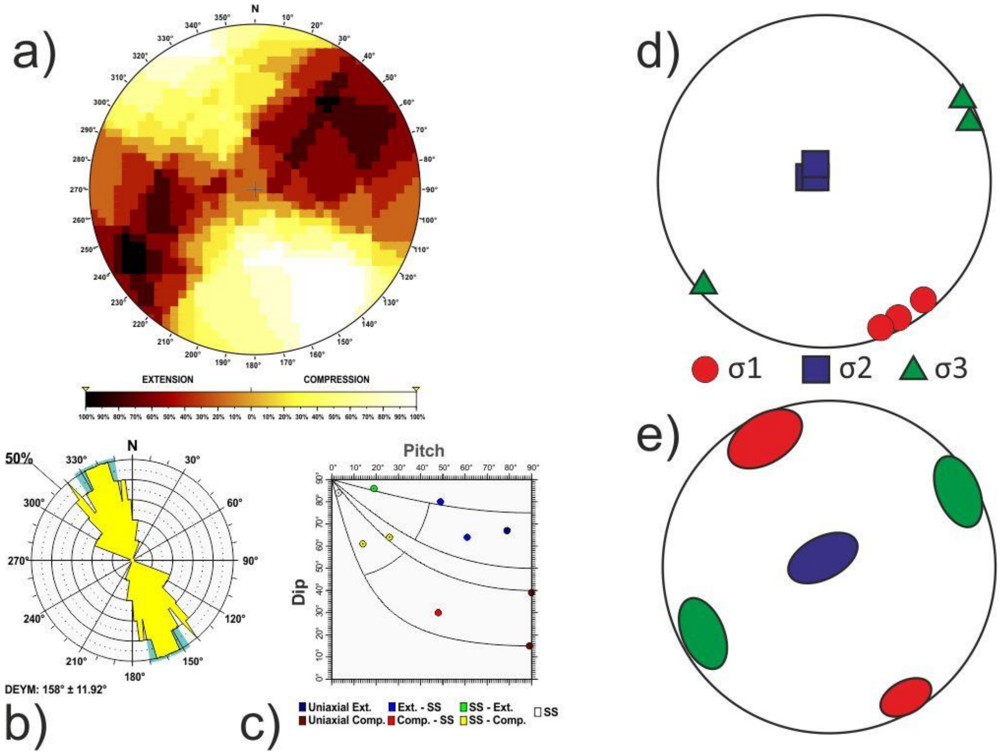

Fig. B11 Gulf of Cádiz tectonic zone. Results of the stress and strain analyses for different zones: a) Right Dihedra solution. b) Rose diagram of the Dey (horizontal shortening direction) obtained from the Slip model. C) Pitch/Dip plot for the neo-formed nodal planes obtained from the Slip Model. d) Stress Inversion Results. e) Variability of the three principal stress axes of the stress inversion.

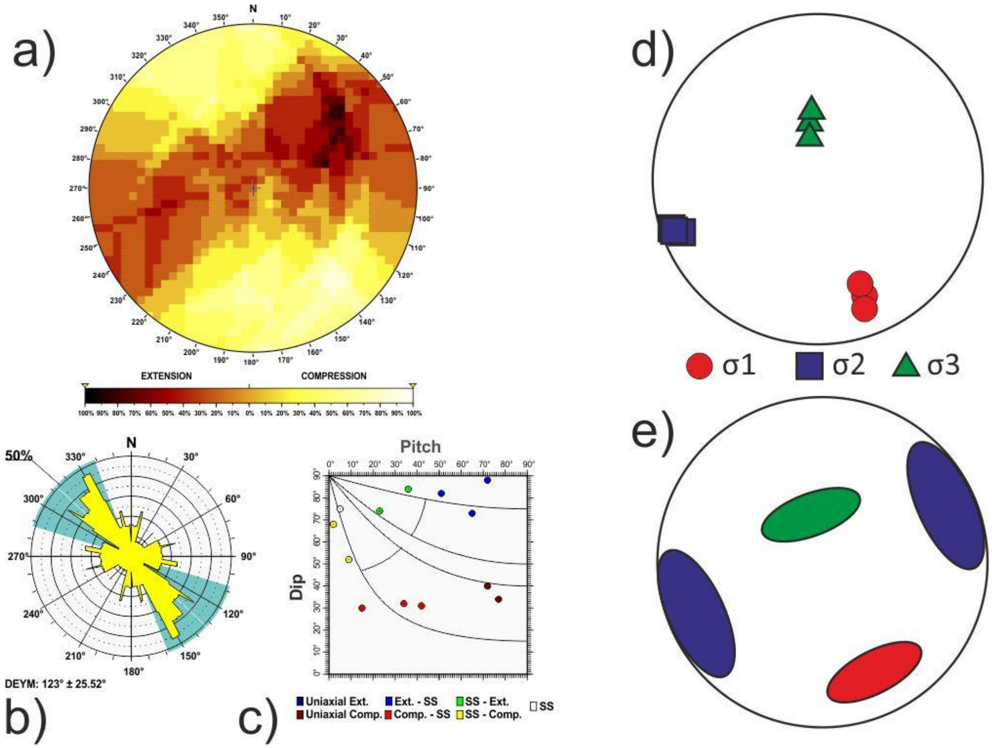

Fig. B12 Gorringe - Horseshoe tectonic zone. Results of the stress and strain analyses for different zones: a) Right Dihedra solution. b) Rose diagram of the Dey (horizontal shortening direction) obtained from the Slip model. C) Pitch/Dip plot for the neo-formed nodal planes obtained from the Slip Model. d) Stress Inversion Results. e) Variability of the three principal stress axes of the stress inversion.

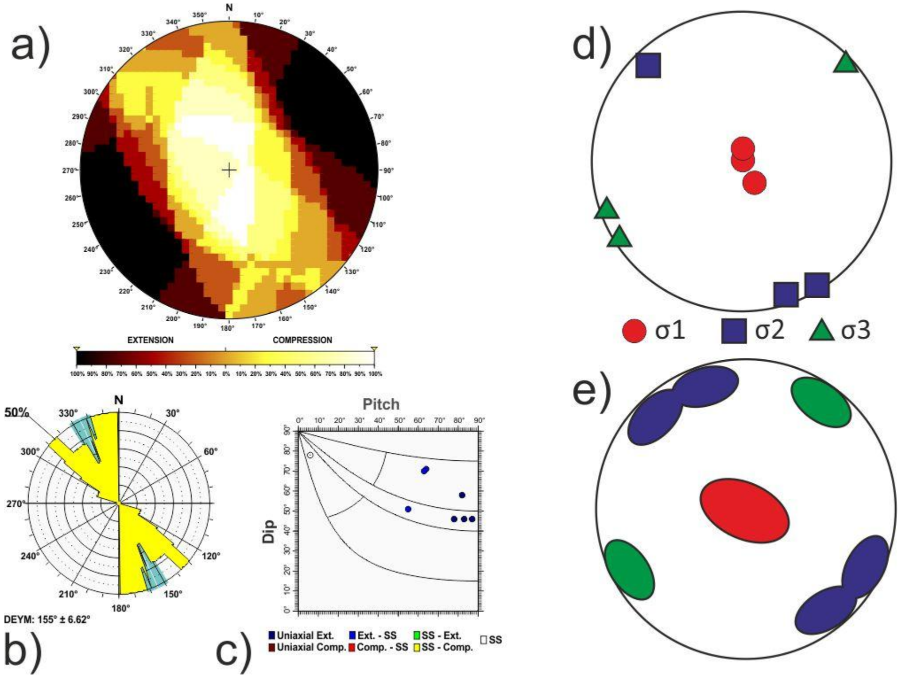

Fig. B13 Iberian Chain tectonic zone. Results of the stress and strain analyses for different zones: a) Right Dihedra solution. b) Rose diagram of the Dey (horizontal shortening direction) obtained from the Slip model. C) Pitch/Dip plot for the neo-formed nodal planes obtained from the Slip Model. d) Stress Inversion Results. e) Variability of the three principal stress axes of the stress inversion.

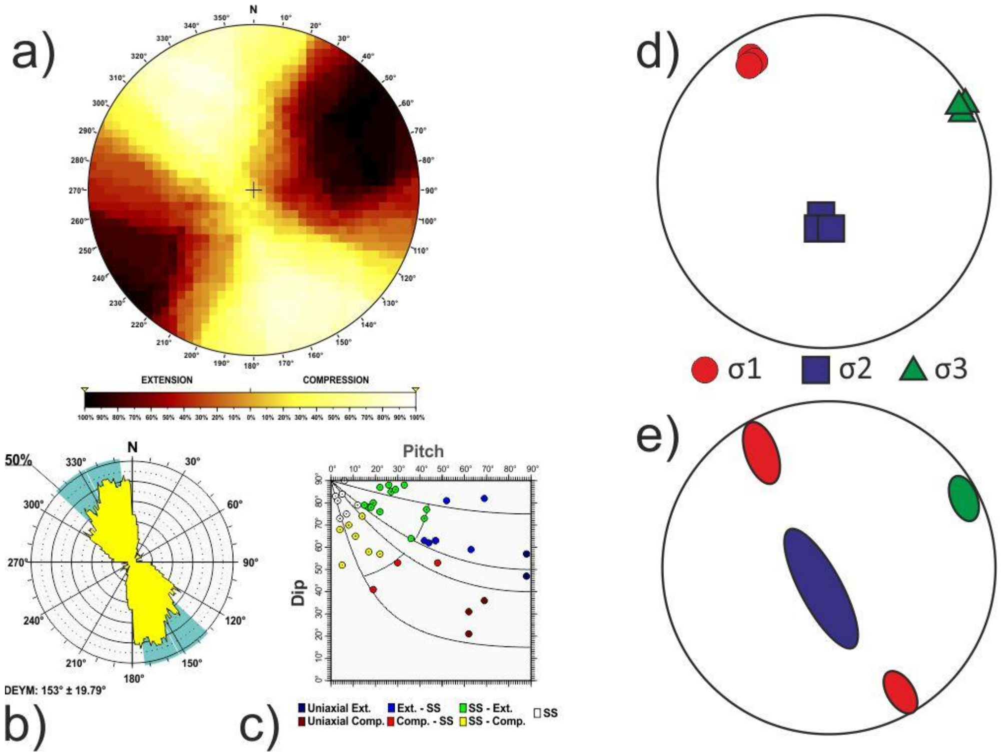

Fig. B14 Northern Alboran tectonic zone. Results of the stress and strain analyses for different zones: a) Right Dihedra solution. b) Rose diagram of the Dey (horizontal shortening direction) obtained from the Slip model. C) Pitch/Dip plot for the neo-formed nodal planes obtained from the Slip Model. d) Stress Inversion Results. e) Variability of the three principal stress axes of the stress inversion.

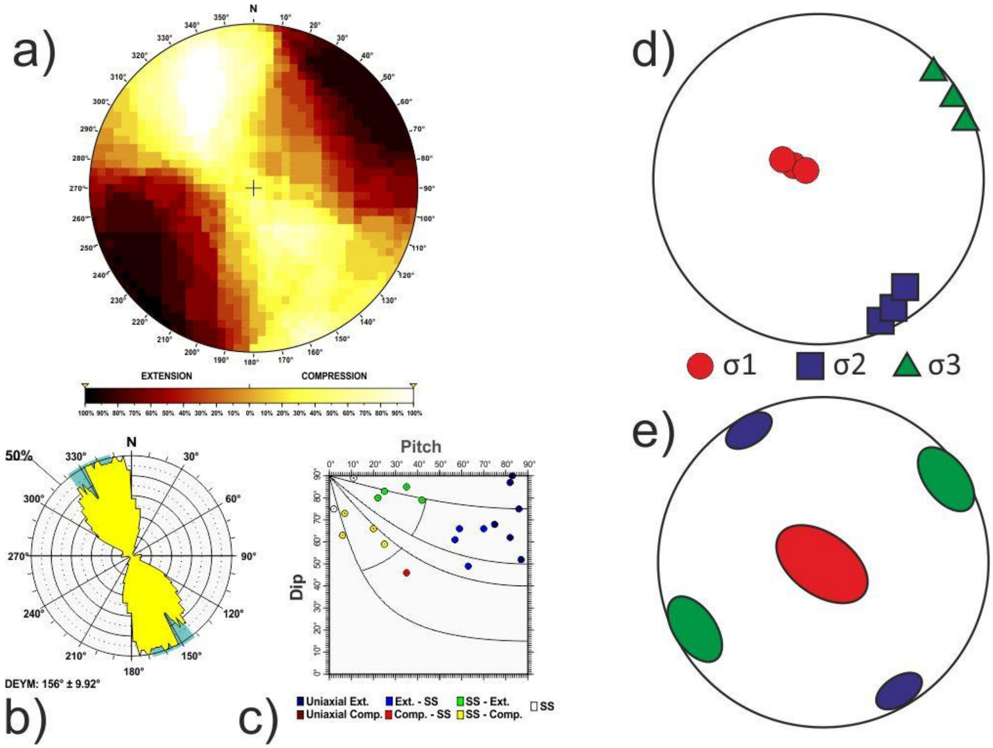

Fig. B15 NW Galicia tectonic zone. Results of the stress and strain analyses for different zones: a) Right Dihedra solution. b) Rose diagram of the Dey (horizontal shortening direction) obtained from the Slip model. C) Pitch/Dip plot for the neo-formed nodal planes obtained from the Slip Model. d) Stress Inversion Results. e) Variability of the three principal stress axes of the stress inversion.

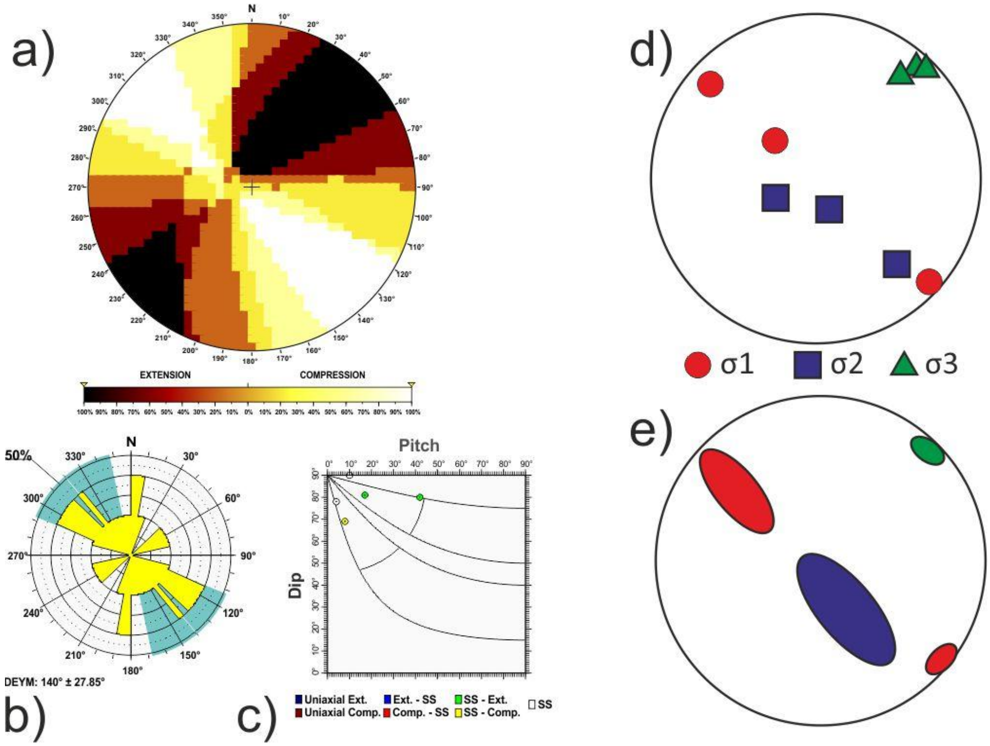

Fig. B16 Offshore Atlantic tectonic zone. Results of the stress and strain analyses for different zones: a) Right Dihedra solution. b) Rose diagram of the Dey (horizontal shortening direction) obtained from the Slip model. C) Pitch/Dip plot for the neo-formed nodal planes obtained from the Slip Model. d) Stress Inversion Results. e) Variability of the three principal stress axes of the stress inversion.

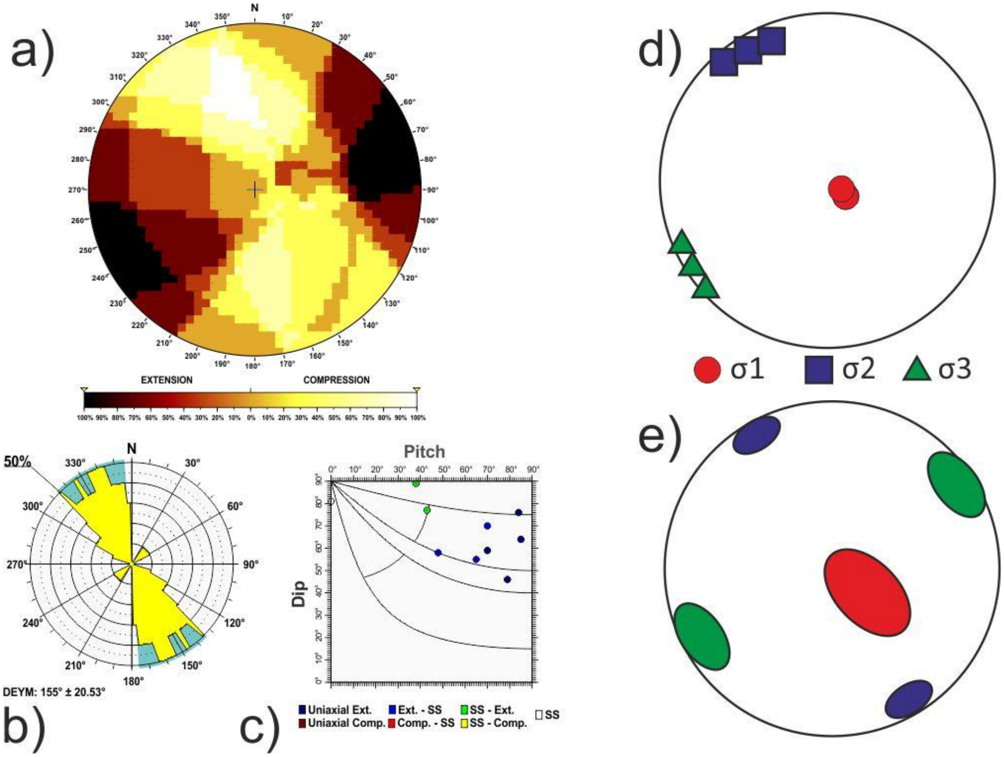

Fig. B17 Southern Valencia tectonic zone. **Results of the stress and strain analyses for different zones: a) Right Dihedra solution. b) Rose diagram of the Dey (horizontal shortening direction) obtained from the Slip model. C) Pitch/Dip plot for the neo-formed nodal planes obtained from the Slip Model. d) Stress Inversion Results. e) Variability of the three principal stress axes of the stress inversion.**

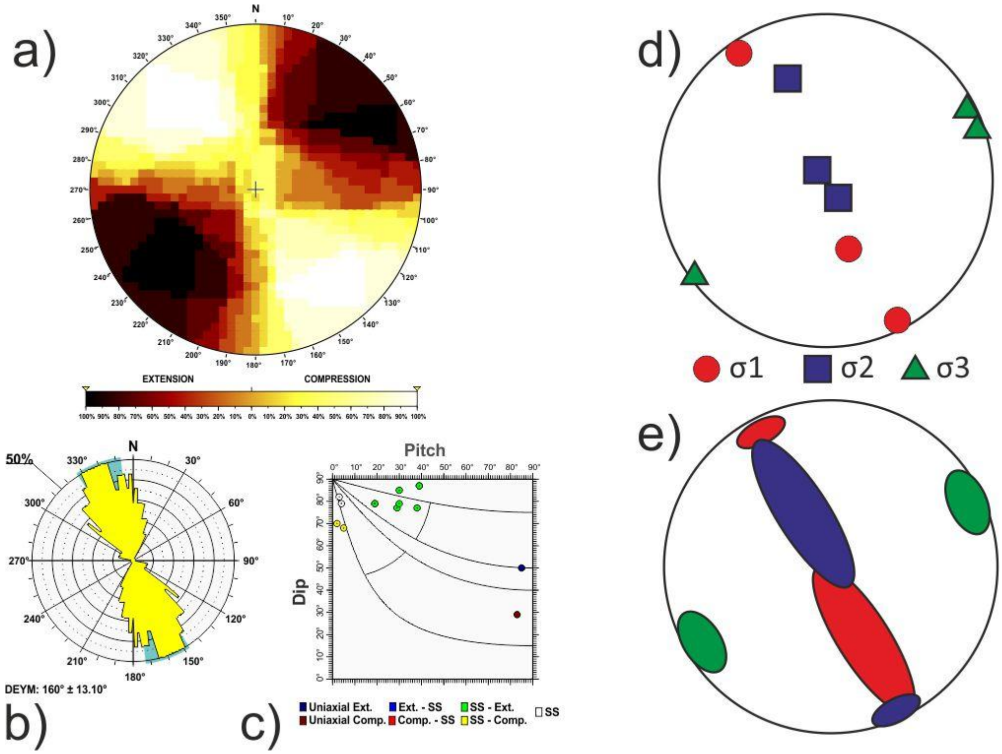

Fig. B18 Western Alcaraz Arch tectonic zone. Results of the stress and strain analyses for different zones: a) Right Dihedra solution. b) Rose diagram of the Dey (horizontal shortening direction) obtained from the Slip model. C) Pitch/Dip plot for the neo-formed nodal planes obtained from the Slip Model. d) Stress Inversion Results. e) Variability of the three principal stress axes of the stress inversion.

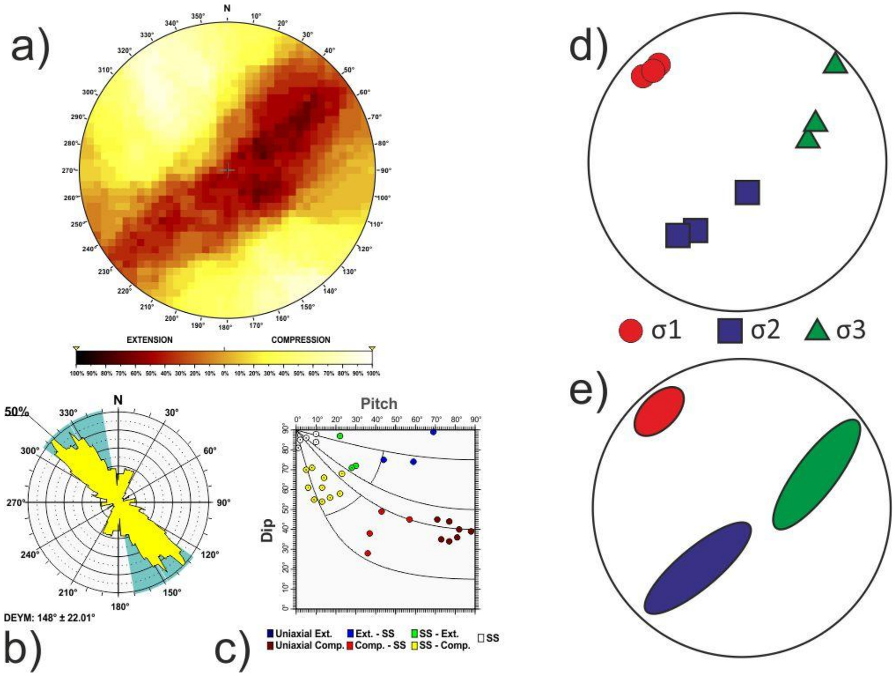

Fig. B19 Western Betics tectonic zone. Results of the stress and strain analyses for different zones: a) Right Dihedra solution. b) Rose diagram of the Dey (horizontal shortening direction) obtained from the Slip model. C) Pitch/Dip plot for the neo-formed nodal planes obtained from the Slip Model. d) Stress Inversion Results. e) Variability of the three principal stress axes of the stress inversion.

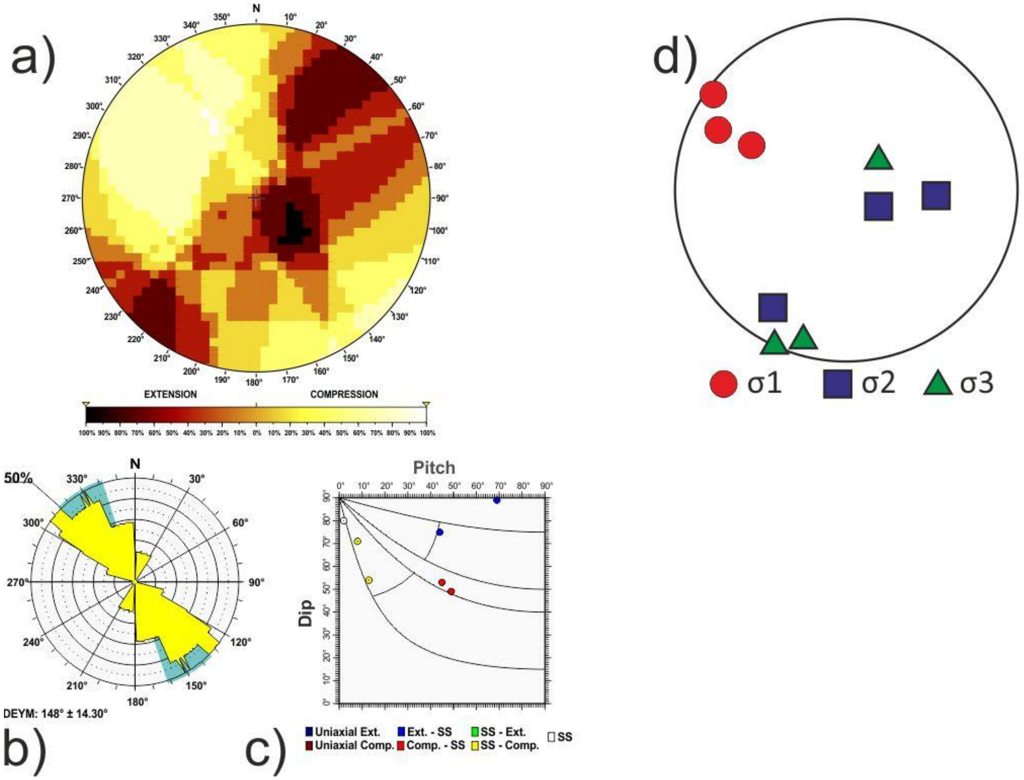

Fig. B20 **Western Betics > 20 km tectonic zone. Results of the stress and strain analyses for different zones: a) Right Dihedra solution. b) Rose diagram of the Dey (horizontal shortening direction) obtained from the Slip model. C) Pitch/Dip plot for the neo-formed nodal planes obtained from the Slip Model. d) Stress Inversion Results. e) Variability of the three principal stress axes of the stress inversion.**

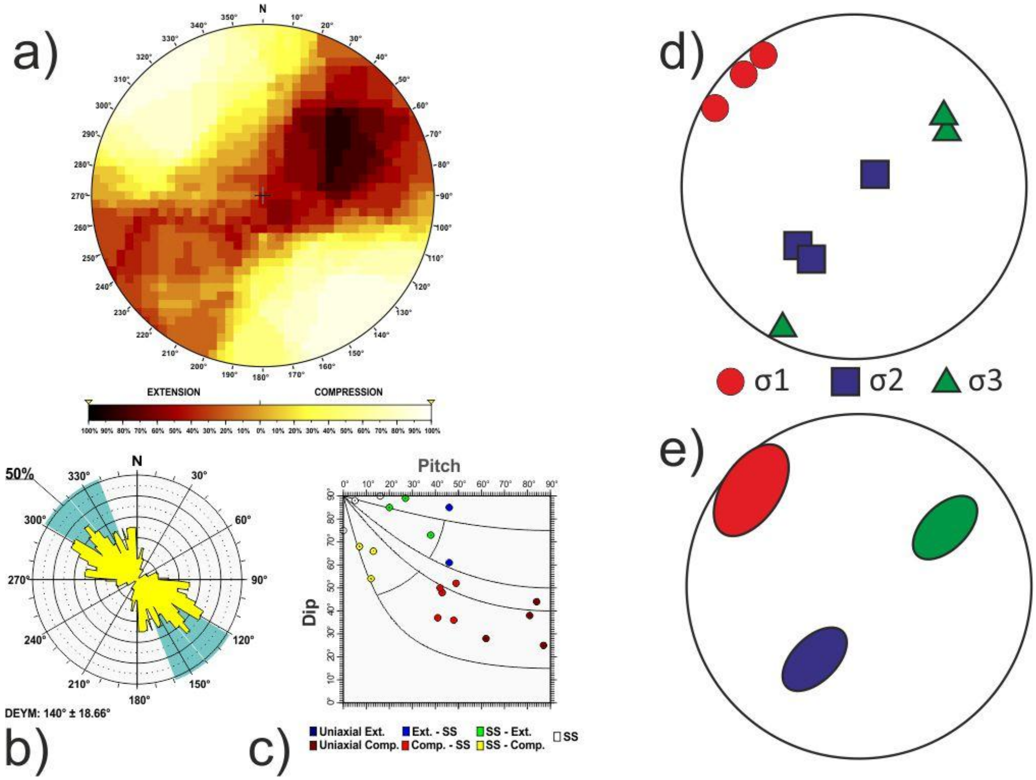

Fig. B21 Western Spanish Portuguese Central System tectonic zone. Results of the stress and strain analyses for different zones: a) Right Dihedra solution. b) Rose diagram of the Dey (horizontal shortening direction) obtained from the Slip model. C) Pitch/Dip plot for the neo-formed nodal planes obtained from the Slip Model. d) Stress Inversion Results. e) Variability of the three principal stress axes of the stress inversion.

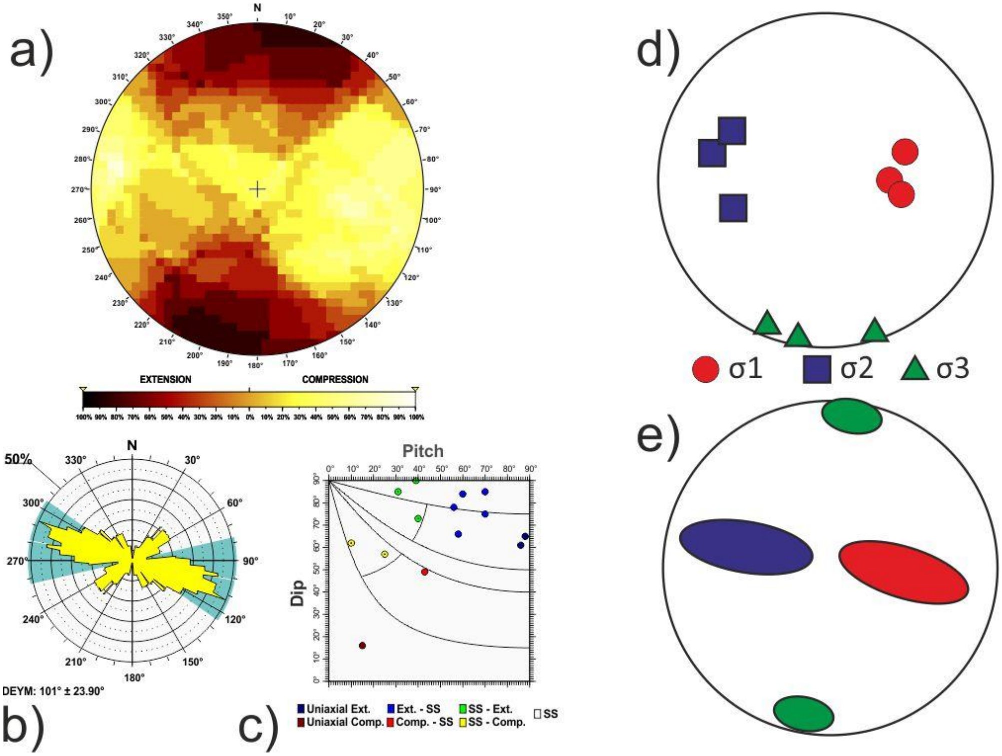

Fig. B22 Western Pyrenees tectonic zone. Results of the stress and strain analyses for different zones: a) Right Dihedra solution. b) Rose diagram of the Dey (horizontal shortening direction) obtained from the Slip model. C) Pitch/Dip plot for the neo-formed nodal planes obtained from the Slip Model. d) Stress Inversion Results. e) Variability of the three principal stress axes of the stress inversion.

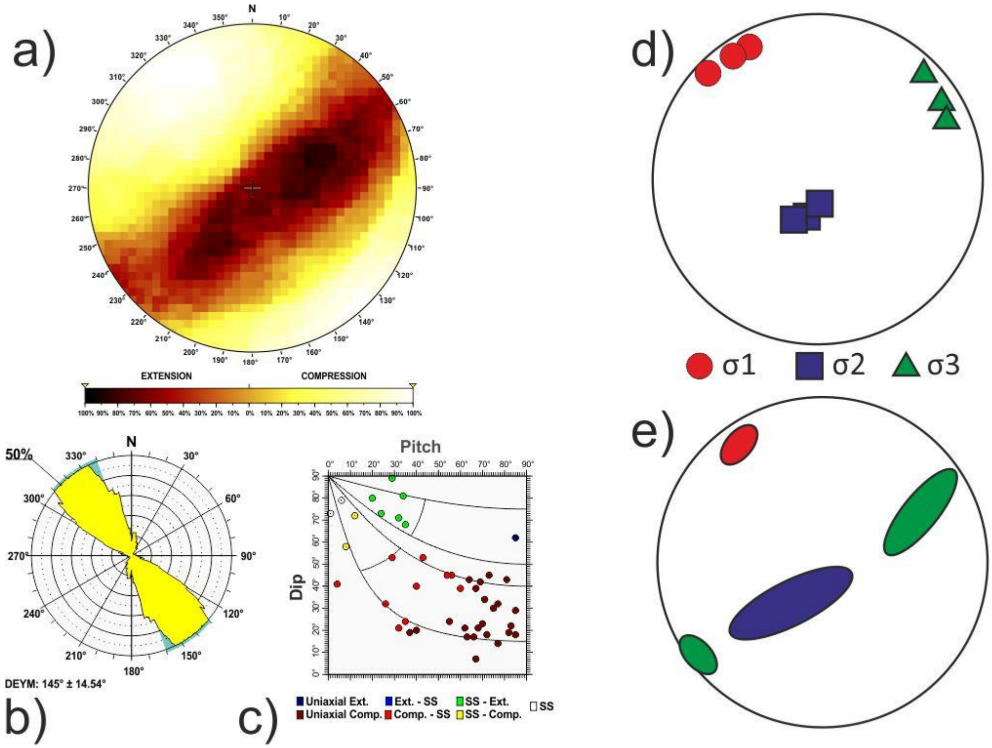

Fig. B23 West Tell Atlas tectonic zone. **Results of the stress and strain analyses for different zones: a) Right Dihedra solution. b) Rose diagram of the Dey (horizontal shortening direction) obtained from the Slip model. C) Pitch/Dip plot for the neo-formed nodal planes obtained from the Slip Model. d) Stress Inversion Results. e) Variability of the three principal stress axes of the stress inversion.**

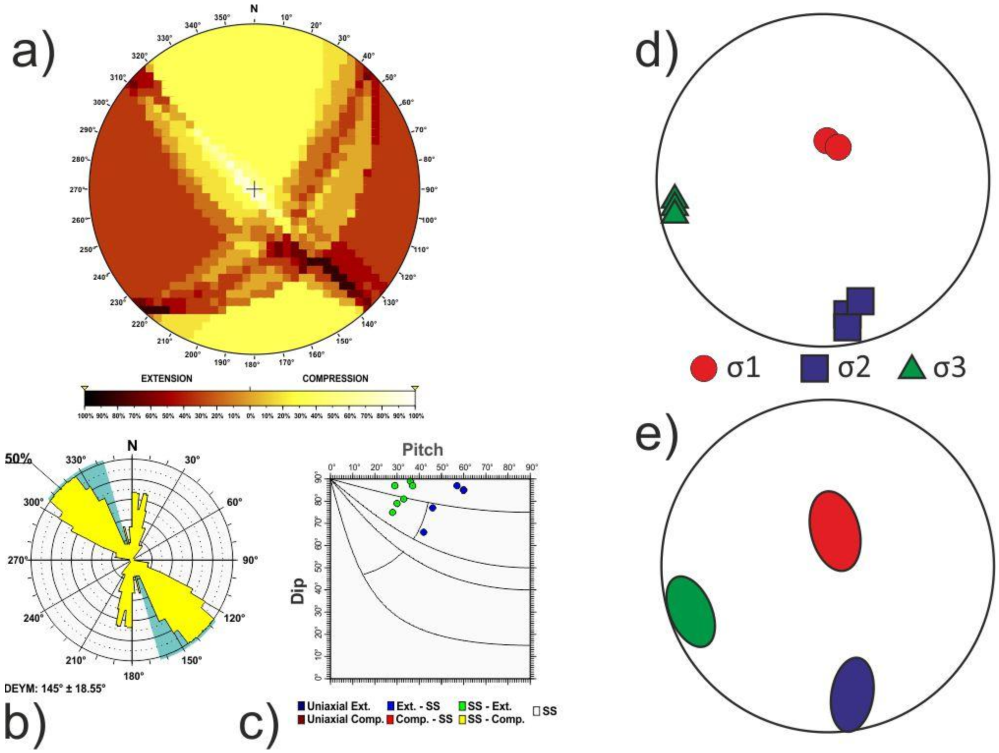

Fig. B24 Western Valencia tectonic zone. Results of the stress and strain analyses for different zones: a) Right Dihedra solution. b) Rose diagram of the Dey (horizontal shortening direction) obtained from the Slip model. C) Pitch/Dip plot for the neo-formed nodal planes obtained from the Slip Model. d) Stress Inversion Results. e) Variability of the three principal stress axes of the stress inversion.

Data availability

Focal mechanisms used in this study are compiled from: Braunmiller et al., 2002; Carreño et al., 2008; Cesca et al., 2021; Chevrot et al., 2011; Custodio et al., 2016; Del Pie Perales, 2016; Dziewonski et al., 1981; Ekström et al., 2012; ETH-Swiss Seismological Service; GFZ-Postdam; Global Centroid Moment Tensor; IAG Instituto Andaluz de Geofísica; IGN Instituto Geográfico Nacional de España; IPMA Portuguese Institute for Sea and Atmosphere; INGV Istituto Nazionale di Geofisica e Vulcanologia; Martín et al., 2015; Matos et al., 2018; Olaiz et al.2024; Pondrelli et al., 2002, 2004; Rueda and Mezcua, 2005; Scognamiglio et al., 2006; Stich et al., 2003, 2005, 2006, 2010, 2020 and Villaseñor et al., 2020.

Supplementary material includes the focal mechanism compiled and the new focal mechanism calculated for this study. The database is available at a Zenodo repository (https://doi.org/10.5281/zenodo.14326528). A database encompassing both the results of this study and previous data from World Stress Map, standardized in accordance with World Stress Map guidelines is accessible at https://doi.org/10.5281/zenodo.14326528.

Author contribution

AO, JAAG, GDV, AMM conceived the idea. AO, JAAG, GDV, AMM, JVC, SC, DV and OH performed the formal analysis, investigation and methodology. JVC and DN calculated the new focal mechanisms. AO, JAAG, GDV, AMM, SC and OH completed the supervision and visualization of the manuscript. AO and OH worked on the data curation. AO, JAAG, GDV, AMM, OH prepared the original manuscript; all the authors contributed to the review and editing. JAAG and AMM worked on funding acquisition

Competing interest

The contact author has declared that none of the authors has any competing interests

Acknowledgements

The Generic Mapping Tools (GMT) were used for figure plotting (Wessel and Smith, 1995). The authors wish to express their appreciation to Dr. Antonio Casas, Prof. Klaus Reicherter, an anonymous reviewer and the editor for their insightful comments and suggestions, which have greatly improved this manuscript.

Financial support

The authors acknowledge support from the projects GEOMARHIS (PID2022-138360NB-I00) and model_SHaKER (PID2021-124155NB-C31) funded by the Ministry of Science, Innovation and Universities of Spain.

References

Amadei, B., and Stephansson, O.: Rock Stress and its measurements, 1st ed., Chapman and Hall, New York, 9401062471, 1997.

Ammar, A., Mauffret, A., Gorini, C. and Jabour, H.: The tectonic structure of the Alboran Margin of Morocco. Rev. Soc. Geo. España, 20 (3-4): 247-271, ISSN 0214-2708, 2007.

Angelier, J., and Mechler, P.: Sur une méthode graphique de recherche des contraintes principales egalement utilisable en tectonique et en seismologie: La methode des diedres droites, Bull. Soc. Geol. Fr., 7(19), 1309 – 1318, https://doi.org/10.2113/gssgfbull.S7-XIX.6.1309, 1977.

Alasset, P.J. and Meghraoui, M.: Active faulting in the western Pyrénées (France): Paleoseismic evidence for late Holocene ruptures. Tectonophysics 409 (2005) 39 – 54, https://doi.org/10.1016/j.tecto.2005.08.019, 2005

Alvarez-Gómez, J.A.: FMC—earthquake focal mechanisms data management, cluster and classification. SoftwareX 9, 299–307. https://doi.org/10.1016/j.softx.2019.03.008, 2019.

Álvaro, M., Capote, R. and Vegas, R.: Un modelo de evolución geotectónica para la Cadena Celtibérica. Acta Geologica Hispanica. Homenage a LIuis Sole i Sabaris, 14, 172-177, 1979

Ancochea, E. and Huertas, M.J.: Radiometric ages and time–space distribution of volcanism in the Campo de Calatrava Volcanic Field (Iberian Peninsula). J. Iber. Geol. 47:209–223 https://doi.org/10.1007/s41513-021-00167-y, 2021.

Arcila, M. and Muñoz–Martín, A.: Integrated perspective of the present–day stress and strain regime in Colombia from analysis of earthquake focal mechanisms and geodetic data. In: Gómez, J. & Pinilla–Pachon, A.O. (editors), The Geology of Colombia, Volume 4 Quaternary. Servicio Geológico Colombiano, Publicaciones Geológicas Especiales 38, 21 pp. Bogotá. https://doi.org/10.32685/pub.esp.38.2019.17, 2020.

Arlegui, L.E., Simón, J.L., Lisle, R.J. and Orife, T.: Late Pliocene-Pleistocene stress field in the Teruel and Jiloca grabens (eastern Spain): contribution of a new method of stress inversion. J. Struc. Geol. 27, 693–705, https://doi.org/10.1016/j.jsg.2004.10.013, 2005.

Asensio, E., Khazaradze, G., Echeverria, A., King, R.W. and Vilajosana, I.: GPS studies of active deformation in the Pyrenees. Geophys. J. Int. 190, 913–921. doi: 10.1111/j.1365-246X.2012.05525.x, 2012.

Bailey, I. W., Alpert, L. A., Becker, T. W., and Miller, M. S.: Co-seismic deformation of deep slabs based on summed CMT data. J. Geophys. Res: Solid Earth, 117(B4), https://doi.org/10.1029/2011JB008943, 2012.

Barcos, L., Balanyá, J.C., Díaz-Azpiroz, M., Expósito, I. and Jiménez-Bonilla, A.: Kinematics of the Torcal Shear Zone: Transpressional tectonics in a salient-recess transition at the northern Gibraltar Arc. Tectonophysics 663- 62-77. http://dx.doi.org/10.1016/j.tecto.2015.05.002, 2015.

Bell, J. S., Caillet, G. and Lemarrec, A.,: The Present-Day Stress Regime of the Southwestern Part of the Aquitaine Basin, France, as Indicated by Oil-Well Data, J. Struc. Geol., 14(8-9), 1019-1032, doi:10.1016/0191-8141(92)90033-S, 1992.

Bolillot, G. and Malod, J.: The North and North-West Spanish continental margin: a review. Rev. Soc. Geol. España, 1, 295-316, 1988.

Borges, J. F., Bezzeghoud, M., Buforn, E., Pro, C., and Fitas, A.: The 1980, 1997 and 1998 Azores earthquakes and some seismo-tectonic implications. Tectonophysics, 435(1-4), 37-54, https://doi.org/10.1016/j.tecto.2007.01.008, 2007.

Braunmiller, J., Kradolfer U., Baer M. and Giardini D. Regional Moment- Tensor inversion in the European-Mediterranean area. Tectonophysics, 356, 5-22. [Dataset] https://doi.org/10.1016/S0040-1951(02)00374-8, 2002.

Briais, A., Armijo, R., Winter, T., Tapponnier, P. and Herbecq, A.: Morphological evidence for Quaternary normal faulting and seismic hazard in the Eastern Pyrenees. Annales Tectonicae 4(1), 19-42, 1990.

Buforn, E., Bezzeghoud, M., Udías, A., and Pro, C.: Seismic sources on the Iberia-African plate boundary and their tectonic implications. Pure and Applied Geophysics, 161, 623-646, https://doi.org/10.1007/s00024-003-2466-1, 2004.

Busetti, S., Jiao, W. and Reches, Z. Geomechanics of hydraulic fracturing microseismicity: Part 1. Shear, hybrid and tensile events. AAPG Bulletin, v. 98, no. 11, pp. 2439-2457, 2014.Cabral, J.: An example of intraplate neotectonic activity, Vilarica Basin, northeast Portugal. Tectonics, 8, 285–303. https://doi.org/10.1029/TC008i002p00285, 1989.

Cabral, J.: Neotectonics of mainland Portugal: state of the art and future perspectives. Journal of Iberian Geology 38 (1), 71-84 http://dx.doi.org/10.5209/rev_JIGE.2012.v38.n1.39206, 2012.

Cabral, J., Mendesa, V.B., Figueiredo, P., da Silveira, A.B., Pagarete, J., Ribeiro, A., Dias, R. and Ressurreição, R.: Active tectonics in Southern Portugal (SW Iberia) inferred from GPS data. Implications on the regional geodynamics. J. Geodyn., 112, 1-11. http://dx.doi.org/10.1016/j.jog.2017.10.002, 2017.

Cabral, J., Dias, R., Cunha, P.P. and Cabral, M.C.: Quaternary tectonic activity of the São Marcos–Quarteira fault (Algarve, southern Portugal): a case study for the characterization of the active geodynamic setting of SW Iberia. J. Iber. Geol. https://doi.org/10.1007/s41513-019-00102-2, 2019.

Cabrera, L., Roca, E. and Santanach, P.: Basin formation at the end of a strike-slip fault: the Cerdanya Basin (eastern Pyrenees). Jour. Geol. Soc. London 145, 261-268. doi:10.1144/gsjgs.145.2.0261, 1988.

Cannavò, F. and Palano, M.: Defining geodetic reference frame using Matlab®: PlatEMotion 2.0. Pure and Applied Geophysics, 173(3), 937–944. https://doi.org/10.1007/s00024-015-1112-z, 2016.

Carreño, E., Benito, B., Martínez Solares, J.M., Cabañas, L., Giner, J., Murphy, P., López, C.,Del Fresno, C., Alcalde, J.M., Gaspar-Escribano, J.M., Antón, R., Martínez-Díaz, J., Cesca, S., Izquierdo, A., Sánchez Caballero, J.G., and Expósito, P.: The 7 June mbLg 4.2 Escopete Earthquake: An Event with Significant Ground Motion in a Stable Zone (Central Iberian Peninsula). Seismol. Res. Lett., Volume 79, number 6. 820-829. [Dataset] doi: 10.1785/gssrl.79.6.820, 2008.

Casas-Sainz, A.M. and de Vicente, G.: On the tectonic origin of the iberian topography. Tectonophysics, 465. 31 pp. https://doi.org/10.1016/j.tecto.2009.01.030, 2009.

Capote, R., de Vicente, G. and González-Casado, J.M.: An application of the slip model of brittle deformation to focal mechanism analysis in three different plate tectonics situations, Tectonophysics, 191, 399 – 409, https://doi.org/10.1016/0040-1951(91)90070-9, 1991.

Cebriá, J.M., López-Ruiz, J., Doblas, M., Martins, L.T. and Munha. J.: Geochemistry of the Early Jurassic Messejana-Plasencia dyke (Portugal-Spain); Implications on the origin of the Central Atlantic Magmatic Province. J. Petrol., 44 (3), 547-568, 2003.

Cesca, S., Stich, D., Grigoli, F., Vuan, A., López-Comino, J.A., Niemz, P., Blanch, E., Dahm, T. and Ellsworth, W.: Seismicity at the Castor gas reservoir driven by pore pressure diffusion and asperities loading. Nature communications, 12:4783, [Dataset] https://doi.org/10.1038/s41467-021-24949-1, 2021.

Chevrot, S., Sylvander, M. and Delouis, B.: A preliminary catalog of moment tensor for the Pyrenees. Tectonophysics, 510, 239-251. [Dataset] doi:10.1016/j.tecto.2011.07.011, 2011.

Cloetingh, S., Burov, E., Beekman, F., Andeweg, B., Andriessen, P.A.M, García- Castellanos, D., de Vicente, G. and Vegas, R.: Lithospheric folding in Iberia. Tectonics, 2002, 21,5,1041. 26 pp. doi:10.1029/2001TC901031,2002

Comas, M. C., Platt, J. P., Soto, J. I., and Watts, A. B.: The origin and tectonic history of the Alboran Basin: insights from Leg 161 results. In Proceedings of the ocean drilling program scientific results (Vol. 161, pp. 555-580), 1999.

Custodio, S., Lima, V., Vales, D., Cesca, S. and Carrilho, F.: Imaging active faulting in a region of distributed deformation from the joint clustering of focal mechanisms and hypocentres: Application to the Azores–western Mediterranean region. Tectonophysics, 676, 70-89. [Dataset].https://doi.org/10.1016/j.tecto.2016.03.013. 2016.

d'Acremont, E., Gutscher, M.A., Rabaute, A., Mercier de Lépinay, B., Lafosse, M., Poort, J., Ammar, A., Tahayt, A., Le Royc, P., Smit, J., Do Couto, D., Cancouët, R., Prunier, C., Ercilla, G. and Gorini, C.: High-resolution imagery of active faulting offshore Al Hoceima, Northern Morocco. Tectonophysics 632, 160-166, http://dx.doi.org/10.1016/j.tecto.2014.06.008, 2014.

de Vicente, G. (1988), Análisis poblacional de fallas. El sector de enlace Sistema Central- Cordillera Ibérica, Ph.D. thesis, 317 pp., Univ. Complutense de Madrid, Madrid.

de Vicente, G., Cloetingh, S., Muñoz-Martín, A., Olaiz, A., Stich, D., Vegas, R., Galindo-Zaldívar, J. & Fernández-Lozano, J.: Inversion of moment tensor focal mechanisms for active stresses around the microcontinent Iberia: Tectonic implications, Tectonics, 27(TC1009), doi:10.1029/2006TC002093, 2008.

de Vicente, G., and Vegas, R.: Large-scale distributed deformation-controlled topography along the western Africa–Eurasia limit: Tectonic constraints. Tectonophysics, 474(1–2), 124–143. https://doi.org/10.1016/j.tecto.2008.11.026, 2009.

de Vicente, G., Cloetingh, S., J. Van Wees, J.D. and Cunha, P.P.: Tectonic classification of Cenozoic Iberian foreland basins. Tectonophysics, 502 (1-2), 38-61. doi:10.1016/j.tecto.2011.02.007, 2011.

de Vicente, G., Cunha, P. P., Muñoz-Martín, A., Cloetingh, S., Olaiz, A., and Vegas, R.: The Spanish-Portuguese Central System: An example of intense intraplate deformation and strain partitioning. Tectonics, 37. https://doi.org/10.1029/2018TC005204, 2018.

de Vicente, G., Olaiz, A., Muñoz-Martín, A. and Cunha, P.P.: Longest and still longer: The Messejana-Plasencia dyke and its links with later Alpine deformation belt in Iberia. Tectonophysics, Volume 815, 2021, 229009, ISSN 0040-1951, https://doi.org/10.1016/j.tecto.2021.229009, 2021.

de Vicente, G., Díez Fernández, R., Cunha, P.P. and Olaiz, A.: Active tectonics (Plio-Quaternary) in the western sector of the Madrid Cenozoic Basin. Iberfault 2022, ISBN:978-84-18321-58-0, 2022.

de Vicente, G., Terrinha, P., Carbonell, R., Muñoz-Martín, A. and Olaiz, A.: The Trans-Iberia Central Orogen and aborted subduction. X Simposio sobre el margen Ibérico Atlántico. Bilbao. Abstracts volume 14-16, 2022.

De Ruig, M.J.: Extensional diapirism in the Eastern Prebetic Foldbelt, Southeastern Spain. In: Jackson, M.P.A., Roberts, D.G., Snelson, S. (Eds.), Salt tectonics: a global perspective. AAPG Memoir 65, 353-367, https://doi.org/10.1306/M65604C17, 1995.

Del Pie Perales, L.: Inversión del momento sísmico para terremotos de la región cantábrica: implicaciones geodinámicas. Master thesis. University of Oviedo. 77 pp [Dataset].https://digibuo.uniovi.es/dspace/bitstream/10651/39062/6/TFM_%20Laura%20Pie%20Perales.pdf, 2016

Delvaux, D., Moeys, R., Stapel, G., Petit, C., Levi, K., Miroshnichenko, A., Ruzhich, V. and San´kov, V.: Paleostress reconstructions and geodynamics of the Baikal region, Central Asia, Part 2. Cenozoic rifting. Tectonophysics 282, 1-38. https://doi.org/10.1016/S0040-1951(97)00210-2, 1997.

Diaz, J., Gallar, J. and Carbonell, R.: Moho topography beneath the Iberian-Western Mediterranean region mapped from controlled-source and natural seismicity surveys. Tectonophysics 692A, 74-85. doi: 10.1016/j.tecto.2016.08.023, 2016.

Domingues, A., Custódio, S. and Cesca, S.: Waveform inversion of small-to-moderate earthquakes offshore southwest Iberia. Geophys. J. Int, Vol 192, Issue 1, January, 2013, Pages 248–259, https://doi.org/10.1093/gji/ggs010, 2013.

Dziewonski, A.M., Chou, T.A. and Woodhouse, J.H.: Determination of earthquake source parameters from waveform data for studies of global and regional seismicity, J. Geophys. Res., 86, 2825-2852. [Dataset]. doi:10.1029/JB086iB04p02825, 1981.

Ercilla, G., Galindo-Zaldívar, J., Estrada, F., Valencia, J., Juan, C., Casas, D., Alonso, B., Mª. Comas, M.C., Tendero-Salmerón, V., Casalbore, D., Azpiroz-Zabala, M., Bárcenas, P., Ceramicola, S., Chiocci, F.L., Idárraga-García, J., López-González, N., Mata, P., Palomino, D., Rodríguez-García, J.A., Teixeira, M., Nespereira, J., Vázquez, J.T. and Yenes, M. Understanding the complex geomorphology of a deep sea area affected by continental tectonic indentation: The case of the Gulf of Vera (Western Mediterranean). Geomorphology 402 108126 https://doi.org/10.1016/j.geomorph.2022.108126, 2022.

Etheve, N., Mohn, G., Frizon de Lamotte, D., Roca, E., Tugend, J. and Gómez-Romeu, J.: Extreme Mesozoic crustal thinning in the eastern Iberia margin: The example of the Columbrets Basin (Valencia Trough). Tectonics, 37. https://doi.org/10.1002/2017TC004613, 2018.

Etchecopar, A., Vasseur, G., and Daignieres, M.: An inverse problem in microtectonics for the determination of stress tensors from fault striation analysis. J. Struct. Geol., vol.3, no 1, pp 51-65. https://doi.org/10.1016/0191-8141(81)90056-0, 1981.

Ekström, G., Nettles, M. and Dziewonski, A.M.: The global CMT project 2004-2010: Centroid-moment tensors for 13,017 earthquakes, Phys. Earth Planet. Inter., 200-201, 1-9. [Dataset]. doi:10.1016/j.pepi.2012.04.002, 2012.

ETH- Swiss Seismological Service [Dataset] https://geophysics.ethz.ch/research/groups/sed.html

Faccenna, C., Piromallo, C., Crespo-Blanc, A., Jolivet, L. and Rossetti, F.: Lateral slab deformation and the origin of the western Mediterranean arcs. Tectonics, 23, TC1012, doi:10.1029/2002TC001488, 2004.

Fernández-Viejo, G., Álvarez Pulgar, J., Gallastegui, J and Quintana, L. The fossil accretionary wedge of the Bay of Biscay: Critical wedge analysis on depth-migrated seismic sections and geodynamical implications. Journal of Geology, vol. 120, n.º 3, pp. 315-31, https://doi.org/10.1086/664789., 2012

Ferranti, L., Passaro, S. and de Alteriis, G.: Morphotectonics of the Gorringe Bank summit, eastern Atlantic Ocean, based on high-resolution multibeam bathymetry. Quat. Int., 9-114. https://doi.org/10.1016/j.quaint.2013.11.011, 2014.

Flinn, D.: On tests of significance of preferred orientation in three-dimensional fabric diagrams. The Journal of Geology, 66(5): 526-539. https://doi.org/10.1086/626533, 1958.

Fonseca, J.F.B.D. and Vilanova, S.P.: The 23 April 23 1909 Benavente (Portugal) M 6.3 Earthquake. Seismol. Res. Lett., 81, 3. doi: 10.1785/gssrl.81.3.534, 2010.

Frohlich, C. and Apperson, K.D.: Earthquake focal mechanisms, moment tensors, and the consistency of seismic activity near plate boundaries, Tectonics, 11, 279–296, https://doi.org/10.1029/91TC02888, 1992.

Galindo-Zaldivar, J., Jabaloy, J., Serrano, I., Morales, J., González-Lodeiro, F. and Torcal, F.: Recent and present-day stresses in the Granada Basin (Betic Cordilleras): Example of a late Miocene-present-day extensional basin in a convergent plateboundary.Tectonics,18,(4),686-702, doi: 10.1029/1999tc900016, 1999.

Galindo-Zaldivar, J., Gil, A.J., Tendero-Salmerón, V., Borque, M.J., Ercilla, G., González-Castillo, L., Sánchez-Alzola, A., Lacy, M.C., Estrada, F., Avilés, M., Alfaro, P., Madarieta-Txurruka, A. and Chacón, F.: The Campo de Dalias GNSS Network Unveils the Interaction between Roll-Back and Indentation Tectonics in the Gibraltar Arc. Sensors, 22, 2128. https://doi.org/10.3390/s22062128, 2022.

Gallastegui, J. and Pulgar, J.A.: Initiation of an active margin at the North Iberian continent-ocean transition. Tectonics 21 (4). https://doi.org/10.1029/ 2001TC901046, 2002.

Gamboa, D., Omira, R., Piedade, A., Terrinha, P., Roque, C. and Zitellini, N.: Destructive episodes and morphological rejuvenation during the lifecycles of tectonically active seamounts: Insights from the Gorringe Bank in the NE Atlantic. Earth Planet Sci Lett, 116772. https://doi.org/10.1016/j.epsl.2021.116772. 2021.

García-Navarro, E., Fernández, C. and Camacho, M.A.: Mesozoic tectonic evolution of the southwest continental Iberian Margin. Geodinamica Acta 18/2, 131–144, 2005.

Gea P.J., Negredo, A.M. and Mancilla, F. dL.: The Gibraltar slab dynamics and its influence on past and present-day Alboran domain deformation: Insights from thermo-mechanical numerical modelling. Front. Earth Sci. 11:995041. doi: 10.3389/feart.2023.995041, 2023.

Gephart, J.W. and Forsyth, D.W.: An improved method for determining the regional stress tensor using earthqueakes focal mechanism data: application to the San Fernando earthquake sequence. J. Geophys. Res., vol. 89, no B11, pages 9305-9320. https://doi.org/10.1029/JB089iB11p09305, 1984.

GFZ-Postdam [Dataset] https://geofon.gfz-potsdam.de/old/eqinfo/list.php?mode=mt

Giner-Robles, J. L., Gumiel, P., Pérez-López, R., Rodríguez-Pascua, M. A. García-Mayordomo, J., Paredes, C. and González-Casado, J. M.: Importancia en la elección de la orientación del plano de falla en el análisis de mecanismos focales de terremotos. 5th Asamblea Hispano Portuguesa de Geodesia y Geofísica, Com. Española de Geod. Y Geofís., Sevilla, Spain. 2006.

Global Centroid Moment Tensor (former Harvard Centroid Moment Tensor) [Dataset] https://www.globalcmt.org/

Gómez de la Peña, L.: The origin and tectono-sidimentary structure of the Alboran Basin. PhD. Thesis. Universidad de Barcelona. 319 pp, 2017.

Gómez-Novell, O., Ortuño, M., García-Mayordomo, J., Insua-Arévalo, J. M., Rockwell, T. K., Baize, S., Martínez-Díaz, J.J., Pallàs, R. and Massana, E.: Improved geological slip rate estimations in the complex Alhama de Murcia Fault zone (SE Iberia) and its implications for fault behaviour. Tectonics, 41, e2022TC007465. https://doi.org/10.1029/2022TC007465, 2022.

Goula, X., Olivera, C., Fleta, J., Grellet, B., Lindo, R., Rivera, L., Cisternas, A. and Carbon, D.: Present and recent stress regime in the eastern part of the Pyrenees. Tectonophysics 308, 487-502. doi:10.1016/S0040-1951(99)00120-1, 1999.

Grácia, E., Pallàs, R., Soto, J.I., Comas, M., Moreno, X., Masana, E., Santanach, P., Diez, S., García, M. and Dañobeitia, J.: Active faulting offshore SE Spain (Alboran Sea): Implications for earthquake hazard assessment in the Southern Iberian Margin. Earth Planet. Sci. Lett. 241 (2006) 734–749. doi:10.1016/j.epsl.2005.11.009, 2006.

Gràcia, E., Grevemeyer, I., Bartolomé, R., Perea, H., Martínez-Loriente, S., Gómez de la Peña, L., Villaseñor, A., Klinger, Y., Lo Iacono, C., Diez, S., Calahorrano, A., Camafort, M., Costa, S., d'Acremont, E., Rabaute, A. and Ranero, C.R.: Earthquake crisis unveils the growth of an incipient continental fault system. Nature Communications, 10:3482. https://doi.org/10.1038/s41467-019-11064-5, 2019.

Granja Bruña, J.L., Vegas, R., Sentre, M.A., Muñoz-Martín, A. and Sainz-Maza, S.: Gravity modeling of the lithosphere in the Calatrava Volcanic Province (Spain): geodynamic implications. J. Iber. Geol. 41 (2) 2015: 233-252 http://dx.doi.org/10.5209/rev_JIGE.2015.v41.n2.47617, 2015.

Grevemeyer, I., Lange, D., Villinger, H., Custódio, S. and Matias, L.: Seismotectonics of the HorseshoeAbyssal Plain and Gorringe Bank,eastern Atlantic Ocean: Constraintsfrom ocean bottom seismometer data,J. Geophys. Res. Solid Earth,122,63–78, doi:10.1002/2016JB013586, 2017.

Gutiérrez, F., Sevil, J., Silva, P.G., Roca, E. and Escosa, F.: Geomorphic and stratigraphic evidence of Quaternary diapiric activity enhanced by fluvial incision. Navarrés salt wall and graben system, SE Spain. Geomorphology, 342, 1, 176-195. https://doi.org/10.1016/j.geomorph.2019.06.002, 2019.

Gutscher, M.A., Dominguez, S., Westbrook, G.K., Le Roy, P., Rosas, F., Duarte, J.C., Terrinha, P., Miranda, J.M., Graindorge, D., Gailler, A., Sallares, V. and Bartolome, R.: The Gibraltar subduction: A decade of new geophysical data. Tectonophysics 574-575, 72-91. http://dx.doi.org/10.1016/j.tecto.2012.08.038, 2012.

Heidbach, O., Barth, A., Müller, B., Reinecker, J., Stephansson, O., Tingay, M. and Zang, A.: WSM quality ranking scheme, database description and analysis guidelines for stress indicator. World Stress Map Technical Report 16-01, GFZ German Research Centre for Geosciences. DOI: http://doi.org/10.2312/wsm.2016.001 , 2016.

Heidbach, O., Barth, A., Connolly, P., Fuchs, F., Müller, B., Reinecker, J., Sperner, B., Tingay, M. and Wenzel, F.: Stress Maps in a Minute: The 2004 World Stress Map Release, EOS Trans., 85(49), 521-529, https://doi.org/10.1029/2004EO490001, 2004.

Heidbach, O., and Höhne, J.: CASMI - a tool for the visualization of the World Stress Map data base, Comp. & Geosciences, 34(7), 783-791, doi:10.1016/j.cageo.2007.06.004, 2008.

Heidbach, O., Rajabi, M., Cui, X., Fuchs, K., Müller, B., Reinecker, J., Reiter, K., Tingay, M., Wenzel, F.,, Xie, F., Ziegler, M.O., Zoback., M.L. and Zoback, M. .: The World Stress Map database release 2016: Crustal stress pattern across scales, Tectonophys., 744, 484-498, doi:10.1016/j.tecto.2018.07.007, 2018.

Heidbach, O., Rajabi, M., Reiter, K., Ziegler, M. O. and WSM Team: World Stress Map Database Release 2016, edited by G. D. Services, GFZ German Research Centre for Geosciences, doi:10.5880/WSM.2016.001, 2016.

Heidbach, O., Reinecker, J., Tingay, M., Müller, B., Sperner, B., Fuchs, K. and Wenzel, F.: Plate boundary forces are not enough: Second- and third-order stress patterns highlighted in the World Stress Map database, Tectonics, 26, TC6014, doi:10.1029/2007TC002133, 2007.

Heidbach, O., Tingay, M., Barth, A., Reinecker, J., Kurfeß, D. and Müller, B.: Global crustal stress pattern based on the World Stress Map database release 2008, Tectonophys., 482, 3-15, doi:10.1016/j.tecto.2009.07.023, 2010.

Instituto Andaluz de Geofísica [Dataset] https://iagpds.ugr.es/investigacion/informacion-general

Instituto Geográfico Nacional de España [Dataset]https://www.ign.es/web/ign/portal/tensor-momento-sismico/-/tensor-momento-sismico/getExplotacion

IPMA Portuguese Institute for Sea and Atmosphere [Dataset] https://www.ipma.pt/en/geofisica/tensor

Istituto Nazionale di Geofisica e Vulcanologia [Dataset] http://terremoti.ingv.it/en/tdmt

Jackson, M.P.A. and Hudec, M.R.: Salt tectonics, Principles and Practice. Part III - Salt-Tectonic Systems. Chapter 12 - Strike-Slip Salt-Tectonic Systems. Cambridge University Press. https://doi.org/10.1017/9781139003988.016, 2017.

Jost, M. L., Büßelberg, T., Jost, Ö., and Harjes, H. P.: Source parameters of injection-induced microearthquakes at 9 km depth at the KTB deep drilling site, Germany. Bull. Seismol. Soc. Am., 88(3), 815-832, 1998.

Kagan, Y.Y.: 3-D rotation of double-couple earthquake sources, Geophys. J. Int., 106, 709–716, https://doi.org/10.1111/j.1365-246X.1991.tb06343.x ,1991.

Khazaradze, G., Pena-Castellnou, S., Santamaría-Gómez, A., and Vernant, P.: 3D GPS velocity field of the Iberian Peninsula. Geophysical Research Abstracts, 21, EGU2019-9710, 2019.

Kiratzi, A. and Papazachos, C.: Active crustal deformation from the Azores triple junction to Middle East, Tectonophysics 243, 1-24, https://doi.org/10.1016/0040-1951(94)00188-F ,1995.

Lacan, P. and Ortuño, M.: Active Tectonics of the Pyrenees: A review. J. Iber. Geol. 38 (1) 2012: 9-30. http://dx.doi.org/10.5209/rev_JIGE.2012.v38.n1.39203, 2012.

Lacan, P.: Activité Sismotectonique Plio-Quaternaire del'Ouest des Pyrénées. PhD. Thesis. Université de Pau et des Pays de l'Adour: 284 pp., 2008.

Ljunggren, C., Chang, Y., Janson, T. and Christiansson, R.: An overview of rock stress measurement methods, International Journal of Rock Mechanics and Mining Sciences, 40(7-8), 975-989, doi:10.1016/j.ijrmms.2003.07.003. 2003.

López-Fernández, C., Fernández-Viejo, G., Olona, J. and Llana-Fúnez, S.: Intraplate Seismicity in Northwest Iberia along the Trace of the Ventaniella Fault: A Case for Fault Intersection at Depth. Bull. Seismol. Soc. Am., Vol. 108, No. 2, pp. 604–618, April 2018, doi: 10.1785/0120170215. 2018.

Lundstern, J-E. and Zoback, M.D.: Multiscale variations of the crustal stress field throughout North America. Nature Communications, 11:1951, https://doi.org/10.1038/s41467-020-15841-5, 2020.

Madarieta-Txurruka, A., González-Castillo, L., Peláez, J. A., Catalán, M., Henares, J., Gil, A. J., Lamas-Fernández, F. and Galindo-Zaldivar, J.: The role of faults as barriers in confined seismic sequences: 2021 seismicity in the Granada Basin (Betic Cordillera). Tectonics, 41, e2022TC007481. https://doi.org/10.1029/2022TC007481, 2022.

Maillard, A. and Mauffret, A.: Crustal structure and riftogenesis of the Valencia Trough (north-western Mediterranean Sea). Basin Research, 11, 357–379, 1999.

Maouche, S., Bouhadad, Y., Harbi, A., Rouchiche, Y., Ousadou, F. and Ayadi, A.: Active Tectonics and Seismic Hazard in the Tell Atlas (Northern Algeria): A Review. In: Bendaoud, A., Hamimi, Z., Hamoudi, M., Djemai, S., Zoheir, B. (eds) The Geology of the Arab World---An Overview. Springer Geology. Springer, Cham. https://doi.org/10.1007/978-3-319-96794-3_10, 2019.

Maouche, S., Meghraoui, M., Morhange, C., Belabbes, S., Bouhadad, Y. and Haddoum, H.: Active coastal thrusting and folding, and uplift rate of the Sahel Anticline and Zemmouri earthquake area (Tell Atlas, Algeria). Tectonophysics 509, 69–80. doi:10.1016/j.tecto.2011.06.003, 2011.

Martin-Gonzalez, F. and Heredia, N.: Geometry, structures and evolution of the western termination of the Alpine-Pyrenean Orogen reliefs (NW Iberian Peninsula). J. Iber. Geol., 37, DOI: 10.5209/rev_JIGE.2011.v37.n2.1103, 2011.

Martín, R., Stich, D., Morales, J and Mancilla F.: Moment tensor solutions for the Iberain-Maghreb region during the IberArray deployment (2009-2013). Tectonophysics, 663, 261-274, [Dataset] https://doi.org/10.1016/j.tecto.2015.08.012, 2015.

Martínez-Díaz, J. J.: Neotectonica y Tectonica Activa del Oeste de Murcia y sur de Almeria (Cordillera Betica). PhD Thesis, Universidad Complutense Madrid: 470 p, 1998.

Martínez-Díaz, J.J., Masana, E, and Ortuño, M.: Active tectonics of the Alhama de Murcia fault, Betic Cordillera, Spain. J. Iber. Geol. 38 (1), 253-270. http://dx.doi.org/10.5209/rev_JIGE.2012.v38.n1.39218, 2012.

Martínez-García, P.: Recent tectonic evolution of the Alboran Ridge and Yusuf regions. PhD. Thesis. Instituto andaluz de Ciencias de la Tierra (CSIC-UGR). 276 pp, 2012.

Martínez-Loriente, S., Gracia, E., Bartolome, R., Sallarès, V., Connors, C., Perea, H., Lo Iacono, C., Klaeschen, D., Terrinha, P., Dañobeitia, J.J. and Zitellini, N.: Active deformation in old oceanic lithosphere and significance for earthquake hazard: Seismic imaging of the Coral Patch Ridge area and neighboring abyssal plains (SW Iberian Margin). Geochem., Geophys., Geosyst., 14, 00. doi: 10.1002/ggge.20173, 2013.

Masana, E., Neotectonic features of the Catalan Coastal Ranges, Northeastern Spain. Acta Geológica Hispánica, 29, 2-4, 107-121, 1996.

Masana, E., Martínez-Díaz, J.J. Hernández-Enrile, J.L. and Santanach, P., The Alhama de Murcia fault (SE Spain), a seismogenic fault in a diffuse plate boundary: Seismotectonic implications for the Ibero-Magrebian region. J. Geophys. Res., Vol. 109, B01301, doi:10.1029/2002JB002359, 2004.

Masana, E., Moreno, X., Gràcia, E., Pallàs, R., Ortuño, M., López, R., Gómez-Novell, O., Ruano, P., Perea, H., Stepancikova, P. and Khazaradze, G.: First evidence of paleoearthquakes along the Carboneras Fault Zone (SE Iberian Peninsula): Los Trances site. Geologica Acta, 16, 4, 461-476 DOI: 10.1344/GeologicaActa2018.16.4.8, 2018.

Matias, H., Kress, P., Terrinha, P., Mohriak, W., Paulo, T., Menezes, L., Matias, L., Santos, F. and Sandnes, F.: Salt tectonics in the western Gulf of Cádiz, southwest Iberia. American Association of Petroleum Geologist Bulletin, 95(10), 1667-1698, 2011.

Matos, C., Custódio, S., Batlló, J., Zahradník, J., Arroucau, P., Silveira, G., and Heimann, S.: An active seismic zone in intraplate west Iberia inferred from high-resolution geophysical data. J. Geophy. Res: Solid Earth, 123, 2885–2907. [Dataset] https://doi.org/10.1002/2017JB015114, 2018.

McKenize, D.P.: The relation between fault plane solutions for earthquakes and the direction of the principal stresses. Bull. Seismol. Soc. Am. 59 (2): 591–601. https://doi.org/10.1785/BSSA0590020591, 1969.

Meghraoui, M., Cisternas, A. and Philip, H.: Seismotectonics of the Lower Cheliff Basin: Structural background of the El Asnam (Algeria) earthquake. Tectonics, 5, 6, 809-836, https://doi.org/10.1029/TC005i006p00809, 1986.

Meghraoui, M., and Pondrelli, S.:Active faulting and transpression tectonics along the plate boundary in North Africa, Ann. Geophys. 55, no. 5, doi: 10.4401/ag-4970, 2012.

Michael, A.: Use of Focal Mechanisms to Determine Stress: A Control Study. Journal of Geophysical Research: Solid Earth 92, no. B1: 357–68. https://doi.org/10.1029/JB092iB01p00357, 1987.

Montadert, L., B. Damotte, J. P. Fail, J. R. Delteil, and P. Valéry, Structure géologique de la plaine abyssale du Golfe de Gascogne, in Histoire Structurale du Golfe de Gascogne, edited by J. Debysier, X. Le Pichon, and M. Montadert, VI.14.1-VI.14.42, Technip, París, 1971.

Montenat, C. and d'Estevou, P. O.: The diversity of late Neogene sedimentary basins generated by wrench faulting in the Eastern Betic Cordillera, SE Spain. J. Pet. Geol., 22(1), 61-80, https://doi.org/10.1111/j.1747-5457.1999.tb00459.x, 1999.

Morales, J., Azañón, J.M., Stich, D., Roldán, F.J., Pérez-Peña, J.V., Martín, R., Cantavella, J.V., Martín, J.B., Mancilla, F. and González.Ramón, A.: The 2012-2013 earthquake swarm in the eastern Gualdalquivir Basin (South Spain): A case of heterogenous faulting due to oroclinal bending. Gondwana Research, Volume 28, Issue 4, Pages 1566-1578, https://doi.org/10.1016/j.gr.2014.10.017, 2015.

Morawietz, S., Heidbach, O., Reiter, K., Ziegler, M. O., Rajabi, M., Zimmerman, G., Müller, B. and Tingay, M.: An open access stress magnitude database for Germany and adjacent regions, Geothermal Energy, doi:10.1186/s40517 020 00178-5, 2020.

Neres, M., Carafa, M. M. C., Fernandes, R.M.S., Matias. L., Duarte, J.C., Barba, S. and Terrinha, P. Lithospheric deformation in the Africa-Iberia plate boundary: Improved neotectonic modeling testing a basal-driven Alboran plate. JGR Solid Earth, https://doi.org/10.1002/2016JB013012, 2019.

Neres, M., Neves, M. C., Custódio, S., Palano, M., Fernandes, R. and Matias, L.: Gravitational potential energy in Iberia: A driver of active deformation in high-topography regions. J. Geophys. Res.: Solid Earth, 123. https://doi.org/10.1029/2017JB015002, 2018a.

Neres, M., Terrinha, P., Custodio, S.M., Silva, J., and Miranda, J.M. Geophysical evidence for a magmatic intrusion in the ocean-continent transition of the SW Iberia margin. Tectonophysics, 744:118–133, Oct 2018, https://doi.org/10.1016/j.tecto.2018.06.014. 2018b

Neves, M.C., Terrinha, P., Afilhado, A., Moulin, M., Matias, L. and Rosas, F.: Response of a multi-domain continental margin to compression: Study from seismic reflection–refraction and numerical modelling in the Tagus Abyssal Plain. Tectonophysics 468, 113–130. http://dx.doi.org/10.1016/j.tecto.2008.05.008. 2009.

Nirrengarten, M., Manatschal, G., Tugend, J., Kusznir, N. and Sauter, D. Kinematic Evolution of the Southern North Atlantic: Implications for the Formation of Hyperextended Rift Systems. Tectonics, https://doi.org/10.1002/2017TC004495., 2018

Olaiz, A.J., Álvarez Gómez, J., A, de Vicente, G., Muñoz-Martín, A., Cantavella, J.V., Custódio, S., Vales, D. and Heidbach, O.: Seismo-tectonics of Greater Iberia: An updated review, Zenodo repository, doi:10.5281/zenodo.14326528

Olaiz, A.J., Muñoz-Martín, A., de Vicente, G., Vegas, R. and Cloetingh, S.: European continuous active tectonic strain–stress map. Tectonophysics, 474, 33–40, https://doi.org/10.1016/j.tecto.2008.06.023, 2009.

Olivera, C., Redondo, E., Lambert, J., Riera Melis, A. and Roca, A.: Els terratrèmols dels segles XIV i XV a Catalunya. Institut Cartogràfic de Catalunya, Monografies 30, 407pp, ISBN: 84-393-6961-1, 2006.

Pedrera, A., Ruiz-Constán, A., Marín-Lechado, C., Galindo-Zaldivar, J., González, A. and Peláez, J. A.: Seismic transpressive basement faults and monocline development in a foreland basin (eastern Guadalquivir, SE Spain). Tectonics, 32, 1571–1586. https://doi.org/ 10.1002/2013TC003397, 2013.

Perea, H., Masana, E. and Santanach, P.: An active zone characterized by slow normal faults, the northwestern margin of the València trough (NE Iberia): a review. J. Iber. Geol. 38(1):31–52, https://doi.org/10.5209/rev_jige.2012.v38.n1.39204, 2012.

Perea, H., Masana, E. and Simón, J.L.: Slow active faults along the extensional northeastern margin of the Iberian Peninsula. In The Geology of Iberia: A Geodynamic Approach Volume 5: Active Processes: Seismicity, Active Faulting and Relief, 10.1007/978-3-030-10931-8_4, 2020.

Pereira, R., Rosas, F., Mata, J., Represas, P., Escada, C. and Silva, B.: Interplay of tectonics and magmatism during post-rift inversion on the central West Iberian Margin (Estremadura Spur). Basin Research, 33:1497–1519. DOI: 10.1111/bre.12524, 2021.

Pierdominici, S., and Heidbach, O.: Stress field of Italy – Mean stress orientation at different depths and wave-length of the stress pattern, Tectonophys., 532-535, 301-311, doi:10.1016/j.tecto.2012.02.018, 2012.

Pla-Pueyo, S., Gierlowski-Kordesch, E.H., Viseras, C. and Soria, J.M.: Major controls on sedimentation during the evolution of a continental basin: Pliocene–Pleistocene of the Guadix Basin (Betic Cordillera, southern Spain). Sediment. Geol. 219 (2009) 97–114. http://dx.doi.org/10.1016/j.sedgeo.2009.05.001, 2009.

Pondrelli S., Morelli, A. and Ekström, G.: European-Mediterranean Regional Centroid MomentTensor catalog: solutions for years 2001 and 2002, Phys. Earth Planet. Int., 145, 127-147. [Dataset] https://doi.org/10.1016/j.pepi.2004.03.008, 2004.

Pondrelli, S., Morelli, A., Ekström, G. Mazza, S., Boschi, E. and Dziewonski, M.: European- Mediterranean regional centroid-moment tensors: 1997-2000, Phys. Earth Planet. Int., 130, 71-101. [Dataset] https://doi.org/10.1016/S0031-9201(01)00312-0, 2002.

Posadas, A.M., Vidal, F., De Miguel, F., Alguacil, G., Peña, J., Ibañez, J.M. and Morales, J.: Spatial-Temporal Analysis of a Seismic Series Using the Principal Components Method: The Antequera Series, Spain, 1989. J. Geophys. Res., 98, B2, 1923-1932., 1993.

Rajabi, M., Tingay, M., Heidbach, O., Hillis, R. and Reynolds, S.: The present-day stress field of Australia, Earth Sci. Rev., 168, 165-189, doi:10.1016/j.earscirev.2017.04.003. 2017a

Rajabi, M., Tingay, M., King, R. and Heidbach, O.: Present-day stress orientation in the Clarence-Moreton Basin of New South Wales, Australia: A new high density dataset reveals local stress rotations, Basin Res., 29(S1), 622-640, doi:10.1111/bre.12175, 2017b.

Rajabi, M., Ziegler, M. O., Heidbach, O., Mukherjee, S. and Esterle, J.: Contribution of mine borehole data toward high-resolution stress mapping: An example from northern Bowen Basin, Australia, Int. J. Rock Mech. Min. Sci., 173, doi:10.1016/j.ijrmms.2023.105630, 2024.

Ramos, A., Fernández, O., Terrinha, P. and Muñoz, J.A.: Extension and inversion structures in the Tethys?Atlantic linkage zone, Algarve Basin, Portugal. Int. J. Earth Sci. (Geol Rundsch) 1–17. http://dx.doi.org/10.1007/s00531-015-1280-1., 2015.

Ramsay, J.G.: Folding and fracturing rocks. McGraw-Hill, New York, N.Y. 560 pp., ISBN 978-0070511705, 1967.

Reches, Z.: Faulting of rocks in three-dimensional strain fields. II. Theoretical analysis, Tectonophysics, 47, 109 – 129. https://doi.org/10.1016/0040-1951(83)90264-0, 1983.

Reches, Z.: Determination of the tectonic stress tensor from slip along faults that obey the Coulomb yield condition. Tectonics, vol. 6, no. 6, 849-861 https://doi.org/10.1029/TC006i006p00849, 1987.

Reches, Z., Baer, G. and Hatzor, Y.: Constraints on the strength of the Upper Crust from stress inversion of fault slip data, J. Geophys, Res, 97, 12,481 – 12,493. https://doi.org/10.1029/90JB02258, 1992.

Reicherter, K.R. and Peters, G. Neotectonic evolution of the Central Betic Cordilleras (Southern Spain). Tectonophysics 405,191-212. https://doi.org/10.1016/j.tecto.2005.05.022, 2005.

Reicherter, K.R. and Pletsch, T.K. Evidence for a synchronous Circum-Iberian subsidence event and its relation to the African-Iberian plate convergence in the Late Cretaceous. Terra Nova 12, 141-147, https://doi.org/10.1046/j.1365-3121.2000.123276.x 2002.

Reinecker, J., Tingay, M., Muller, B. and Heidbach, O.: Present-day stress orientation in the Molasse Basin, Tectonophysics, 482(1-4), 129-138, doi:10.1016/j.tecto.2009.07.021, 2010.

Reiter, K., Heidbach, O., Schmitt, D. R., Moeck, I., Ziegler, M. O. and Hauck, C.: Crustal stress field pattern of Canada, Tectonophys., 636, 111-124, doi:10.1016/j.tecto.2014.08.006, 2014.

Roca, E. and Guimerà, J.: The Neogene structure of the eastern Iberian margin: Structural constraints on the crustal evolution of the Valencia trough (western Mediterranean). Tectonophysics 203(1–4):203–218. https://doi.org/10.1016/0040-1951(92)90224-t, 1992.

Rueda, J. and Mezcua, J.: Near-real-time seismic moment-tensor determination in Spain. Seismol. Res. Lett. 76, 455-465. [Dataset] https://doi.org/10.1785/gssrl.76.4.455, 2005.

Ruiz, M., Diaz, J., Canari, A., Ortuño, M. and Vergés, J.: Seismic Activity at the Eastern Pyrenean Termination. Available at SSRN: https://ssrn.com/abstract=4341777 or http://dx.doi.org/10.2139/ssrn.4341777, 2023.

Ruiz, M., Gallart, J., Díaz, J., Olivera, C., Pedreira, D., López, C., González-Cortina, J.M. and Pulgar, J.A.: Seismic activity at the western Pyrenean Edge. Tectonophysics 412, 217–235, https://doi.org/10.1016/j.tecto.2005.10.034, 2006.

Ruiz Constán, A.: Lithospheric structure of the western Betic Cordillera and its foreland implications in the recent tectonic evolution. PhD Thesis. Universidad de Granada, 162 pp., 2009.

Ruiz-Constán, A., Galindo-Zaldívar, J., Pedrera, A., Célérier, B. and Marín-Lechado, C.: Stress distribution at the transition from subduction to continental collision (northwestern and central Betic Cordillera), Geochem. Geophys. Geosyst., 12, Q12002, doi:10.1029/2011GC003824, 2011.

Rutter, E.H., Faulkner, D.R. and Burgess, R.: Structure and geological history of the Carboneras Fault Zone, SE Spain: Part of a stretching transform fault system. Journal of Structural Geology, 45, 68-86. http://dx.doi.org/10.1016/j.jsg.2012.08.009, 2012.

Sanz de Galdeano, C.: Geologic evolution of the Betic Cordilleras in the Western Mediterranean, Miocene to the present. Tectonophysics, 172 (1-2), 107-119, https://doi.org/10.1016/0040-1951(90)90062-D, 1990.

Sanz de Galdeano, C., García-Tortosa, F.J., Peláez, J.A., Alfaro, P., Azañón, J.M., Galindo- Zaldívar, J., López Casado, C., López Garrido, A.C., Rodríguez-Fernández, J. and Ruano, P.: Main active faults in the Granada and Guadix-Baza Basins (Betic Cordillera). J. Iber. Geol. 38 (1) 2012: 209-223. http://dx.doi.org/10.5209/rev_JIGE.2012.v38.n1.39215 , 2012.

Scognamiglio, L., Tinti, E. and Quintiliani, M.: Time Domain Moment Tensor (TDMT) (Data set). Istituto Nazionale di Geofisica e Vulcanologia (INGV). [Dataset] https://doi.org/10.13127/TDMT, 2006.

SGC, 1985–1997. Butlletí Sismològic. Generalitat de Catalunya. Servei Geològic de Catalunya.

Sibuet, J. C., Srivastava, S. P. and Spakman, W. Pyrenean orogeny and plate kinematics. J. Geophys. Res. 109:B08104, doi:10.1029/2003JV002514., 2004

Simón J.L.: Late Cenozoic stress field and fracturing in the Iberian Chain and Ebro Basin (Spain). J. Struct. Geol. 11:285–294, https://doi.org/10.1016/0191-8141(89)90068-0, 1989.

Simón, J.L.: Active faults in the Iberian Chain. In The Geology of Iberia: A Geodynamic Approach Volume 5: Active Processes: Seismicity, Active Faulting and Relief, 10.1007/978-3-030-10931-8_4, 2020.

Soumaya, A., Ben Ayed, N., Rajabi, M., Meghraoui, M., Delvaux, D., Kadri, A., et al.: Active faulting geometry and stress pattern near complex strike-slip systems along the Maghreb region: Constraints on active convergence in the western Mediterranean. Tectonics, 37, 3148–3173. https://doi.org/10.1029/ 2018TC004983, 2018.

Souriau, A. and Pauchet, H.: A new synthesis of Pyrenean seismicity and its tectonic implications. Tectonophysics 290, 221-244. doi: 10.1016/S0040-1951(98)00017-1, 1998.

Sperner, B., Müller, B., Heidbach, O., Delvaux, D., Reinecker, J. and Fuchs, K.: Tectonic stress in the Earth's crust: advances in the World Stress Map project, in New insights in structural interpretation and modelling, edited by D. A. Nieuwland, pp. 101-116, Geological Society, London, doi:10.1144/gsl.sp.2003.212.01.07, 2003.

Srivastava, S. P., Roest, W. R., Kovacs, L. C., Oakey, G., Levesque, S., Verhoef, J. and Macnab, R. Motion of Iberia since the Late Jurassic: Results from detailed aeromagnetic measurements in the Newfoundland Basin, Tectonophysics, 184, 229 – 260, https://doi.org/10.1016/0040-1951(90)90442-B 1990

Stich, D., Serpelloni, E., Mancilla, F.L. and Morales, J.: Kinematics of the Iberia– Maghreb plate contact from seismic moment tensors and GPS observations, Tectonophysics, 426, 3-4, 295-317 [Dataset] doi:10.1016/j.tecto.2006.08.004, 2006.

Stich, D., Martín, R., and Morales, J.: Moment tensor inversion for Iberia-Maghreb earthquakes 2005-2008. Tecthonophysics, 483, 390-398. [Dataset] https://doi.org/10.1016/j.tecto.2009.11.006, 2010.

Stich, D., Ammon, C.J. and Morales, J.: Moment tensor solutions for small and moderate earthquakes in the Ibero-Maghreb region, J. Geophys. Res. 108, 02JB002057. [Dataset] https://doi.org/10.1029/2002JB002057, 2003.

Stich, D., Batlló, J., Maciá, R., Teves-Costa, P and Morales, J.: Moment tensor inversion with single-component historical seimograms: The 1909 Benavente (Portugal) and Lambesc (France) earthquakes. Geophys. J. Int. 162, 850–858, [Dataset]doi: 10.1111/j.1365-246X.2005.02680.x, 2005.

Stich, D., Martín, R., Morales, J., López-Comino, J.A. and Mancilla, FdL.: Slip partitioning in the 2016 Alboran Sea Earthquake Sequence (Western Mediterranean). Front, Earth Sci. 8:587356. [Dataset]. https://doi.org/10.3389/feart.2020.587356, 2020.

Tendero-Salmerón, V.: Recent and active deformation structures in the centra-eastern sector of the Betic Cordillera and the Alboran Sea: indentation processes and roll-back. Ph.D. Thesis. Universidad de Granada, 238 pp, 2022.

Tendero-Salmerón, V., Galindo-Zaldivar, J., Peláez, J. A.,Martínez-Martos, M., Henares, J. and Marín-Lechado, C.: Seismicity in strike-slip foreland faults (central Betic cordillera front): Evidence of indentation tectonics. Tectonics, 39, e2020TC006143. https:// doi.org/10.1029/2020TC006143, 2020.

Tendero-Salmerón V, Lafosse M, d'Acremont E, Rabaute A, Azzouz O, Ercilla G, Makkaoui M and Galindo-Zaldivar J.: Application of Automated Throw Backstripping Method to Characterize Recent Faulting Activity Migration in the Al Hoceima Bay (Northeast Morocco): Geodynamic Implications. Front. Earth Sci. 9:645942. doi: 10.3389/feart.2021.645942, 2021.

Tendero-Salmerón, V., Galindo-Zaldivar, J., d'Acremont, E., Catalán, M., Martos, Y.M., Ammar, A. and Ercilla, G.: New insights on the Alboran Sea basin extension and continental collision from magnetic anomalies related to magmatism (western Mediterranean). Marine Geology, 443, 106696. https://doi.org/10.1016/j.margeo.2021.106696, 2022.

Terrinha, P.: Structural Geology and Tectonic Evolution of the Algarve Basin, South Portugal. PhD Thesis. Imperial College, London, pp. 430, 1998.

Terrinha, P., Matias, L., Vicente, J., Duarte, J., Pinheiro, J.L., Lourenço, N., Diez, S., Rosas, F., Magalhães, V., Valadares, V., Zitellini, N., Roque, C., Mendes Víctor, L. and MATESPRO Team: Morphotectonics and strain partitioning at the Iberia–Africa plate boundary from multibeam and seismic reflection data. Marine Geology, 267, 156–174. http://dx.doi.org/10.1016/j.margeo.2009.09.012, 2009.

Tingay, M., Müller, B., Reinecker, J. and Heidbach, O.: State and Origin of the Present-day Stress Field in Sedimentary Basins: New Results from the World Stress Map Project, paper presented at 41st U.S. Symposium on Rock Mechanics (USRMS): 50 years of Rock Mechanics - Landmarks and Future Challenges, Golden, Colorado, June, 17-21, 2006.

Tingay, M., Müller, B., Reinecker, J., Heidbach, O., Wenzel, F. and Fleckenstein, P.: Understanding tectonic stress in the oil patch: The World Stress Map Project, The Leading Edge, 24, 1276-1282, doi:10.1190/1.2149653, 2005.

Tozer, B., Sandwell, D. T., Smith, W. H. F., Olson, C., Beale, J. R. and Wessel, P.: Global Bathymetry and Topography at 15 Arc Sec: SRTM15+, Earth and Space Science, 6(10), 1847-1864, doi:10.1029/2019ea000658, 2019.

Vadillo Muñoz, O.: Análisis de la serie sísmica de Palenciana (Córdoba), Junio de 1989 y sus implicaciones sismotectónicas. PhD Thesis. Universidad Complutense de Madrid. 364 pp, 1999.

Van der Woerd, J., Dorbath, C., Ousadou, F., Dorbath, L., Delouis, B., Jacques, E., Tapponnier, P., Hahou, Y., Menzhi, M., Frogneux, M. and Haessler, H.: The Al Hoceima Mw 6.4 earthquake of 24 February 2004 and its aftershocks sequence. J. Geodyn., 77, 89–109. http://dx.doi.org/10.1016/j.jog.2013.12.004, 2014.

Van Hinsbergen, D., Vissers, J.J., Reinoud, L.M. and Spakman, W.: Origin and consequences of western Mediterranean subduction, rollback, and slab segmentation. Tectonics 33 (4), 393-419, https://doi.org/10.1002/2013TC003349, 2014.

Vázquez, J.T., Alonso, B., Fernández-Puga, M.C., Gómez-Ballesteros, M., Iglesias, J., Palomino, D., Roque, C., Ercilla, G. and Díaz-del-Río, V.: Seamounts along the Iberian Continental Margins. Boletín Geológico y Minero, 126 (2-3): 483-514 ISSN: 0366-0176, 2015.

Vergés, J.: Evolución de los sistemas de rampas oblicuas de los Pirineos meridionales: fallas del Segre y Pamplona. Boletín Geológico y Minero, 114 (1): 87-101 ISSN: 0366-0176, 2003.

Villamor, M. P.: Cinemática terciaria y cuaternaria de la falla de Alentejo-Plasencia y su influencia en la peligrosidad sísmica del interior de la península ibérica. PhD Thesis. Universidad Complutense de Madrid, 343 pp.. 2002.

Villaseñor, A., Herrmann, R.B., Gaite, B. and Ugalde, A.: Fault reactivation by gas injection at an undergroung gas storage off the east coast of Spain. Solid Earth, 11, 63-74. [Dataset].https://doi.org/10.5194/se-11-63-2020, 2020.

Wessel, P. and Smith, W. H. F.: New version of the Generic Mapping Tools released. Eos, Transactions American Geophysical Union, 76(33), 329. https://doi.org/10.1029/95EO00198, 1995.

Wessel, P., Smith, W.H.F., Scharroo, R., Luis, J. and Wobbe, F.: Generic Mapping Tools: Improved Version Released. Eos, 94, 45, 5. 409–420, 2013.

Wetzler, N., Sagy, A., Marco, S. and Reches, Z. Asymmetry of faults and stress patterns within the Dead Sea basin as displayed by seismological analysis. Tectonophysics 819, 229069, https://doi.org/10.1016/j.tecto.2021.229069, 2021.

Ziegler, M. O. and Heidbach O.: Manual of the Matlab script Stress2Grid v1.1Rep., 33 pp, GFZ German Research Centre for Geosciences, Potsdam, 2019, https://doi.org/10.5880/wsm.2019.002

Zitellini, N., Gràcia, E., Matias, L., Terrinha, P., Abreu, M.A., DeAlteriis, G., Henriet, J.P. Dañobeitia, J.J., Masson, D.G. Mulder, T., Ramella, R., Somoza, L. and Diez, S.: The quest for the Africa–Eurasia plate boundary west of the Strait of Gibraltar. Earth and Planetary Science Letters 280, 13–50 https://doi.org/10.1016/j.epsl.2008.12.005, 2009.

Zoback, M.-L.: First- and Second- Order Patterns of Stress in the Lithosphere: The World Stress Map Project, J. Geophys. Res., 97., https://doi.org/10.1029/92JB00132, 1992.